Metal Oxides as Electrocatalysts at Oxygen Electrodes in Electrochemical Systems

Shuai Zhao, Ph.D.

University of Connecticut, 2016

Fuel cells, one of the most widely studied electrochemical energy conversion devices, together with electrolyzers, a promising energy storage system for natural renewable energy and source of purified hydrogen, have attracted significant research attention in recent years as the demand for energy continues to increase with no end to this energy expansion in sight. However, electrochemical reactions occurring at oxygen electrodes such as the oxygen reduction reaction (ORR) and oxygen evolution reaction (OER) have very slow kinetics, which has limited the industrialization of both fuel cells and electrolyzers because slow kinetics leads directly high reaction overpotentials. Metal oxides have been widely adopted in terms of electrocatalysts for these oxygen reactions, either as as a support to enhance the stability or activity of platinum, or as the direct catalysts for ORR and OER in alkaline media. However, what is not known is how and why metal oxides as support materials can influence the performance of precious metals through their interactions, what the active sites are for different electrochemical reactions and how to control the desired phases by manipulating the synthesis conditions. This study will probe these very important questions.

Chapter 1 of this work provides a background into the ORR/OER mechanism, active sites, and catalyst candidates in electrochemical devices. **Chapter 2** presents experimental approaches including material synthesis, and both physical and

electrochemical characterization. **Chapters 3 and 4** of this study investigate doped metal carbides and metal oxides as support materials for platinum and iridium catalysts for the ORR and OER, respectively, in acidic electrolytes. The **Chapter 3** is an investigation of tungsten carbide modified with titanium as a potential non-carbon support for platinum during the ORR in acid media. **Chapter 4** discusses the relationship between the synthesis parameters of iridium/iridium oxide supported on titanium-doped tungsten oxide and its durability both ex-situ in a three-electrode cell on a rotating disk electrode (RDE) and in-situ in an operating electrolyzer. **Chapter 5** discusses a new method to determine the electrochemically active area of iridium oxide, one of the most common anode catalysts in commercial PEM electrolyzers, in-situ through its electrochemical psuedocapacitance. **Chapter 6** probes the performance and function of tin-doped indium oxides (ITO) as a support for platinum ORR catalyst in alkaline media. Metal-support interactions were studied mainly through X-ray photoelectron spectroscopy and electrochemical measurements. **Chapter 7** focuses on the electrocatalysis of carbon nanotube (CNT)-supported cobalt oxide for both oxygen reduction and evolution reactions in alkaline media. An optimized procedure to produce a highly stable and active bifunctional ORR/OER hybrid catalyst was developed along with an understanding of the impact of metal oxide anchoring sites and synthesis parameters on catalyst durability. This part of the study provides novel perspectives for the design of carbon-based, hybrid materials and insight into the synthesis-property relationships for these and future electrocatalysts.

In summary, this work has studied metal oxides as catalysts and support materials for precious metals during aqueous oxygen reactions. Wherever possible, the

fundamental cause for their behavior, including enhanced electrocatalytic activity and durability, was probed thoroughly through physical and electrochemical characterization.

Metal Oxides as Electrocatalysts at Oxygen Electrodes in Electrochemical Systems

Shuai Zhao,

B.S. Chemical Engineering, Dalian University of Technology, 2012

A Dissertation

Submitted in Partial Fulfillment of the

Requirements for the Degree of

Doctor of Philosophy

at the

University of Connecticut

2016

APPROVAL PAGE

Doctor of Philosophy Dissertation
Metal Oxides as Electrocatalysts at Oxygen Electrodes in Electrochemical Systems

Presented by
Shuai Zhao, B.S.

Major Advisor_____
William E. Mustain

Associate Advisor_____
Brian G. Willis

Associate Advisor_____
Hui Xu

Associate Advisor_____
Radenka Maric

Associate Advisor_____
Steven Suib

Associate Advisor_____
Yu Lei

University of Connecticut

2016

ACKNOWLEDGMENTS

The past four years has been one of the most important periods in my life, during which I tried my best to absorb the positive influences from all the amazing and important people around me, and I saw the incredible growth of myself from an immature college graduate to an independent researcher, with the help and support from all these individuals. Most gratefully, I would express my sincere thanks to my supervisor Dr. William Mustain, an energetic academic professional with great achievement at such a young age, who is always my research motive and live model, from the time I became your student till today. You gave me all the professional guidance for research, writing and publication, and also career path, as well as the right attitude to be a Ph.D. candidate, especially enormous encouragement and proper strictness during my depressed period, which suited me well and got me out of a bad time immediately. Your life philosophy and family value also influenced me a lot. It is true that what you can learn and what your life is during pursuit of your Ph.D. degree really depend on your advisor, especially as an international student. That I can be a much better me today is all because of you. I always feel so lucky to have you as a mentor at the beginning of my career life and you help define where I can go further. Thank you very much, Dr. Mustain, to have such a huge positive influence on me in my life.

I would also like to thank all my associate advisors on my thesis committee: Dr. Brian Willis, Dr. Hui Xu, Dr. Radenka Maric, and Dr. Steven Suib, and Dr. Yu Lei for their professional academic advises, support and encouragement. Special thanks goes to Dr. Hui Xu, who provided me a special opportunity to work in industry as an intern for

LIST OF FIGURES

LIST OF ABBREVIATIONS AND SYMBOLS

ε - Relative Dielectric Donstant

ε_0 - Permittivity of Free Space

v - Kinematic Viscosity

η - Overpotential

A - Electrode Surface Area

AEMEC - Anion Exchange Membrane Electrolysis Cell

AEMFC - Anion Exchange Membrane Fuel Cell

AFC - Alkaline Fuel Cells

BET - Brunauer-Emmet-Teller

BJH - Barret, Joyner and Halenda

CNT - Carbon Nanotube

CV - Cyclic Voltammetry

D - Diffusion Coefficient

DFT - Density Functional Theory

e - Charge of An Electron

E_{fb} - Flatband Potential

ECSA – Electrochemically Active Surface Area

EDS - Energy Dispersive X-ray Spectroscopy

F - Faraday's Constant

FEFI - Ferrocyanide/Ferricyanide

FE-SEM - Field Emission Scanning Electron Microscope

FIB - Focused Ion Beam

G – Free Energy

GCE - Glassy Carbon Electrode

GDL – Gas Diffusion Layer

GO – Graphene Oxide

H_{upd} - Hydrogen Underpotential Deposition

HER - Hydrogen Evolution Reaction

HOR - Hydrogen Evolution Reaction

HRTEM - High Resolution Transmission Electron Microscopy

i – Current

ITO - Tin-doped Indium Oxides

k - Boltzmann Constant

M - Molar Concentration

MOR – Methanol Oxidation Reaction

n - Number of Electrons

N_D - doping density

NHE - Normal Hydrogen Electrode

NPs - Nanoparticles

OER - Oxygen Evolution Reaction

ORR - Oxygen Reduction Reaction

P – Pressure

PEMEC - Proton Exchange Membrane Electrolysis Cell

PEMFC - Proton Exchange Membrane Fuel Cell

Q - Charge

RDE - Rotating Disk Electrode

RDS - Rate Determining Step

RHE - Reversible Hydrogen Electrode

RPM - Revolutions per Minute

SEM - Scanning Electron Microscopy

T - Temperature

TEM - Transmission Electron Microscopy

U - Potential

V - Volts

URFC - Unitized Regenerative Fuel Cell

XPS - X-Ray Photoelectron Spectroscopy

XRD - X-Ray Diffraction

TABLE OF CONTENTS

CHAPTER 1 - INTRODUCTION

Fuel cells and electrolyzers have been attracting significant interest for energy applications for the past several decades as energy conversion and storage devices, respectively. The combination of both, known as a reversible or unitized regenerative fuel cell (URFC), had the highest energy density among all aircraft energy storage devices back in the 1990s (including supercapacitors, various chemical batteries, etc.) of about 450 watt-hours per kilogram. Recent advances have increased this number to 800 watt-hours per kilogram [1,2], and URFCs remain one of the highest energy density storage devices in aircraft today. In all of the above systems, the oxygen electrode limits the device performance. The oxygen reduction reaction (ORR) occurring at the proton exchange membrane fuel cell (PEMFC) and anion exchange membrane fuel cell (AEMFC) cathode and combination of ORR and the oxygen evolution reaction (OER) at the electrodes of URFCs are all sluggish compared to their hydrogen electrode counterparts from both a kinetic and mass transport perspective. The poor oxygen kinetics demand the development of electrocatalysts that enable the ORR/OER to happen at potentials close to their thermodynamic limit; this remains the major bottleneck for applicable devices [3].

1.1 Mechanism of Oxygen Reduction and Evolution Reactions in Acidic Electrolyte

1.1.1 Mechanism of Oxygen Reduction Reaction in Acidic Electrolyte

PEMFCs are the most widely applied and industrially mature fuel cells for mobile applications. A simplified schematic of a common PEMFC is shown in **Fig. 1.1** and the cell reactions are given as **Equations 1.1-1.3**. At the anode, hydrogen is electrochemically oxidized producing protons and electrons. The protons transfer through a proton-conducting polymer electrolyte (most commonly Dupont's Nafion®) and meet with the protons and electrons, and oxygen, at the cathode side to produce water.

Anode: $H_2 \rightarrow 2H^+ + 2e^-$, $E° = 0.0$ V (1.1)

Cathode: $O_2 + 4H^+ + 4e^- \rightarrow 2H_2O$, $E° = 1.23$ V (1.2)

Overall: $2H_2 + O_2 \rightarrow 2H_2O$ (1.3)
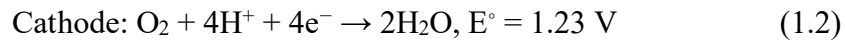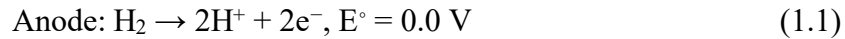
The electrochemical efficiency of a fuel cell can be calculated as a simple ratio of the cell operating voltage, E_{cell} in **Equation 1.4**, and the thermodynamic voltage, E_{rev} [4].

$$E_{cell} = E_{rev\,(P_{H_2}, P_{O_2}, T)} - \Delta E_{ohmic} - \eta_{ORR} - \eta_{tX}$$ (1.4)

The thermodynamic cell voltage, which depends on the partial pressures of the reactants and the cell temperature, is approximately 1.23 V under standard conditions (25°C, 1atm), according to **Eq. 1.1** and **1.2**. The second term on the right side of **Equation 1.4** is the voltage loss in the cell due to ohmic resistance, including both the electronic contact resistance between fuel cell components and proton conduction resistance in the membrane [5]. The third term is the potential difference between the thermodynamic oxygen reduction reaction (ORR) potential and the experimentally observed potential, the so-called overpotential, which is due to the sluggish ORR kinetics. Note that the hydrogen oxidation reaction (HOR) kinetics at the anode is so rapid, that the HOR overpotenial is not typically considered at all. The fourth term is the mass transfer

loss, incurred by the poor oxygen-transport through the diffusion medium and the catalyst layer. Therefore, the ORR occurring at the cathode is the most challenging technical issue and most intensively investigated due to the sluggish kinetics and mass transport issue compared with the anode hydrogen oxidation reaction.

There are two possible pathways for the ORR: a partial two-electron reduction to hydrogen peroxide (H_2O_2) or a full four-electron reduction to water. **(Fig. 1.2)** In an operating PEMFC, the former is unwanted because not only does it clearly decrease the energy conversion efficiency, peroxides produce radicals that can attack and destroy the polymer electrolyte.

Despite decades of development, state-of-the-art ORR catalysts are still platinum nanoparticles supported on carbon black (Pt/C). Density functional theory (DFT) calculations have shown that Pt (111) facets (and facets of Pt alloys) provide the ideal oxygen adsorption energy, a key descriptor for ORR activity. Oxygen adsorption is followed by either O_2* dissociating into 2O* to react with hydrogen forming water (four-electron route) or directly reacting with hydrogen producing water with (two-electron route) or without (four-electron route) forming intermediate of H_2O_2* [6]. The binding energy (associated with the d-band center) between oxygen atoms and the Pt catalyst surface not only help to enhance the electron transfer rate but also to facilitate breaking of the O=O bond [7–10], which allows an overwhelming amount of the reaction to occur through the preferred four-electron pathway.
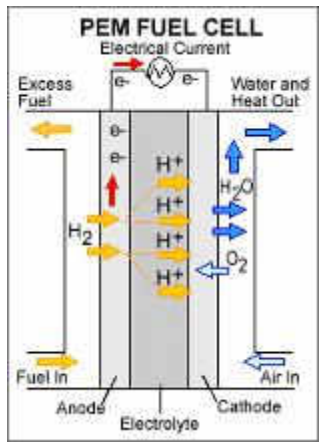
Figure 1.1 Schematic of a common proton exchange membrane fuel cell (PEMFC) [11].

$$O_2 \xrightarrow{\text{diff}} O_{2(ads)} \underset{k_{-2}(-2e^-)}{\overset{k_2(+2e^-)}{\rightleftharpoons}} H_2O_{2(ads)} \xrightarrow{k_3(+2e^-)} H_2O$$

$k_1(+4e^-)$

k_4

$k_6 \quad k_5$

H_2O_2
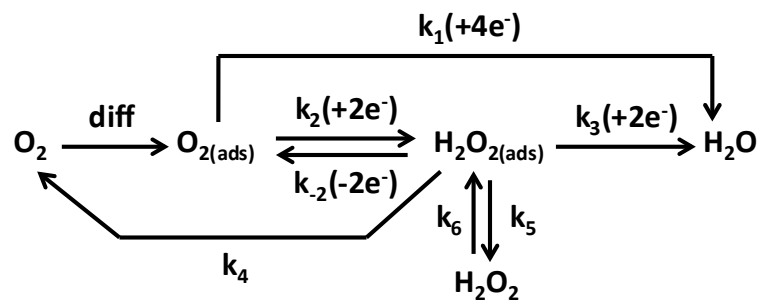
Figure 1.2 Different ORR pathways in acid solution.

1.1.2 Mechanism of Oxygen Evolution Reaction in Acidic Electrolyte

A schematic of the proton exchange membrane electrolysis cell (PEMEC) is shown in **Fig. 1.3** and cell reactions are given as **Equations 1.5-1.7**.

$$\text{Anode: } 2H_2O \rightarrow O_2 + 4H^+ + 4e^-, E° = 1.23 \text{ V} \qquad (1.5)$$

$$\text{Cathode: } 2H^+ + 2e^- \rightarrow H_2, E° = 0.0 \text{ V} \qquad (1.6)$$

$$\text{Overall: } 2H_2O \rightarrow 2H_2 + O_2 \qquad (1.7)$$
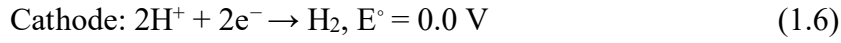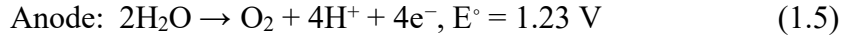
As an energy storage system, a PEMEC electrochemically oxidizes deionized water pumped into the anode of the electrolyzer, producing O_2 as well as protons and electrons. Similar to the PEMFC, the protons transfer through the polymer membrane; however in the PEMEC, they combine directly with the electrons from the external circuit to produce pure hydrogen, which is basically a reverse mode of a fuel cell. When combined with renewable and intermittent energy like solar and wind, PEMECs can play an essential role by producing hydrogen with relatively high efficiency, and unlike steam reforming systems PEMECs also quickly cycle up and down, and deliver hydrogen with high and differential pressure (self-compression). However, there are several challenges that have to be solved in this process, with the most pressing being to reduce the OER overpotential, and hence energy losses, at the PEMEC anode [12]. Improving the anode catalyst will thus improve the efficiency of the electrolyzer and reducing the cost of the catalyst is also commercially desirable. Therefore, many studies focus on understanding the fundamental mechanism of the oxygen evolution reaction (OER).
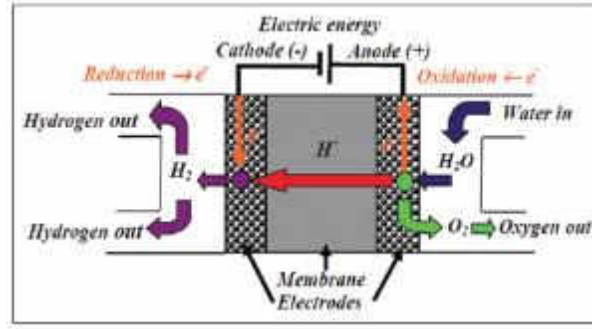
Figure 1.3 Schematic of a proton exchange membrane electrolysis cell (PEMEC) [13].

Some computational work has been done on several classes of materials including metals [14] and rutile oxides [15,16]. In these studies, researchers proposed that the OER mechanism consists of four consecutive proton and electron transfer steps, with the intermediates being HO*, O*, and HOO*. They predicted the OER activity with estimated O* binding energies as a descriptor, which mirrors work on ORR catalyst in fuel cells. Later, the Rossmeisl group introduced a new, universal descriptor for the OER – a scaling relationship between the binding energy of HOO* and HO*, which was derived from first principles periodic DFT calculations [17]. The proposed free energy diagram for the four electron reaction pathway for an ideal catalyst is shown in **Fig. 1.4**. They claimed that the free energy difference between the adsorbed oxy and hydroxyl anions ($\Delta G_{O*} - \Delta G_{HO*}$) was the origin of the overpotential for oxygen evolution catalysis, which agreed well with experimental results in literature. Their studied oxides included rutile, perovskite, spinel, rock salt, and bixbyite oxides. The most commonly used and industrially mature electrocatalysts in PEM electrolyzers are noble metal oxides with a rutile crystal structure, ruthenium and iridium oxide. However, since dominant cost of an electrolyzer is electricity, about 70 % of the total [18], increasing the efficiency is of a higher importance than decreasing catalyst cost. Efforts for developing a high activity and efficiency OER catalyst in acid have lasted for decades. **Chapter 4** will investigate the relationship between the OER catalyst synthesis parameters and the durability of the catalyst in PEM electrolyzer.
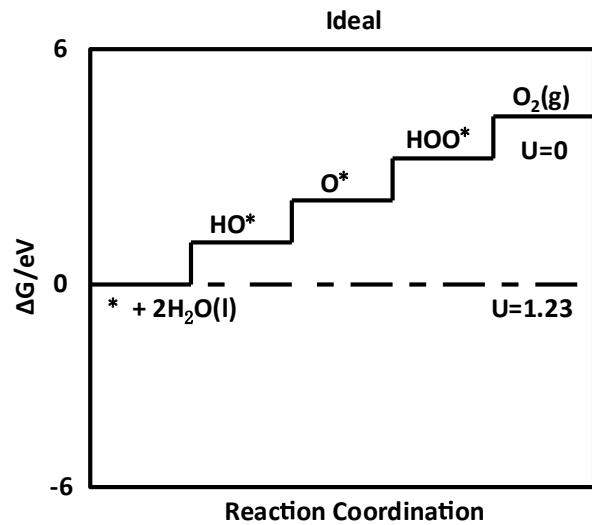
Figure 1.4 Standard free energy diagram for the OER at zero potential (U=0), equilibrium potential for oxygen evolution (U=1.23), and at the potential for which all steps become downwards at pH 0 and T=298 K over the ideal catalyst.

1.2 In-Situ Iridium Oxide Electrochemically Active Surface Area

Though according to the well accepted OER "volcano plot", it is known that the OER eletrocatalytic activity of RuO_2 and IrO_2 lie far ahead of other metal oxides [19] in terms of activity [20], benchmarking these catalysts in the same way that has been done for Pt PEMFC and AEMFC catalysts has proven very difficult since there does not exist a reliable method to determine their electrochemically active surface area (ECSA) in-situ. This means that the oxide specific activity and in-cell utilization remain a mystery today, which needs to be known in order to develop benchmarks and systematically discover new catalysts. Though the activity of RuO_2 is known to be higher than IrO_2, its dissolution under electrolyzer conditions mostly prevents its use in practical applications. Therefore, PEMECs with the IrO_2 anode that dominates the market will be solely studied and discussed in this work.

Traditionally, one of the most common methods to calculate the electrochemically active surface area (ECSA) of a catalyst is to collect a cyclic voltammogram (CV) in N_2-saturated electrolyte and measure the hydrogen adsorption charge (Q_r) during the negative-going scan after correction for double-layer charging [21]. This works for platinum because Pt has the ability to undergo hydrogen underpotential deposition (H_{upd}). The principle behind the H_{upd} method is that the charge under the voltammetric peaks for hydrogen adsorption is rooted in the attachment of one hydrogen atom on each metal atom on the surface. The equation for calculating the ECSA of Pt is shown in **Equation 1.8** [21]:

$$ECSA = \frac{Q_r}{m \times C} \tag{1.8}$$

where m is the Pt mass loading, and C is the charge of full monolayer coverage of H

atoms onto clean polycrystalline Pt (210 μC cm^{-2}). This method has been validated versus CO adsorption and Cu underpotential deposition methods for measuring the Pt ECSA [22] and has been extended to other metals including Rh, Ir and Ni.

However, iridium oxide does not have access to the same mechanism for underpotential deposition of H onto its surface, which makes it difficult to determine the ECSA. This has significant practical implications because iridium oxide is a very common anode catalyst material for the OER in the PEMEC. The inability to measure the ECSA makes it very difficult to benchmark in-situ anode catalyst performance including catalyst utilization and specific activity. **Chapter 5** in this study will present a new method to calculate the ECSA of IrO$_2$ in-situ for the application of PEM electrolyzers.

1.3 Possible Advantages of Alkaline Electrolyte Over Acidic Electrolyte

The study of electrocatalyst activity and stability in alkaline media was a popular research topic from the 1960s through the 1980s because of the development of alkaline fuel cells (AFCs) for space applications [23]. However, its terrestrial development was limited by problems with electrolyte carbonation and electrolyte leakage. Recent designs of AFCs such as laminar flow-based micro fuel cells, the boom of alkaline fuel cell companies such as AFC Energy and the breakthrough development of stable, high conductivity anion exchange membranes and ionomers have started to overcome the problems of conventional AFCs and revive researchers' interest in electrochemical reactions in alkaline media [24–26].

In alkaline media, the ORR is reasonably more favorable from a kinetic perspective than it is in acidic solution because the metal surface tends to have fewer

oxygenated adlayers, and the potential range of M–OH formation on platinum metals in alkaline solutions is considerably wider than in acidic solutions [27]. The electrode reactions in the anion exchange membrane fuel cell (AEMFC) are shown in **Equations 1.9-1.11**. The oxygen reduction reaction (ORR), which occurs at the AEMFC cathode, is one of the most widely studied reactions to date, similarly for the alkaline OER reaction (shown in **Equation 1.12**) at the anode of anion exchange membrane electrolyzer cell (AEMEC). Generally, researchers have proposed that the ORR in alkaline media proceeds through multistep reactions involving first the formation of an HO_2^- intermediate from adsorbed O_2 on the active sites of the catalyst surface, followed by its further reduction or decomposition to OH^- ions [28,29].
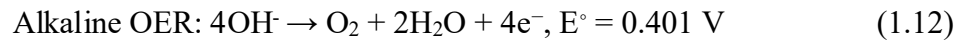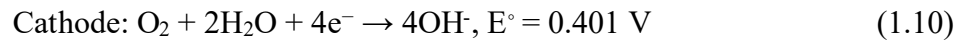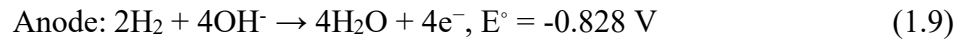
$$\text{Anode: } 2H_2 + 4OH^- \rightarrow 4H_2O + 4e^-, E° = -0.828 \text{ V} \qquad (1.9)$$

$$\text{Cathode: } O_2 + 2H_2O + 4e^- \rightarrow 4OH^-, E° = 0.401 \text{ V} \qquad (1.10)$$

$$\text{Overall: } 2H_2 + O_2 \rightarrow 2H_2O \qquad (1.11)$$

$$\text{Alkaline OER: } 4OH^- \rightarrow O_2 + 2H_2O + 4e^-, E° = 0.401 \text{ V} \qquad (1.12)$$

Though the shift in potential with pH is very well known (0.059V/pH) and often discussed, the differences in the interface and its role in the ORR mechanism are not as well known or as widely discussed. First, the lower potential required for the ORR in alkaline media changes the surface free energy, weakening the Pt-O bond energy compared to acid electrolyte [30]. This decreased bond energy, combined with the outer-sphere electron transfer mechanism [31,32] decreases the overpotential for the ORR in alkaline media relative to acidic media. Simply put, the ORR in alkaline media is more facile than it is in acid.

The lower energy requirement, combined with improved stability of transition metal systems in alkaline vs. acid media, suggest that the search for ORR/OER catalysts and support in alkaline media can expanded over much of the periodic table from noble metals to earth-abundant elements. The catalytic activity of the ORR electrocatalysis in alkaline media has been observed for elements over a significant portion of the periodic table from carbon compounds [33–35], to various transition metals [36–38], coinage metals [39–44], metal macrocycles including porphyrins [45–48], phthalocyanines [49–52] and metal oxides [53]. Although some high activity non-platinum group metal catalysts have been shown for the ORR in alkaline media [54,55], unfortunately, Pt-based catalysts still remain the most popular in the literature because of their proven combination of high stability and activity.

1.4 Impact of the Support on ORR Electrocatalysts

As mentioned above, regardless of the electrolyte, platinum group metals remain the most common oxygen electrocatalysts. One method to reducing the amount of Pt used at these electrodes, in order to reduce cost, is to increase dispersion through the use of a support. Carbon is the most common support for Pt in modern systems; however, the conventional Pt/C catalytic mass activity still requires a factor of >4 increase for the significant cost of large-scale applications [56]. Although the efforts of developing advanced carbon support materials to improve the stability and electrocatalytic activity of Pt clusters have improved device durability over time, the long-term instability of carbon materials still remains a major concern. The short catalyst life may be first caused by the

13

thermodynamic limitations of carbon support itself due to the oxidation/corrosion, as shown in the electrochemical reaction in **Equation 1.13** [57,58],

$$C + 2H_2O \rightarrow CO_2\,(g) + 4H^+ + 4e^-,\ E^\circ = 0.207\ V \qquad (1.13)$$
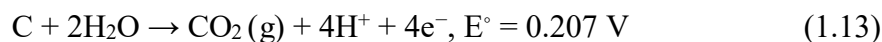
The surface carbon atoms can be activated electrochemically at any potential above 0.207 V vs. the normal hydrogen electrode (NHE). This means that carbon supports are intrinsically unstable under normal fuel cell operating conditions ($0.6 < E_{cathode}\ V < 0.8;\ 60 < T\ (^{\circ}C) < 90$). Then, the activated carbon species become the final product of CO_2 when reacting with neighboring water molecules, which then leads to mechanical failure and collapse of the catalyst layer pore structure. What's worse, the supported Pt may act as a catalyst for the carbon oxidation [59,60], which may localize the corrosion to areas in direct contact with Pt. This would further cause the poor dispersion or even the dissolution of Pt clusters on carbon. Other than the long-term stability issue of the catalyst itself, there would also be membrane degradation induced by the relatively high activity of carbon towards the two-electron reduction of oxygen to hydrogen peroxide [26][61]. Therefore, it is still a major challenge to design cheap and stable electrocatalysts for ORR in fuel cells.

A large number of alternative ceramic support materials have been introduced in the literature to manipulate the Pt dispersion, size, shape, etc. through electron transfer between the catalyst and support, and further improve corrosion resistance and reduce electrochemical surface area (ECSA) degradation rates [62–69]. Metal−support interactions can also improve the electrocatalytic activity of the supported Pt in several ways such as modification of the electronic states of Pt to increase the potential of the formation of Pt-OH groups [70] and reduction of the equilibrium OH adsorption by

lateral repulsion between Pt-OH and oxide surface [71–73]. Therefore, **Chapter 3** will try to present a theory to produce the potential modified ceramic support for platinum in acidic media, and in **Chapter 6** of this study, the application of tin-doped indium oxide (ITO) as an electrocatalyst support for Pt in alkaline media was explored. The ORR activity and stability of Pt/ITO are compared with a commercial Pt/Vulcan electrocatalyst. The differences of Pt/ITO catalyst in acidic and alkaline media, and the possible reasons for its high activity and stability are discussed.

1.5 ORR/OER Bifunctional Electrocatalysts for Alkaline Unitized Rversible Fuel Cells (URFCs)

Although for the past few decades precious metal catalysts have been extensively investigated for PEM and AEM electrocatalysts, they still have very high cost and poor reversibility for oxygen reactions. The last chapter, **Chapter 7** of this work will shed light upon the development of non-precious metal bifunctional ORR/OER electrocatalysts for reversible anion exchange membrane fuel cells or URFCs. Because this field is only emerging, it is necessary here to include a more in-depth discussion than the sections above where countless review articles have already been written about each topic.

It is always challenging to find stable and efficient bifunctional electrocatalysts, which drive both oxygen reduction and evolution reactions, because good catalysts for ORR mostly result in poor performance for OER and vice versa. Take the ORR and OER mechanisms on perovskite oxides as an example. Both reactions proceed via 4 electron transfer steps (indicated by the black numbers inside both reaction circles) as proposed by

Suntivich et al. in **Fig. 1.5** [74,75]. In the OER rate determining steps (RDS), a good OER catalyst tends to either lower the O-O bond formation energy (step 2 in the OER circle) or the proton extraction energy from the oxy-hydroxide group (step 3 in the OER circle). However, in the ORR case, the raised binding energy of O-O or the lowered binding energy of O-H would make the breakage of O-O and proton adsorption from water more difficult to occur in the reverse steps (steps 2 and 3 in the ORR circle). Similarly, what a good ORR catalyst may do in its RDS - either the surface hydroxide displacement (step 4 in the ORR circle) or the surface hydroxide regeneration (step 1 in the ORR circle) – would also result in the same situation to the reverse steps 4 and 1 in the OER circle. Therefore, it is always challenging to maintain a proper balance for reversible ORR/OER catalysis.

The most popular family of non-precious metal bifunctional OER/ORR electrocatalysts in alkaline media is transition metal oxides such as perovskite (i.e. $LaNiO_3$, $LaCoO_3$) and spinel-type transition metal oxides (e.g. Co_3O_4 and $NiCo_2O_4$). The spinel structure possesses a general formulation $A^{2+}B^{3+}_2O^{2-}_4$, with the oxide anions arranged in a cubic close-packed lattice and the cations A and B occupying some or all of the octahedral and tetrahedral interstitial sites in the lattice. A and B can be a single transition metal element with prototypical charges of +2 and +3, respectively, like aluminum, iron, cobalt, manganese, etc. A can also be a substitution, like copper, zinc, magnesium or nickel, of B. Spinel structures can be active for both ORR and OER reactions because they can provide donor-acceptor chemisorption sites for the reversible adsorption of oxygen because of the presence of mixed valences of the cations [76].
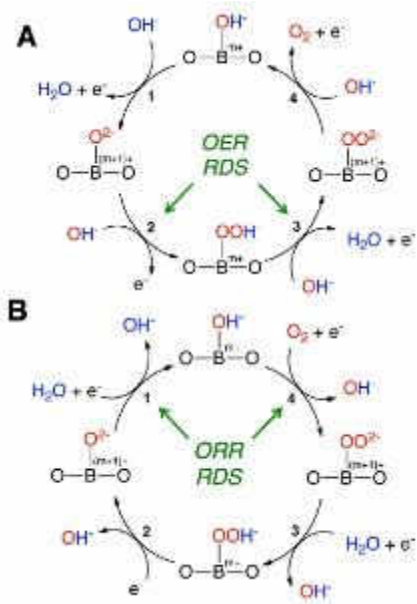
Figure 1.5 (a) Four-electron OER reaction mechanism on perovskite surface; (b) Four electron ORR mechanism for perovskite surface. Reprinted with permission from ref. [74,75] Copyright 2011 Science.

Though mixed valence oxides involving transition metals have been broadly considered as possible alternatives with ORR and OER catalytic activity in alkaline media, cobalt-based oxides (including their binary and ternary composites) in particular have shown generally high activity and relatively easy preparation, which has increased interest in these materials in recent years. Some recent studies have also shown promising activities using hybrid spinel-graphene materials, though the graphene-enhancement mechanism is still poorly understood [77,78]. These two categories will be further discussed in detail in the following two subsections.

1.5.1 Cobalt-based Spinel Oxide as Candidates of ORR/OER Reversible Electrocatalysts in Alkaline Electrolyte

a) Cobalt oxide (spinel cobaltite oxides)

Among the numerous low-cost non-precious metal oxides, cobalt oxides are promising for both ORR and OER in alkaline media [79–84]. Co_3O_4 has a normal spinel crystal structure ($A^{2+}B^{3+}_2O^{2-}_4$) based on a close-packed face centered cubic configuration of oxygen ions, as stated at the beginning of this section. Co^{2+} ions occupy one-eighth of the tetrahedral A sites while Co^{3+} ions occupy one half of the octahedral B sites [85].

In general, traditional theory states that the ORR is assumed to take place at active sites associated with the cations at the higher oxidation state [85]. During the ORR, the Co^{3+} ions would act as donor–acceptor reduction sites, due to the ability of Co_3O_4 to capture electrons and to provide electrons to O_2 in solution [86]. It has been reported [87] that the surface Co^{3+} cations on the cobalt oxide electrode can produce surface electronic states by the Jahn–Teller effect (a geometric distortion of a non-linear

molecular system, typically observed among octahedral complexes that reduces its symmetry and energy), which essentially states that in this particular situation, these surface states can capture electrons from the bulk oxide to form excited cationic states $[Co^{3+} + e]$, which can act as the active sites for the alkaline ORR. Therefore, the ORR activity is believed to be directly related to the distribution of Co^{3+} cations among the different coordination sites at the cobalt oxide surface. Xu et al. [86] showed that ORR catalytic activity is sensitive to the number of surface exposed Co^{3+} ions, and the number of sites can be tailored by the morphology of cobalt oxides. Their Co_3O_4 nano-rod structure exhibits a higher activity than the noble Pd catalyst does at the low potential region. However, their experimental support for the higher density of Co^{3+} ions on the surface of the sample with the best performance than others was a very slight shift of the Co^{3+}/ Co^{4+} redox couple in the CV curve, which can be influenced by various operation parameters between samples. Therefore, the less sharp contrast between the all of the nano-rod samples made the conclusion less convincing. Another theory for the ORR mechanism on Co_3O_4 was proposed by Xiao et al. [88] by controllable synthesis of Co_3O_4 nanorods (NR), nanocubes (NC) and nano-octahedrons (OC) with the different exposed nanocrystalline surfaces ({110},{100}, and {111}, respectively), which have different distributions of Co^{2+} and Co^{3+},as shown in **Figure 1.6**. The Co^{3+} cations are present solely on the {110} plane, as shown by surface differential diffraction study [89,90]. Similarly, the crystalline phases, morphology and exposed facets were confirmed by XRD, TEM and high-resolution TEM. Shape-dependent ORR catalytic activity of the Co_3O_4 nanocrystals was clear that both the onset and half-wave potential of ORR on Co_3O_4 NC and OC were close to each other (OC is slightly higher than NC), about 0.08 V

higher than that of Co_3O_4 NR. The theory behind this phenomenon is that the O_2 adsorption/desorption process takes place in a Pauling configuration ($Co…(O_{ads} = O)$), as opposed to Griffths and Bridge-type modes [91], which is involved in the rate-determining step as suggested by the mismatch of the bond angle on the surface and the bulk and also the bond length of the oxygen molecule and adjacent active sites. Therefore, the surface Co^{2+} ($3d^54s^2$) tends to be the active site rather than the surface Co^{3+} ($3d^54s^1$) cations because Co^{2+} can transfer electrons to the absorbed O_2 molecules to weaken and to assist breaking the O-O bond, meanwhile being oxidized to Co^{3+}. This can also partially explain why CoO supported on nitrogen doped carbon nanotubes outperforms its counter part Co_3O_4 in the same structure in ORR in Liang et al.'s work [92–94]. Further discussion will be provided in the next subsection and **Chapter 7**.

In terms of OER studies with Co_3O_4 electrocatlaysts, the water oxidation activity is generally ascribed to the presence of Co^{4+}, which appeared from the $CoO_2/CoOOH$ redox reaction right before the onset of the OER [76][95]. This finding was experimentally supported by Yeo et al.'s work [96], where the OER turnover frequency of cobalt oxide deposited on Au was 40 times higher than that of bulk cobalt oxide by increasing the population of Co^{4+} due to the electronegativity of gold where the activity decreased monotonically in the order Au > Pt > Pd > Cu > Co, paralleling the decreasing electronegativity of the substrate metal. Their conclusions were joined later by Lu et al. through the OER catalyst of gold nanoparticles incorporated in mesoporous cobalt oxides (Au/mCo_3O_4) [97]. DFT calculations have also shown that O binds more strongly to a
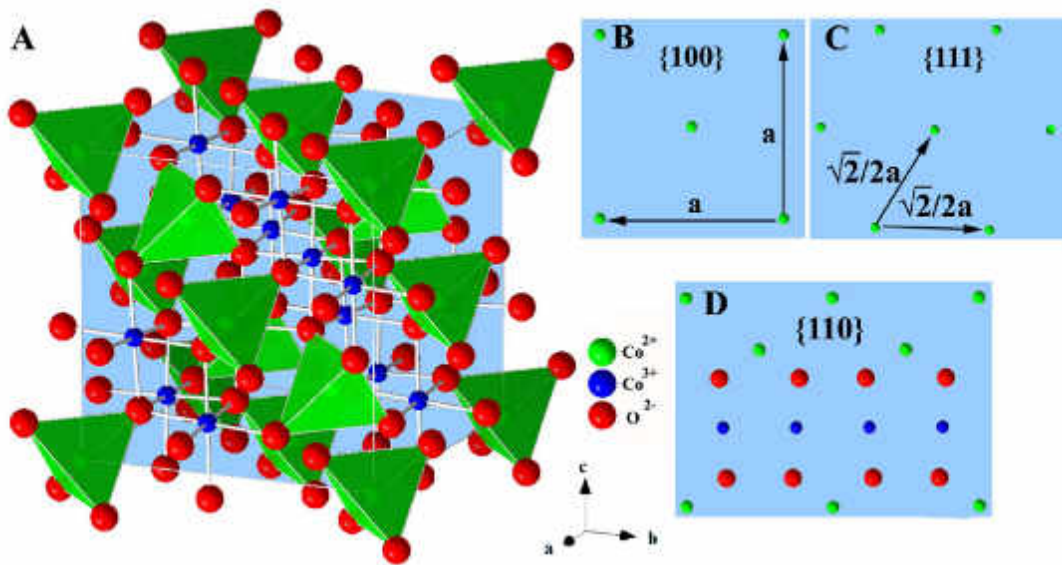
Figure 1.6 Structure models of the spinel Co_3O_4 nanocrystals. (A) Three-dimensional atomic arrangement and (B–D) Surface atomic configurations in the {100}, {111} and {110} planes. Reprinted with permission from ref. [88]. Copyright 2011 Science.

monolayer of Co deposited on Au than to pure Co alone [98]. It is proposed [96][99] that cations with higher oxidation state, Co^{4+} cations in this particular case, can enhance the electrophilicity of the adsorbed O and further facilitate the formation of O-OH via nucleophilic attack by an incoming OH^- anion with an O atom associated with Co^{4+}, which is also beneficial for the deprotonation of the OOH species, via an electron-withdrawing inductive effect, to form O_2. These two steps are normally considered the rate-determining steps for OER on metal oxides, stated at the beginning of this section. Based on the analysis above, the fundamentally different RDS for ORR and OER on cobalt oxides require totally different catalytically active sites on the catalyst surface. Therefore, the ORR/OER activity can be manipulated by the distribution and exposure of corresponding active sites on the surface through synthesis conditions.

b) Nickel Cobalt Oxide

It is well understood that $NiCo_2O_4$ is a low temperature metastable phase, which appears only below ca 400°C in air. In contrast to the normal spinel structure $Co^{2+}[Co^{3+} Co^{3+}]O_4^{2-}$ of Co_3O_4 , $NiCo_2O_4$ has an inverse spinel structure. A number of charge and site distribution models have been proposed. For example, an ionic configuration formula was presented as $Co_x^{2+} Co_{1-x}^{3+} [Ni_{1-x}^{2+} Ni_x^{3+} Co^{3+}]O_4^{2-}$ by Lenglet et al. [100]. But it is well agreed that $NiCo_2O_4$ phase has the best ORR activity among all the nickel doped cobalt oxides [101]. Manivasakan et al. have recently successfully synthesized a series of urchin-like mesoporous three-dimensional hierarchical nanostructures of $Ni_xCo_{3-x}O_4$ [102] to comprehensively develop the relationship between the ORR electro-catalytic activity properties of $Ni_xCo_{3-x}O_4$ and its structure, morphology and composition. Among which $NiCo_2O_4$ was found to possess the highest surface area (123 m^2 g^{-1}), and also a

significantly improved onset potential and current density for ORR compared with previously reported nickel cobalt oxide structures. The mechanism behind the improved ORR activity was claimed that the improved textural features of $NiCo_2O_4$ could provide sufficient exposed Ni^{3+} and Co^{3+} species on the octahedral site to produce more surface electronic states in alkaline media, which is consistent to the surface cation distribution theory and Jahn-Teller effect mentioned above [102].

Other morphologies of nickel cobalt oxide were also produced as bifunctional ORR/OER electrocatalysts [101][103,104] such as porous hollow nickel cobalt oxide tubes with the diameter of 100 nm supported on pure acetylene carbon black as an effective bifunctional catalyst for rechargeable $Li–O_2$ batteries [105]. Mesoporous $NiCo_2O_4$ nanoflakes grown on a three-dimensional (3-D) porous nickel foam as a decoupled OER catalyst in hybrid lithium-air batteries for the systematic study of how the air electrode configurations affect performance of cells with the same catalysts [106]. The reason that $NiCo_2O_4$ has better OER catalytic ability than NiO is proposed by Rasiyah et al. [107] that transition between valence states of cobalt generally occurs at lower potential than the corresponding transition of nickel, therefore, the onset potential for OER on $NiCo_2O_4$ is lower [108].

c) Lithium Cobalt Oxide

Among numerous cobalt-based binary oxides, $LiCoO_2$ has been among the most studied because of its possible application as a cathode material for lithium-ion batteries. The $LiCoO_2$ with a lithiated spinel structure $\{Li_2\}_{16c}[Co_2]_{16d}O_4$ (the Co^{3+} ions occupying all the 16d octahedral sites and the Li^+ ions occupying all the 16c octahedral sites of the spinel framework, space group: *Fd3m*) can be synthesized at a relatively low temperature

(400 ºC). This spinel structured $LiCoO_2$ has also been applied as an OER catalyst by Maiyalagan et al. [109] and showed higher OER activity than $LiCoO_2$ with a layered $NaFeO_2$ structure (space group: $R\overline{3}m$) synthesized at high temperatures (800 ºC). It was also shown that chemically delithiated $Li_{1-x}CoO_2$ (achieved by extracting lithium with NO_2BF_4 in acetonitrile) possessed high ORR activity, making the spinel-type $Li_{0.5}CoO_2$ a potential bifunctional electrocatalyst for rechargeable metal-air batteries. Other authors have attributed the activities of the delithiated cobalt oxide to the presence of Co_4O_4 cubane subunits, and a pinning of the $Co^{3+/4+}$: 3d energy with the top of the O^{2-}: 2p band facilitating the formation of O–O bonds easily leading to an easier release of oxygen [110,111]. However, the OER onset potential is still 0.1 V lower than IrO_2 and durability when screened at 1.7 V for only 5 hours, raises doubts whether the oxygen rich structure can be a durable bifunctional catalyst, especially for OER. In the case when lithium exists as a dopant in cobalt oxide, Wu et al. achieved the best OER performance with $Li_{0.21}Co_{2.79}O_4$ synthesized through a nitrate assisted thermal decomposition method. Their cell achieved a high current density at a voltage of 2.05 V at temperatures of 45 ºC in a single non-precious metal alkaline anion exchange membrane water electrolyser [112], due to the changes in cation distribution $((Co^{2+}_1)_A(Co^{3+}_2)_BO_4$ for Co_3O_4 and $(Li^+_{0.21}Co^{2+}_{0.58}Co^{3+}_{0.21})_A$ $(Co^{3+}_2)_BO_4$ for $Li_{0.21}Co_{2.79}O_4$, electronic conductivity: 2.1 ± 0.2 S cm^{-1}) and variation in binding energy of surface oxygen. The doped cobaltite oxide has better OER activity due to the better electronic conductivity and cation distribution, as compared by Nikolov and co-workers, where the electrochemical behaviors of binary cobalt oxide $M_xCo_{3-x}O_4$ (M = Li, Ni, Cu) were compared and it was found that the activity of the spinels increased in the order $Co_3O_4 < Ni_xCo_{3-x}O_4 \ll Cu_xCo_{3-x}O_4 < Li_xCo_{3-}$

$_x$O$_4$ [113]. The stability of Li$_{0.21}$Co$_{2.79}$O$_4$ was examined under continuous operation for 10 h at above 2 V and at 30 ºC. The author chose a higher voltage to justify the durability of the doped cobaltite than most of other reports, however, a voltage increase of more than 0.2 V only in the first 10 hours was not a very excellent starting performance for electrolyzers, and there is also stability improvement potential for membrane and ionomers in alkaline water electrolyzers.

Other cobalt oxides such as Cu$_x$C$_{3-x}$O$_4$ and Mn$_x$C$_{3-x}$O$_4$, whose complex structures and cationic distributions (Co^{3+}[Mn^{2+}Co^{3+}]O$_4$ [114–117], Co^{2+}[Mn$_x^{3+}$Co$_{2-x}^{3+}$]O$_4$ [118–121], or Co^{2+}[Mn^{4+}Co^{2+}]O$_4$ [122], etc.) have been numerously proposed in literature due to the multivalence of Mn ion depending on the preparation method and the calcination temperature, have also been proposed as an attractive non-precious oxygen electrocatalyst for oxygen reactions [123]. Some examples as reversible ORR/OER catalysts would be further discussed below in the next subsection.

Although mixed transition metal oxides have shown some promise as ORR, OER and reversible ORR/OER electrocatalysts after some modification, their performance is essentially always limited as direct electrocatalysts in fuel cell applications by their low electrical conductivity. Therefore, the introduction of support materials with high electronic conductivity is almost always needed in order to not only increase conductivity, but also enhance their dispersion and often their durability.

1.5.2 Advanced Carbon-Based Hybrid Material as Candidates for Reversible ORR/OER Electrocatalysts in Alkaline Media

a) In-situ vs. ex-situ synthesis processes

In this section, carbon-catalyst hybrid materials with an inorganic component

attached to the outer surface of CNTs, instead of filling CNTs, will be discussed. These structures maintain the conductive CNT inner layers while resulting in highly functionalized outer layers as the active sites for both oxygen reactions. These CNT-inorganic hybrids can be realized by various synthesis strategies, which can be categorized as ex-situ and in-situ techniques. The ex-situ approach first produces the inorganic component in isolation, possessing the desired dimensions and morphology. Then, the surface is modified and the inorganic is attached to the surface of the CNTs via a second process, such as covalent, noncovalent, or electrostatic interactions. Simply put, the formation of the inorganic components and the combination with the support are two independent steps [124,125]. On the contrary, in-situ approaches carry out the synthesis of the inorganic component in the presence of pristine or functionalized CNTs, onto which the inorganic material is grown as particles, nanowires, or thin films [126].

Ex-situ processes tend to have weaker bonding between the inorganic components and the supports, which may not be good for long-term catalyst stability, particularly for the OER where a very harsh oxidizing condition exists as well as mechanical issues brought on by constant gas evolution from the catalyst surface. These structures may be more feasible in ORR-only systems where physical blends of graphene–like carbon and –Ni–a-MnO_2 and –Cu–a-MnO_2 have already been demonstrated with comparable activities to Pt/C and reasonable durability [127,128]. Additionally, Guo et al. synthesized monodisperse Co/CoO nanoparticles (NPs) and deposited them ex-situ onto a graphene (G) support through solution-phase self-assembly, and the resulting G–Co/CoO exhibits a comparative activity and better stability than the commercial C–Pt NPs in KOH (0.1 M) electrolyte [93].

b) Treatment of advanced carbon materials

To enhance the bonding between support and metal oxides, a chemical bond is often introduced between the two, which is more feasible using in-situ methods. In order to grow transition metal oxides onto CNTs, forming covalent bonds between the oxides and supports to promote adhesion, the CNTs must be functionalized initially to provide enough anchoring sites for the metal oxides. One of the most convenient and energy-saving ways to introduce oxygen functional groups to carbon materials is chemical oxidation, which is typically achieved by using concentrated acids or bases, oxidants such as hydrogen peroxide and potassium permanganate, or the combination of both [129–131]. Various oxygen functional groups are introduced during this process including carboxyls, carboxylic anhydrides, and lactones, as well as aldehydes, ethers, hydroxyl groups exhibiting phenolic character, and carbonyl groups such as quinones or pyrones [132–134]. Datsyuk et al. measured the oxidation degree of multi-walled CNTs treated by different oxidation agents through Raman spectroscopy and X-ray photoelectron spectroscopy [129]. They concluded that the increase of the degree of surface oxidation follows the trend of hydrochloric acid < ammonium hydroxide/hydrogen peroxide < piranha < refluxed nitric acid. Oxidative treatment, with the exception of nitric acid, did not lead to the production of additional defects on the outer walls of the multi-walled CNTs. Therefore, the oxidants can be used to serve the purpose of introducing more anchoring sites for metal oxide growth were narrowed down to nitric acid and potassium permanganate [131]. More experimental details of the influence of different oxidants will be provided in **Chapter 7, Section 7.2.1**. Pre-treated advanced carbon can be used as

direct substrate for metal precursors to react on in various synthesis methods, which will be discussed below.

c) Hydrolysis in alcohol-water system/hydrothermal reaction

Dai et al. developed a two-step procedure to synthesize metal hydroxides and oxides on graphene oxides (GO) or oxidized CNTs. This method basically includes a hydrolysis of metal precursor salts selectively on oxidized carbon as the first step with a secondary step of either hydrothermal/solvothermal treatment or thermal annealing in the gas phase to convert the coating into crystalline metal hydroxides or oxides [135]. In the first step, metal ions are added to GO in solution to interact with oxygen functional groups on GO and adsorb onto these groups. At these adsorbed sites, hydrolysis of metal ions is initiated to nucleate and grow metal hydroxides or oxides. Nucleation and growth could also take place in free solution, which would compete with selective nanoparticle nucleation and growth on GO and is undesired. Their work found that there are several important parameters to control the competition over free growth in solution, such as the usage of a mixture of solvents and reaction temperature control. Various additives, such as ammonia and other complex compounds, could affect the reaction rate as well. The annealing temperature and atmosphere in the following thermal treatment step can impact the phase, size and morphology of the materials grown on GO.

Hybrid materials of various nanocrystals and nanoparticles with nano-carbon materials were developed by this method for several electrochemical and photocatalytic applications such as supercapacitors, batteries, electrolyzers and fuel cells. Among these materials, good candidates for bifunctional ORR/OER catalysts have been attained. Strongly coupled Co_3O_4–N-mrGO (nitrogen doped mildly reduced graphene oxide)

hybrid synthesized from the above two-step method exhibited great performance towards both ORR and OER reactions in KOH solutions, indicating the potential to be good non-precious metal bifunctional candidate [136]. This hybrid catalyst exhibited high ORR activity with an onset potential of 0.9 V vs. the reversible hydrogen electrode (RHE) during rotating disk electrode (RDE) measurements, which made it the most active ORR catalysts based on Co_3O_4. A complete four-electron reduction was shown using Koutecky–Levich plots from 0.60–0.75 V. Different from the proposed ORR active sites of Metal-N species in Fe- or Co-N/C catalysts [137] prepared at much higher temperatures (600–1,000 ∘C) with lower metal loadings (<1–2 at% of metal), the Co oxide species at the interface with graphene is believed to be the active site for the above high Co loading Co_3O_4–graphene hybrid catalyst, obtained at lower synthesis temperature. Also, the much improved ORR activity than raw Co_3O_4 catalyst was analyzed through the synergistic effect between Co_3O_4 and the N-mrGO by the possible formation of interfacial Co–O–C and Co–N–C bonds via X-ray absorption near edge structure measurements. A higher electron density at the O site and a lower electron density at the Co site consequently suggested a higher ionic Co–O bonding in the hybrid. The ORR activity was further improved by by substituting half of the Co^{3+} in the spinel structure of Co_3O_4 with Mn^{3+} due to an increase in electron density [77]. But when the Mn/Co ratio is larger than one, the ORR activity started to decrease due to a phase transition from a cubic spinel to a tetragonal spinel phase [138], which possesses a lower intrinsic ORR activity than the cubic phase [28]. Similar cobalt oxide based hybrid structure with other advanced carbon material support such as mildly oxidized multiwalled carbon nanotubes (CNTs), synthesized via modified procedure showed further improved properties [92].

The half-wave potential in the linear sweep voltagram of Co_3O_4 supported on nitrogen doped CNT (NCNT) was similar to Co_3O_4/N-rmGO), about 35 mV more negative than Pt/C catalyst. Also, when the second hydrothermal step was replaced by a thermal annealing at 400 °C in a NH_3/Ar atmosphere, the peak voltammetric current density on the obtained CoO/NCNT catalyst was increased by ~30%. In a setting that is more similar to a practical fuel cell operation, the authors loaded catalysts on Teflon-coated carbon fiber paper, where CoO/NCNT exhibited significantly higher ORR current than the Co_3O_4/N-rmGO hybrid, possibly due to a higher electrical conductivity, which can be observed in electrochemical impedance spectroscopy measurements in the ORR region at 0.8 V for various catalysts. The OER electrocatalytic activities of the above Co_3O_4/N-rmGO hybrids was similar to that of the Co_3O_4 and graphene physical mixture, indicating that a strong coupling between Co_3O_4 and graphene is particularly important for ORR, though less critical for OER [139]. And the $MnCo_2O_4$ /N-rmGO hybrid exhibited lower OER currents than Co_3O_4/N-rmGO due to the reduction of Co^{3+} OER active sites (Co^{3+}/Co^{4+} transition) with Mn^{3+} substitution, but still higher than physical mixture. Therefore, these hybrid structures can be considered as reversible ORR/OER candidates.

Ning et al. achieved highly active and stable hybrid spinel $CuCo_2O_4$ nanoparticle electrocatalysts supported on N-doped reduced graphene oxide (N-rGO) using a similar solvothermal method [140]. The introduced Cu^{2+} ions have excess octahedral stabilization energy and should preferentially occupy the octahedral sites of the spinel structure. They increase the lattice parameter due to a larger ionic radius in the octahedral coordination (0.73 Å) than that of Co^{3+} ions (0.55 Å for low spin and 0.61 Å for high spin). The ORR onset potential for Co_3O_4/N-rGO hybrid is ~30 mV more positive than

that of the $CuCo_2O_4$/N-rGO. Singh et al. proposed a similar approach to synthesize Co_3O_4 supported on N-doped graphene with preferential exposure of low surface energy facets, which showed a low overpotential (~280 mV) for OER at a current density of 10 mAcm^{-2} [141]. Gong et al. synthesized and analyzed a highly OER active phase - nickel−iron layered double hydroxide (NiFe-LDH) nanoplates, which can be used as a novel electrocatalyst material. When grown on mildly oxidized multiwalled carbon nanotubes (CNTs), the NiFe-LDH/CNT hybrid exhibits even higher electrocatalytic activity and stability for OER than commercial precious metal Ir catalysts in alkaline solutions due to an electron transfer enhancement [142,143]. The synergistic effect between NiO alone and graphene support was explained by the pinning effect of hydroxyl/epoxy groups on the Ni atoms of NiO based on first- principles calculations in Zhou et al.'s work. Wang et al. synthesized NiO nanoparticles supported on metal-nitrogen-carbon sheet to achieve improved OER performance via the synergistic effect between the NiO and the support materials. Before they grew inorganic metal oxides, they further functionalized the nitrogen doped graphene oxide with transition metals such as Co and Fe with the aid of polymers to achieve Fe–nitrogen–carbon (FeNC) and Co–nitrogen–carbon (CoNC) sheets, respectively, in order to further increase the active sites for OER [144–146].

d) Chemical (Polyol) reduction process

Chemical reduction is typically a one-pot solvothermal strategy using metal acetate or nitrate as metal precursors and desired advanced carbon materials in polyols, which serves as the dispersing agent as well as the reducing agent. Traces of ammonia and thiourea are sometimes added to produce nitrogen and sulfur functional groups on the carbon support to create better anchoring sites or chalcogenides at the same time.

Zhang et al. synthesized strongly coupled $NiCo_2O_4$ supported on reduced graphene oxide nanosheets through a polyol reduction route, showing a ORR onset potential of 72 mV more negative than that of the commercial 20 wt% Pt/C catalyst. The metal ions were reduced to nucleate on abundant functional groups on GO by refluxing in ethylene glycol at elevated temperature [147]. After generating a uniform layer of Ni-Co-glycolate conformally coated on both sides of the GO sheets, high-temperature annealing was carried out in air to further achieve $NiCo_2O_4$ nanocrystals on the surface [78]. Liu et al. used a similar ethylene glycol reduction method to achieve the novel hybrid of $NiCo_2S_4$ nanoparticles grown on graphene in situ. This $NiCo_2S_4$ supported on N/S double-doped reduced graphene oxide material is described as an effective bifunctional nonprecious electrocatalyst. It has much better durability for alkaline ORR in comparison with commercial Pt/C catalyst with a 0.08 V reduction of onset potential but better methanol tolerance ability as well as promising OER performance in both neutural and basic media [148]. Yan et al. obtained cuprous oxide (Cu_2O) nanoparticles dispersed on reduced graphene oxide (RGO) using diethylene glycol as both solvent and reducing agent [149]. The Cu_2O/RGO exhibits the same onset potential, 0.05 V more negative half-wave potential when compared with commercial Pt/C, as well as remarkable tolerance to methanol and CO during the ORR.

Except the two major solvothermal based methods mentioned above, many other novel and non-mainstream synthesis routes have been proposed in literature to produce advanced carbon-based transition metal oxide hybrid structure for oxygen reduction and evolution reactions. Mao et al. designed and fabricated hollow crumpled-graphene with supported CoO nanohybrids (CG–CoO) through a one-step aerosolization approach. In

this aerosolization/high-temperature-induction procedure, the suspension containing GO with precursor ions (Co^{2+}) was nebulized to generate micro-size aerosol droplets that flowed through a tube furnace at elevated temperature. The rapid evaporation of the solvents in the tube led to a shrinkage of GO sheets and the subsequent compression the GO sheets into crumpled balls with a submicrometer size. Simultaneously, CoO nanocrystals assembled on both external and internal surfaces of the CG balls during the solvent evaporation and the GO crumpling process [150]. This three-dimensional structure exhibited much more stable performance as bi-functional catalysts for both ORR and OER in alkaline solutions compared with conventional two-dimensional graphene. This was due to the prevention of active surface area loss caused by natural restacking of graphene sheets. Electrodepostion is another approach adopted by researchers as the initial synthesis step. Zhang et al. [151] and Wang et al. [152] decorated graphene with Fe_2O_3 nanoclusters and carbon paper with flower-like 3D MnO_2 ultrathin nanosheets, respectively, as an O_2 electrode for high energy rechargeable Li–O_2 batteries using an electrochemical approach in iron and sodium salt electrolyte.

Many of these hybrid structures discussed above exhibited superior performance than their Pt/C catalyst benchmark in alkaline solution. The improved ORR/OER activities were summarized into a few groups: i) the doped nitrogen in the carbon network provides extra active sites, ii) the metal-support coupling interactions or the carbon-nitrogen-metal triple junction enhances electron transfer, and iii) the advanced morphology or structure of the materials increases the exposure of active sites. However, few of these proposed theories were truly experimentally confirmed or fundamentally explained the ORR/OER mechanism. In terms of durability, though some of these

materials have shown good short-term ORR durability, the long-term exposure to harsh and oxidizing environment during OER may cause the thermal instability of carbon and oxidized surface. Therefore, a thorough discussion on and investigation into stability is still a critical need. In fact, durability, not activity, is often the primary driver for industrial adoption in these systems, though, of course, a combination of both stability and durability is desired. In **Chapter 7**, the durability issue of the carbon-based hybrid material as bifunctional catalyst in alkaline media will be explored.

CHAPTER 2 – EXPERIMENTAL

In this chapter, the experimental techniques and details regarding materials synthesis and other experimental protocols are introduced including the conditions for physical characterization techniques such as XRD, XPS, BET gas adsorption, SEM, EDS, TEM, HRTEM, UV-Vis, FTIR, Raman, as well as electrochemical characterization technique and equipment are introduced as common approaches.

2.1 Material Synthesis

2.1.1 Synthesis of Titanium modified Tungsten Oxide ((Ti)-WO₃) and Tungsten Carbide

The first step to prepare titanium doped tungsten carbide was the preparation of a WO_3+Ti sol: the solution of hydrogen peroxide (31 wt%, Sigma-Aldrich) and glacial acetic acid (Sigma-Aldrich) were mixed 1:1 by volume in an iced bath with a small amount of deionized water. Metallic tungsten (Sigma-Aldrich) was then added, and stirred for 24 hours. This liquid was refluxed for 18 hours at 55 °C under vacuum to recover a powdered tungsten peroxy acid product. The powder was reacted with ethanol to form the tungsten-peroxy ester derivative. At last, titanium isoproxide (Sigma-Aldrich) was added to make infiltrate the tungsten species with 8 at% Ti. The next step of the synthesis procedure was to form a mixed-metal oxide by drying the WO_3+Ti sol on a hot plate at 60 °C to make a gel, and then calcining at 500 °C in a muffle furnace for 24 hours. The oxide was then heated in argon atmosphere in a tube furnace at 1300 °C for 3 hours, with a ramping rate of 3 °C/min to form the final mixed metal carbide.

2.1.2 Synthesis of Iridium/Iridium Oxide Supported on Tungsten Doped Titanium Oxide

Through Template-free Polyol Reduction

1.2 g of sodium hydroxide pellets were dissolved into 150 ml ethylene glycol to make a 0.2 M NaOH solution under continuous stirring and slight heating. Next, 0.7 g of commercially available W-TiO$_2$ (Sigma-Aldrich) support was added and the solution was sonicated and stirred for 45 minutes. Then, 0.7 g of the metal precursor (IrCl$_3$.xH$_2$O) was added and mixing was continued for 3 hours. A homogeneously dispersed caramel yellow liquid mixture was obtained, and then was heated to 175°C and reacted for 3 hours. The resulting mixture was cooled to room temperature, removed from heat and mixed into 1.5 L of DI water. While mixing, nitric acid was slowly added with a pipette until the solution pH was approximately 1. The solution was stirred for 3 additional hours. After precipitation, the particles were washed with DI water through centrifugation 3 times, until clear supernatant was obtained. The collected nanoparticles were dried in a vacuum oven at 110°C for 4 hours. Several parameters such as the precursor to support ratio, the initial pH value and the reaction temperature were varied to manipulate the particle size of supported iridium, as shown in **Table 2.1**.

2.1.3 Synthesis of Tin Doped Indium Oxide (ITO) Support Material

To prepare the ITO nanoparticles (NPs), a slurry of indium acetylacetonate (In(acac)$_3$) (99.99+%, Sigma-Aldrich) and tin bis-(acetylacetonate) dichloride (Sn(acac)$_2$Cl$_2$) (98%, Sigma-Aldrich) precursors was prepared in oleylamine (70%, Sigma-Aldrich). The ratio of In to Sn atoms was 19:1 (14.11 mg of tin bis-(acetylacetonate) dichloride was used). Then, the slurry was heated at 200 °C for 1.5 hours in air to produce a dark yellow suspension. The ITO nanoparticles (NPs) were

Parameters	Batch 1	Batch 2	Batch 3	Batch 4
IrCl$_3$.xH$_2$O (g)	0.7	0.7	1.3	1.78
(W-)TiO$_2$ (g)	0.7	0.7	0.7	0.48
Ethylene glycol (mL)	150	125	350	400
NaOH concentration (M)	0.2 (1.2g)	0.03 (0.15g)	0.2 (2.8g)	0.2 (3.2g)
T (°C)	175	175	120	120

Table 2.1 Parameters of synthesis procedure for different batches of iridium/iridium

oxide supported on tungsten doped titanium oxide.

precipitated by the addition of ethanol (40 ml) to the suspension, and the supernatant was removed by centrifugation at 2500 RPM for 6 min. After washing with ethanol again, white ITO NPs were collected. They were heated at 80 °C for 0.5 hours to evaporate the remaining ethanol and then further heated at 500 °C for 2 hours in air for crystallization.

2.1.4 Pt Deposition on ITO and (Ti)-WO$_3$ Support Materials

The as-synthesized ITO was deposited onto a mirror-polished 5 mm-diameter glassy carbon electrode (GCE) (Pine Research Instrumentation). The GCE was polished to a mirror finish using a 0.05 µm alumina-particle suspension (Buehler) on a moistened polishing microcloth (Buehler) and washed ultrasonically with ultra-pure 18.2 MΩ deionized water (from a Millipore Direct-Q 3UV purification system) for 4 min prior to each experiment. The ITO/water dispersion was prepared (0.1 mg/ml ITO) by sonication for 30 minutes, forming an opaque and uniform suspension. 20 µl of the suspension was added dropwise onto the GCE with a micropipet and then dried in air for 60 min on an inverted rotating disk electrode (RDE) at 300 RPM (Pine Research Instrumentation). A homogeneous light gray thin film was obtained on top of the GCE. The loading of ITO NPs on the working electrode was approximately 10.2 µg cm^{-2}.

The method of Pt deposition onto the ITO supports was a galvanic displacement of a Cu monolayer. Cu underpotential deposition was carried out in a custom-built three-electrode electrochemical cell (Adams & Chittenden Scientific Glass) under N$_2$ atmosphere to avoid Cu oxidation. Cu was electrodeposited by cyclic voltammetry (CV) (Autolab PGSTAT302N Potentiostat, Eco Chemie) without rotation in a 0.05 M H$_2$SO$_4$/0.05 M CuSO$_4$ solution. The working electrode potential was cycled between 0.0 and 0.3 V vs. NHE for two cycles at a sweep rate of 50mV/s. The resulting electrode was

rinsed with copious Millipore water, transferred to a dilute, deaerated 0.001 M K_2PtCl_4 (Acros Organics)/0.05 M H_2SO_4 solution and was kept there for 5 minutes at room temperature, which facilitated the galvanic displacement of Cu by Pt [153]. Then the electrode was rinsed with copious Millipore water again. Lastly, a thin layer of Nafion® diluted to 0.05wt% from 5% Nafion® DE-520, DuPont was pipetted onto the working electrode in order to attach the catalyst to the GCE during electrochemical testing. The Nafion® film was dried at room temperature under inverted rotation at 300 RPM in air. The loading of Pt onto the electrode was 6.3 μg cm^{-2} (determined by calculating the charge difference during the anodic and cathodic scan [154]). The procedure for depositing Pt on the (Ti)-WO_3 support materials was the same; ITO was simply replaced with (Ti)-WO_3 in the procedure.

2.2 Calculating the Electrochemically Active Surface Area of Iridium Oxide

2.2.1 Electrodeposition of Ir and IrO_2 Thin Films onto Polycrystalline Gold Electrodes

A 5 mm-diameter disk-type gold working electrode (Pine Research Instrumentation) was polished to a mirror finish using a 0.05 μm alumina-particle suspension (Buehler) on a moistened polishing microcloth (Buehler) and washed ultrasonically with ultra-pure 18.2 MΩ deionized (DI) water (Millipore Direct-Q 3UV purification system) for 4 min prior to each experiment. A Pt flag and Hg/$HgSO_4$ electrode (CH Instruments) were used as counter and reference electrodes, respectively. The working electrode was first cleaned by cycling the potential between 0 V and 1.5 V at 200 mV/s for 50 cycles in 0.5 M H_2SO_4 (Acros Organics) to remove any surface impurities.

The electrode was transferred to a de-aerated 0.5M H_2SO_4/0.04 mM H_2IrCl_6 solution (Dihydrogen hexachloroiridate (IV) hydrate (99.9%), Fisher Scientific) for Ir electrodeposition. Ir deposition was carried out in a custom-built three-electrode electrochemical cell (Adams & Chittenden Scientific Glass) in N_2 atmosphere (by bubbling with UHP grade nitrogen (Airgas) for 20 minutes before operation) to avoid immediate Ir oxidation. Ir was electrodeposited by chronoamperometry (Autolab PGSTAT302N Potentiostat, Eco Chemie) without rotation at 0.2 V vs. the normal hydrogen electrode (NHE) for various lengths of time in order to achieve different loadings. Intermediate CVs during electrodeposition were collected to monitor the growth of the Ir particles by observing the increase of the hydrogen evolution current with increased cycle number. All potentials are reported versus NHE.

After Ir deposition, the electrode was washed with a copious amount of deionized water to remove surface $IrCl_6^{3-}$ and $IrCl_6^{2-}$, and transferred to a 0.5 M H_2SO_4 electrolyte saturated with nitrogen. CVs were carried out between 0.05 and 1.5 V at 200 mV/s for 50 cycles to oxidize the surface Ir to IrO_x. After oxidation, the electrode was rinsed with copious DI water and dried in air.

2.2.2 Adsorption of Zinc Cations onto IrO_x Catalysts

Zinc cation adsorption onto the IrO_x electrode surface was adopted to estimate the true ex-situ ECSA by multiplying the surface area occupied by each zinc cation (17 $Å^2$) by the total number of adsorbed zinc cations. The adsorption mechanism behind this method is essentially an ion-exchange adsorption on hydrated surfaces: water reacts with the iridium oxide surface, adding hydrogen to the oxygen atoms, and hydroxyls to the metals, resulting in a surface of metal-hydroxides, and bridging oxygens [155]. Surface

complexation of the surface OH groups takes place through the release of acidity. At pH values above the point of zero charge, the surface has a net negative or anionic charge, attracting cations and promoting cation exchange reactions, including the absorption of Zn^{2+}, which is shown in **Equation 2.1**. After adsorbing zinc ions onto iridium oxide, the zinc surface area can be correlated with the ex-situ pseudocapacitive charge on both electrodeposited IrO_x and powder IrO_x catalysts, obtaining a constant similar to the conversion factor for Pt catalysts (with units of $\mu C/cm^2$) to estimate the ECSA of iridium oxide through a simple CV.

$$Ir \overset{OH}{\underset{OH}{\diagup}} + Zn^{2+} \longrightarrow Ir \overset{O}{\underset{O}{\diagup}} Zn + 2H^+ \qquad (2.1)$$
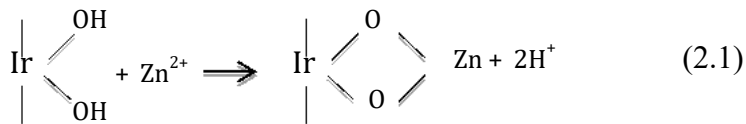
An ammonium chloride solution containing zinc cations was obtained by dissolving white zinc oxide powders (Fisher Scientific) into 0.35 M hydrochloric acid (37%, Fisher Scientific). Ammonium hydroxide (28%, Fisher Scientific) was added as the source of the ammonium ions until the pH was between 9 and 10 in order to cover the surface with anionic charge to attract cations. The resulting concentration of zinc cations was 0.045 mM. The oxidized electrode was immersed into this solution overnight to allow the zinc cation adsorption on IrO_2 to reach equilibrium.

2.2.3 Quantifying Zinc Adsorption by UV-Vis

Because the adsorption of zinc ions onto the electrode results in very small changes in its concentration, titration [156] may not be the most reliable method to quantify the zinc ions. Therefore, the concentration change was determined by UV-Vis spectrophotometry. UV-Vis measures the ultraviolet or visible light absorbed by molecules containing π-electrons or non-bonding electrons to determine the molecule

concentration in the solution.

A standard absorption intensity-zinc cation concentration curve was determined by measuring the adsorption intensities of solutions with known zinc cation concentration (pH and the concentration of other ions were kept the same). Before each test, the solutions were joined by complexing indicator Eriochrome Black-T (EBT, [1-(1-hydroxy-2-naphthol azo) 6-nitro-2-naphthol4-sulphonic acid sodium salt]). The EBT concentration was held constant at 0.005 mM greater than the highest concentration of zinc cations tested. The indicator is blue in basic solutions itself but turns pink-red when it chelates with Zn^{2+} ions, turning the solutions purple. Therefore, the purple intensity can be correlated with the number of zinc cations in the solution.

After obtaining the standard UV-Vis intensity-zinc cation concentration curve, it was straightforward to find the number of zinc cations adsorbed onto the IrO_2 surface by dipping the electrode into a zinc cation solution and then detecting the intensity difference of the purple solution before and after adsorption. The ECSA of each electrode was determined by multiplying the total number of adsorbed zinc ions by 17 $Å^2$ per zinc ion [157].

2.2.4 Preparation of IrO$_2$ Thin Films from Powder Catalysts onto Polycrystalline Gold Electrodes

To extend the Zn-adsorption ECSA method to commercially relevant catalysts, IrO_x thin-film electrodes were made from IrO_x catalysts obtained from Proton OnSite. Before the film preparation, the IrO_x powders were physically characterized. SEM was used to investigate the surface morphology. Nitrogen adsorption analysis was performed with a Micromeritics 2020 at 77 K and a dose of 3 cm^3 (degas at 105 ^oC for 12 h) to find

the BET surface area of the powders. The pore size distribution of the catalyst powders were obtained from the Barret, Joyner and Halenda (BJH) method built into the ASAP 2020 V 3.04 operating software.

Preparing thin film electrodes from the IrO_x powders began with preparing a 24% isopropanol solution by mixing 6 mL of isopropanol and 19 mL of DI water in a 25 mL volumetric flask. Next, 18.5 mg of IrO_x powder was placed into a 50 mL volumetric flask and the 25 mL of 24% isopropanol solution was added. Finally, 100 μL of 5 wt% Nafion® ionomer DE-520 (DuPont) was added to the IrO_x/isopropanol solution, resulting in an ionomer: catalyst ratio (wt) of 5:1. The catalyst 'ink' was then placed in an ice bath and sonicated for 30 minutes. Droplets (20-40 μL for different mass loading) of the dispersed ink were pipetted onto the mirror-finish gold electrode so that it completely covered the gold electrode. The ink droplet was dried in air at room temperature under rotation at 300 rpm for 30 minutes, which yielded a black thin film that homogeneously covered the entire surface of the electrode. The catalyst loading on the electrode was 0.075-0.15 mg/cm^2. In order to fully oxidize the catalyst surface, CVs were carried out between 0.05 and 1.5 V at a scan rate of 200 mV/s for 50 cycles, identical to the electrodeposited IrO_x in **Section 2.2.1**.

2.2.5 IrO_2 ECSA Calculation

CVs for calculating the IrO_x pseudocapacitive charge on the ex-situ disk electrodes were collected between 0.0 and 1.5 V in N_2-saturated 0.5 M H_2SO_4 electrolyte at a scan rate of 50 mV/s. OER polarization curves for IrO_x were collected by scanning the potential from 1.0 V to 2.0 V at a rate of 5 mV/s while rotating the disk electrode (RDE) at 1600 rpm. The current density at 1.6 V from the oxygen evolution polarization

curve was used to determine the specific and mass activities of the catalyst.

To determine the ECSA calculation in-situ in an operating PEM electrolyzer, IrO_x anode CVs were collected using Fuel Cell Technologies hardware modified for electrolysis-most notably, the graphite flow field and the gas diffusion layer (GDL) on the oxygen side of the cell were replaced with a titanium flow field and titanium GDL for stability at high potentials. Catalyst coated membranes with 25 cm^2 active area were provided by Proton OnSite. The cathode material was Pt black and the anode material was IrO_x. The catalyst: ionomer (5 wt% Nafion® dispersion) ratio, by mass, was 1:1. The single-cell tests were carried out at room temperature with fuel supply control through a Teledyne Medusa™ RD fuel cell station (Teledyne Energy Systems, Inc.). CVs were obtained with a Solartron SI 1287 Potentiostat. The electrolyzer was operated by circulating excess N_2 saturated DI water through the anode side of the cell with a small pump, and feeding the cathode side with 100% humidified hydrogen at 0.5 L/min.

2.3 Physical Characterization of Catalyst and Support Materials

In this work, the crystal structure and average grain boundary size of both the electrocatalysts and supports were evaluated by Bruker D8 Advance X-ray diffractometer with a Cu Kα_1 ceramic X-ray tube (λ= 0.1540562 nm) and a LynxEye Super Speed detector. The diffraction angle (2θ) was varied from 5° to 90° at a scanrate of 0.0285°/second.

The surface morphology of the metals and metal oxides were investigated using a FEI Quanta 250 FEG scanning electron microscope (SEM) with a field emission source and images were captured using an Everhart-Thornley SE (secondary electron) detector with an electron accelerating voltage of 20 kV, a 3.0 nm spot-size and a sample height of

10 mm. The sample elemental composition was explored by Energy Dispersive X-ray Spectroscopy (EDS) with a Genesis Apex System from EDAX, AMETEK, Inc., using an electron accelerating voltage of 20 kV and a working distance of 10 mm. The morphology and elemental distribution of certain samples in this study were investigated by a fully digital Field Emission Scanning Electron Microscope (FE-SEM) in the Strata 400 STEM DualBeam system equipped with Focused Ion Beam (FIB) technology and Flipstage/STEM assembly, which allows for complete in-situ sample preparation and high-resolution analysis. Material nanostructure was investigated by transmission electron microscopy (TEM) with a Tecnai T-12 and high-resolution TEM with a FasTEM JEOL 2010 with 200 kV thermionic electron source. The samples for TEM were prepared by ultrasonically dispersing particles in ethanol and drying them on Holey carbon-coated copper grids.

Investigation of material surface composition before and after electrochemicial testing was done using X-ray photoelectron spectroscopy (XPS). The XPS system was a Physical Electronics multiprobe with a Perkin–Elmer dual anode X-ray source and a Kratos AXIS-165 surface analysis system. Unmonochromatized Al K% radiation (1486.6 eV) was used at 250 W and 15 kV. The pressure in the analysis chamber was always ~10^{-8} Torr or less. The full survey was taken at 100 eV pass energy with a scan rate of 1 eV/s and the high-resolution scans were conducted at 50 eV pass energy with a scan rate of 0.1 eV/s. The spectra were calibrated with respect to graphitic C 1s electron bond at 284.6 eV. The backgrounds were determined using Linear or Shirley-type background correction and the curves were fitted with Gaussian/Lorentzian product functions.

A Micromeritics ASAP 2020 accelerated surface area and porosimetry analyzer was used to determine the BET specific surface area.

2.4 Electrochemical Characterizations

Three-electrode electrochemical experiments were carried out in a custom-built three-electrode electrochemical cells with a Luggin capillary and a water jacket (Adams & Chittenden Scientific Glass). Cyclic voltammograms (CVs) and polarization curves for the oxygen reduction reaction were recorded at 25°C (thermostated by an Isotemp 3016D, Fisher) using an Ecochemie Autolab PGSTAT302N potentiostat. A Pt flag and a saturated calomel electrode (CH Instruments) were used as counter and reference electrodes, respectively. The electrolytes used in the electrochemical tests included 0.1 M perchloric acid (70%, Acros Organics) and 0.1 M potassium hydroxide solution made from KOH pellets ($\geq$85.0% Certified ACS, Fisher Chemical). In both electrolytes 18MΩ Millipore water was used. The electrolytes were always deaerated before electrochemical testing by bubbling with UHP grade nitrogen (Airgas) for 45 minutes. When required, after first bubbling with N_2, the electrolytes were saturated with O_2 by bubbling with USP grade oxygen (Airgas) for 45 minutes. Before every electrochemical test, each as-prepared electrode was subjected to break in cycles – typically 40 voltage cycles between 0 and 1.4 V in N_2-saturated electrolyte at 200 mV/s unless otherwise noted.

CHAPTER 3 – INVESTIGATION OF THE MODIFICATION PROCESS FOR TUNGSTEN CARBIDE AS SUPPORT CANDIDATE FOR PLATINUM

3.1 Objective

Tungsten carbide has become popular a candidate catalyst and support for the ORR in recent years because it has been discovered that close to the d-band center, the WC surface electronic structure is very similar to platinum and other platinum group metals, which suggests that its catalytic properties may be similar [158–165]. WC was first discussed as a potential ORR catalyst by Levy and Boudart in the 1970s [166]. They found that WC does have inferior electrocatalytic properties for ORR than Pt, probably because the ORR is a very structure sensitive reaction, only occurring at high rates on certain well known Pt crystallographic facets; however, its high electrical conductivity, relatively low price and insensitivity to poisons make it an interesting alternative to carbon support materials, which are thermodynamically unstable at higher potentials [167–169].

Recent work investigating WC-supported Pt electrocatalysts have shown higher activity than Pt/C in an operating PEMFC [170]. One possible enhancement mechanism proposed that the interaction between support and metal improve the electron transfer, which caused a rearrangement of the Pt d-band, similar to alloying effects. However, one thermodynamic limitation of WC in Liu et al.'s [171] recent studies is the formation of pure surface WC, where near-surface W and C atoms segregate to the surface and are subsequently oxidized when exposed to air or aqueous media. The surface WO_x species can further react in aqueous environments to form tungsten bronzes, which are water-

soluble. This property can actually facilitate catalyst instability, even Pt detachment, leading to poor cycle life. Therefore, the purpose of this work was to create modified WC to change the lattice unit and electronic property to avoid the surface oxidation and dissolution of pure WC. Ti was selected as the dopant since its bulk carbides have been shown to be more stable in oxidizing environments than WC [172] and can be inserted into the WC matrix with minimal structural strain and changes in bond coordination. Also, Group IV and V carbides are generally more stable than group VI carbides due to higher oxidation temperatures in oxygen and aqueous atmosphere, with the exception of ZrC, which is pyrophoric. As a result, it was thought that Ti insertion would shift the free energy for W and C lattice dissociation and surface segregation positive due to enhanced cation-cation interactions and a slightly smaller lattice sizes – leading to higher electrochemical stability than pure WC.

3.2 Results and Discussion

3.2.1 Physical Characterizations of Titanium-doped Tungsten Oxide

As discussed in Chapter 2, the first step in creating the mixed $Ti_xW_{1-x}C$ was to synthesize titanium doped tungsten oxide (Ti/WO_3). The powder XRD pattern for the synthesized Ti/WO_3 is shown in **Figure 3.1** (blue line), compared with that of pure tetragonal tungsten oxide, in red dots. All of the major peaks for Ti/WO_3 observed between the 20° and 90° diffraction angle (2θ) corresponded well with the major facets of pure WO_3, such as (001), (110), (200), (300), (102), (202), (400) of pure tetragonal tungsten oxide (JCPDS 85-0808). No secondary phases for titanium were observed, suggesting that Ti was well incorporated into the material and that tungsten and titanium did not mix as segregated solid oxides.
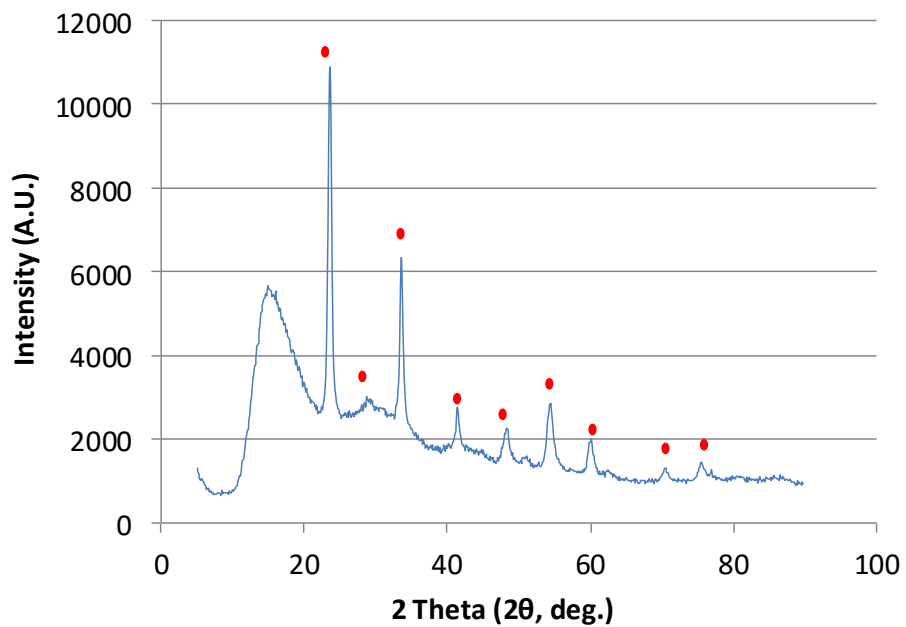
Figure 3.1 XRD pattern of titanium doped tungsten oxide (blue line) compared with pure tetragonal tungsten oxide (red dots)

The bulk morphology and elemental distribution were explored by SEM and EDS as shown in **Figure 3.2**. The average particle size of the support was fairly large, around of 30 to 50 micrometers in diameter due to severe aggregation during the heat treatment steps. The EDS elemental mapping in **Figs. 3.2a and 3.2b** suggested a homogeneous distribution of tungsten and titanium in both the bulk as well as the grain boundaries, which were probed with a cross-section of a cracked single particle. A higher resolution elemental analysis was done in order to show that Ti and W were homogeniously distribution throughout the support. A series of cross-sections were made with a focused ion beam (FIB), and then imaged using a Strata 400 STEM DualBeam equipped FE-SEM. The FIB can be used to prepare a precisely cut sample in-situ for high-resolution spectroscopy. This is especially helpful to investigate small sections of thick and/or delicate samples. In this case, two large agglomerates were cut by the ion beam to create flat cross-section areas for further analysis as shown in **Figs. 3.3a and 3.3b**. Many layers were removed from the sample and the elemental composition was completely independent of depth, showing that Ti was very well incorporated into the carbide supports, and the Ti and W were homogeneously distributed. To probe the composition further, a near 2-D sample was prepared, and the process to attain this sample is shown in **Fig. 3.3c**. A solid, representative particle was selected and a thin, continuous platinum metal film was deposited on the support in order to form a rigid surface on the top of the particle, which prevents cracking and collapse of the layer during FIB cutting. After achieving a card-like sample by removing material from both sides, the thick piece was placed on a triangle holder for further etching. More careful, and time consuming, FIB treatments were needed to obtain the final transparent 2-D layer. The 2-D sample was

then transferred to collect TEM and HRTEM images and elemental quantification spectra from random regions inside the red oval in **Fig. 3.3d**. The TEM images show one kind of particle structure and the HRTEM images in different regions showed only one lattice spacing and the element quantification spectra also showed the same W: Ti same atomic ratio throughout the observed area, which was essentially identical to the SEM EDS results.

3.2.2 Physical Characterizations of Titanium-doped Tungsten Carbide

Though the metal oxide was homogeneously doped with Ti, when it was heated up to 1200 °C (with a ramping rate of 3 °C/min) under oxygen-free atmosphere in a tube furnace, which is a normal procedure for producing metal carbides, the situation was different from mixed metal oxides. From the XRD pattern for the mixed metal carbide (blue line) shown in **Fig. 3.4**, totally separated phases of tungsten carbide (red dots), titanium carbide (blue dots) and even metallic tungsten (green dots) were observed at the same time, indicating the existence of a solid mixture of different metal carbides. A similar trend was obtained from the EDS elemental quantification spectra on random regions with different contrasts of the TEM image, **Fig. 3.5**. Significantly varied values of the atomic ratio of W: Ti suggested the irregular dispersion of Ti in the mixed carbide material.

In order to investigate the oxide-carbide conversion process during the heating step at different high temperatures, in-situ XRD was performed on titanium doped tungsten oxide from 600 °C to 1150 °C, heating for 30 mins for every intermediate 50 °C with the ramping rate of 3 °C/min and collecting the XRD patterns for each individual temperature (**Fig. 3.6**). Until 850 °C, all of the peaks in the XRD pattern corresponded to
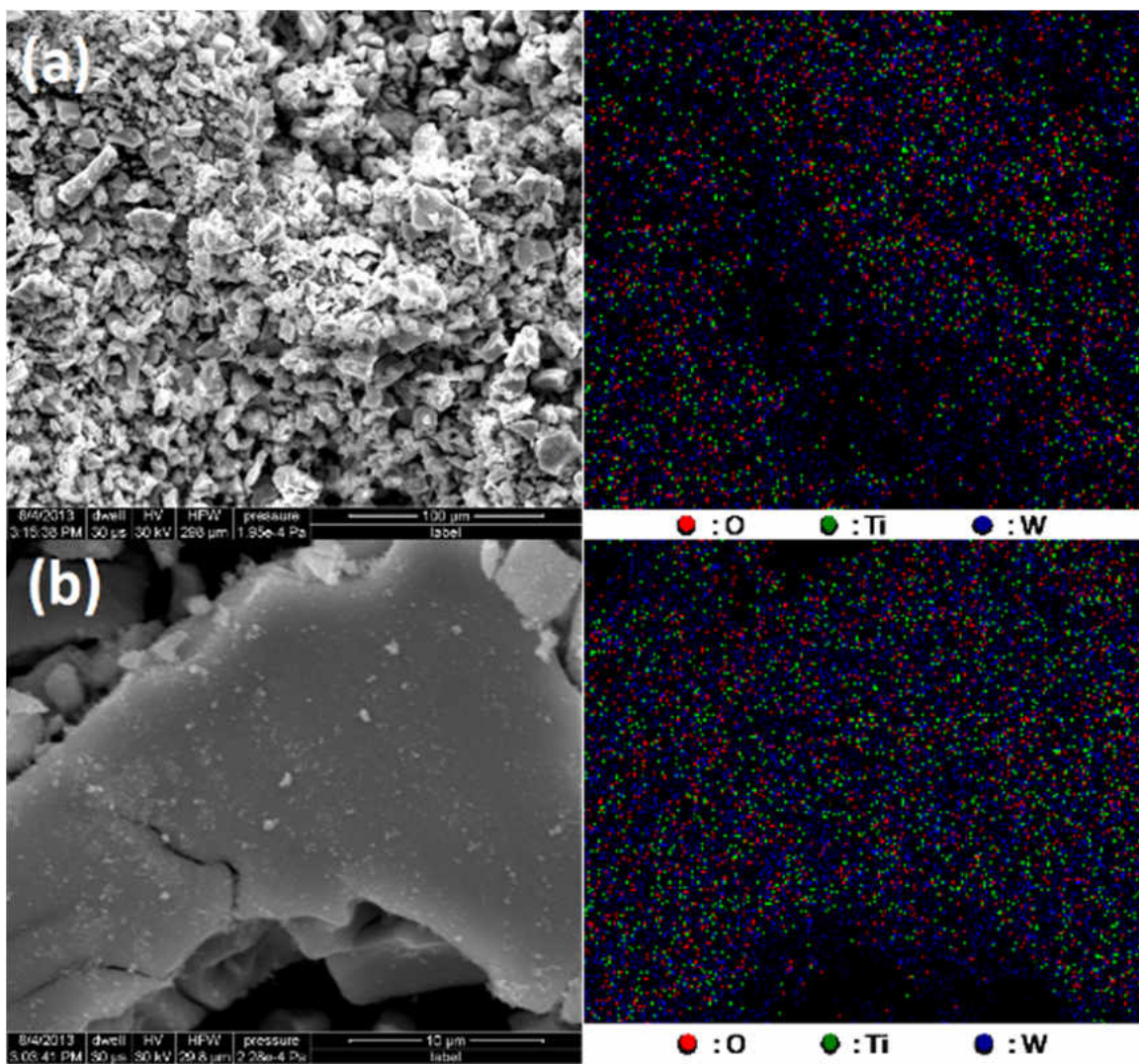
Figure 3.2 SEM images and EDS elemental mapping of Ti/WO$_3$ in (a) large region of the

catalyst sample; (b) cross-section of a single particle.
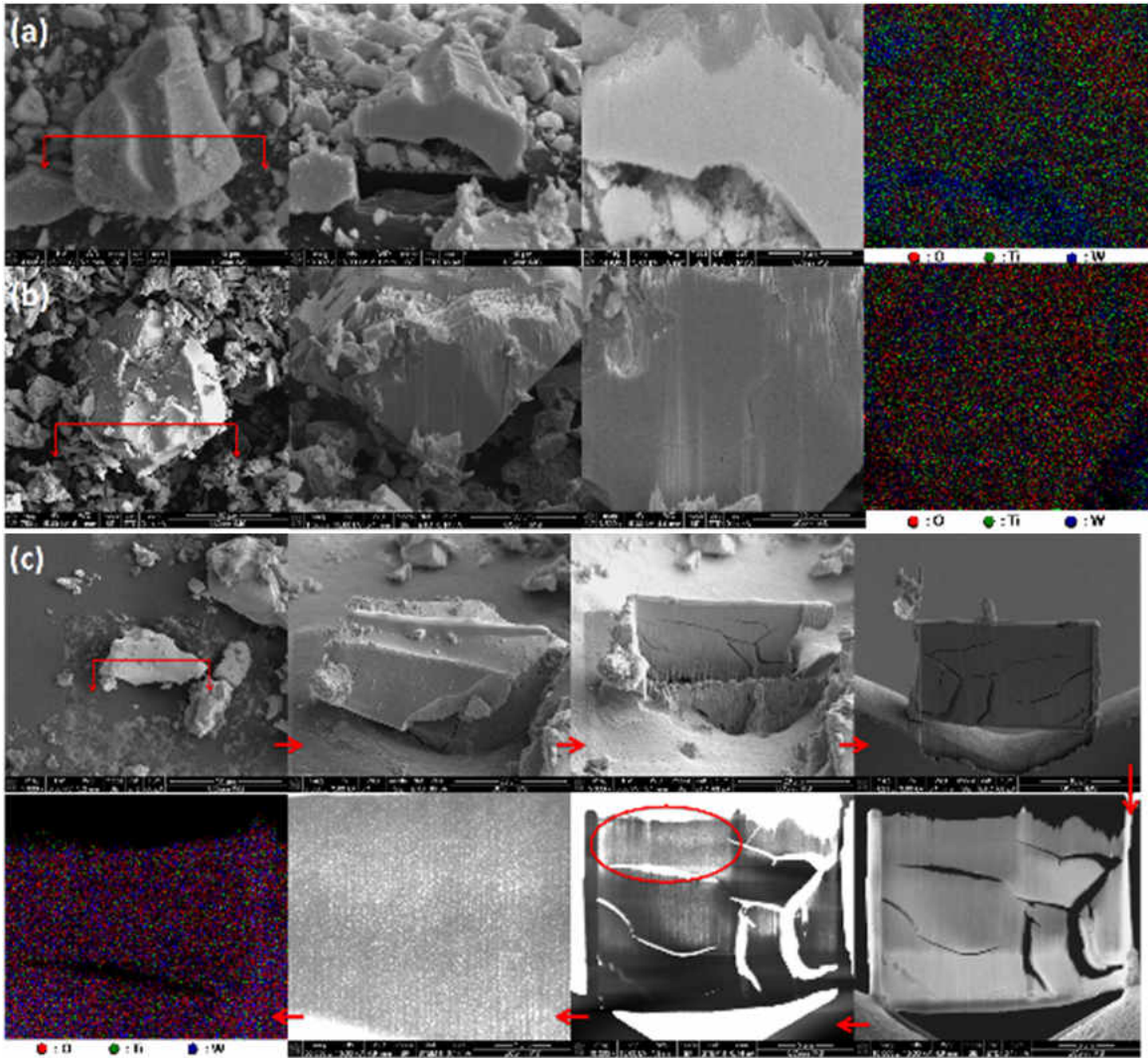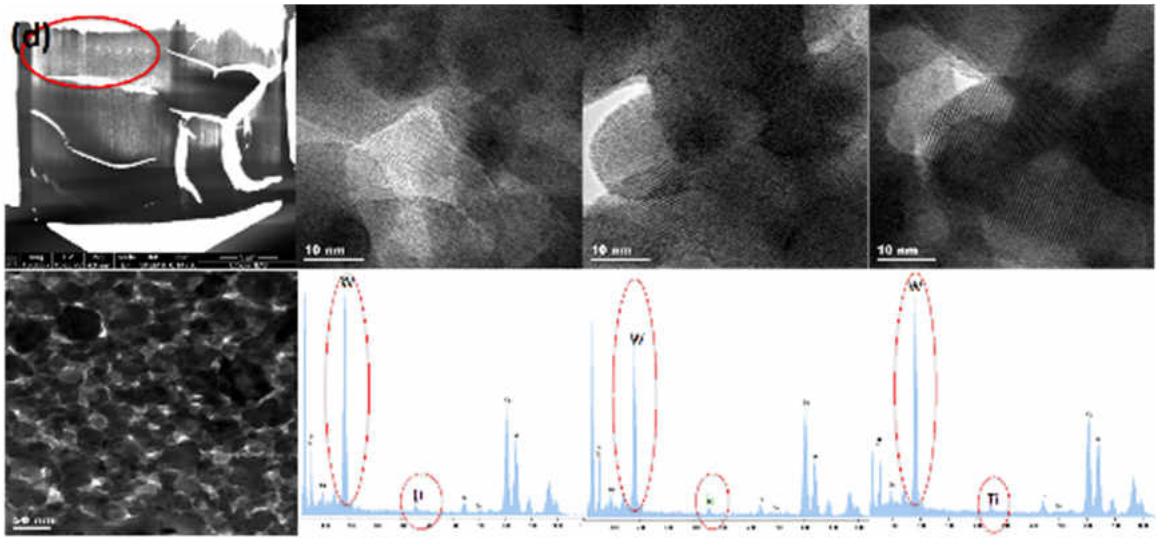
Figure 3.3 FIB cutting processes for high-resolution spectroscopy and EDS elemental mapping for (a) (b) cross-sections; (c) thin layer in the middle of a large particle; (d) TEM and HRTEM images and elemental mapping in random small regions on the thin layer.

the phases of tetragonal tungsten oxide as indicated by the red dots. With an increase in the temperature, the increased crystallinity became obvious. However, from 900 °C to 1000 °C, Ti started to phase separate from the tungsten oxide, and the anatase phase of titanium dioxide started to appear in the pattern, shown by the yellow dots. At higher temperatures, the anatase phase was completely converted to the rutile phase. Therefore, at lower temperatures, the titanium can be incorporated into the lattice of tungsten oxide to from a single phase solid oxide according to previous characterizations, due to the same tetragonal lattice unit and similar sizes of titanium oxide and tungsten oxide (**Fig. 3.6**). But with the increase of temperature, titanium started to diffuse out to form titanium oxide phase in order to stay at a lower thermodynamic surface energy, which is also one of the reasons of the failure of doped metal carbide formation. Another reason is that the difference of the lattice structure of tungsten carbide and titanium carbide, for being hexagonal and cubic, respectively (**Fig. 3.4**).

3.2.3 Electrochemical Charaterization of (Ti)/WO₃ and Pt/(Ti)/-WO₃

Though the mixed metal carbide was never truly formed, the obtained intermediates. WO_3 and Ti/WO_3, can be adopted as electrocatalyst candidates for methanol oxidation reactions (MOR) due to: i) the oxophilic nature of WO_3 to minimize of CO poisoning by transition metal oxides; ii) the electronic and ionic conductivity of hydrogen tungsten bronze (H_xWO_3) formed from WO_3 in acid solution; iii) the facilitated dehydrogenation ability during the MOR by H_xWO_3 [173,174].

The electrochemical properties of WO_3 and Ti/WO_3 and their Pt supporting analogues were studied in a three-electrode cell on a rotating disk electrode (RDE). WO_3 and Ti/WO_3 with different Ti loadings were dispersed on the glassy carbon electrode as
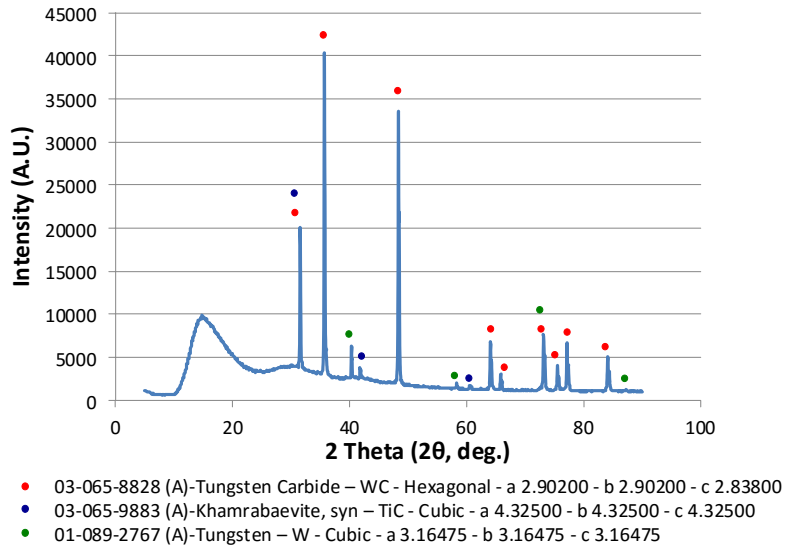
Figure 3.4 XRD pattern of titanium doped tungsten carbide (blue line) compared with pure tungsten carbide (red dots), titanium carbide (blue dots) and metallic tungsten (green dots).
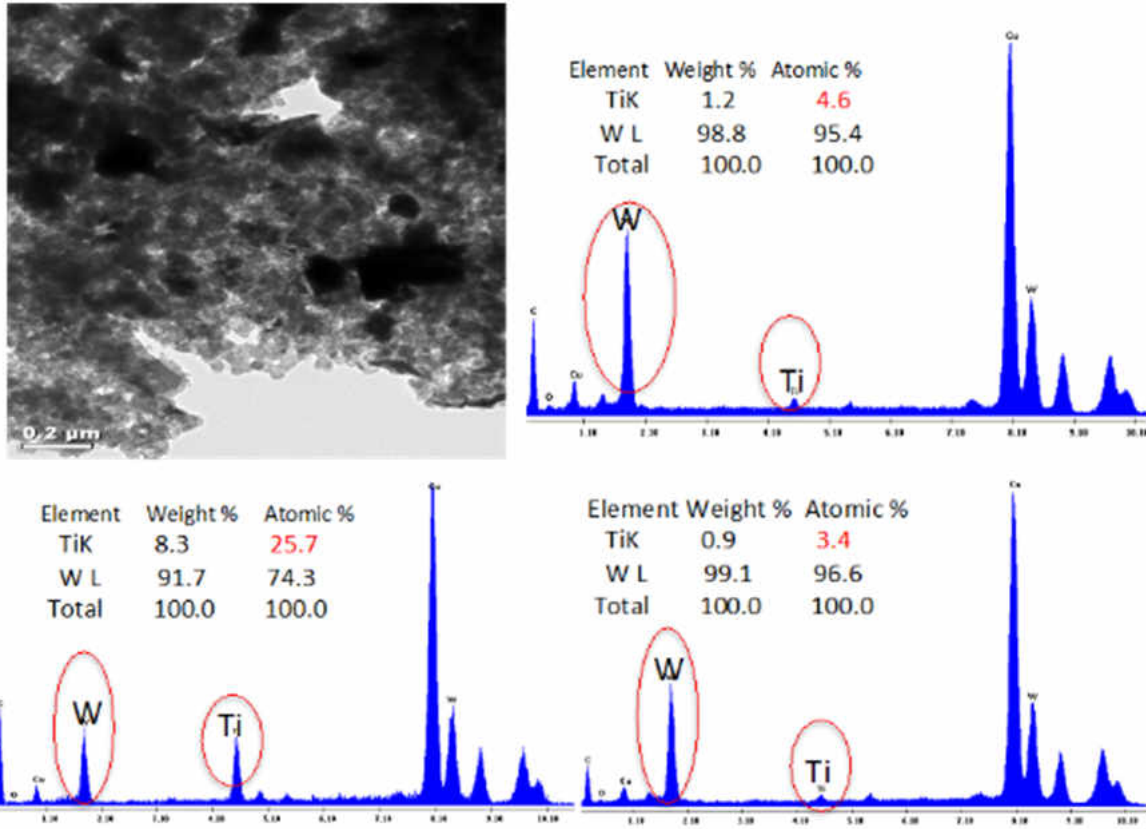
Figure 3.5 TEM image and elemental quantification spectra and charts of titanium doped tungsten carbide in random small regions.

Figure 3.6 In-situ XRD pattern of Ti/WO$_3$ from 600 °C to 1150 °C.
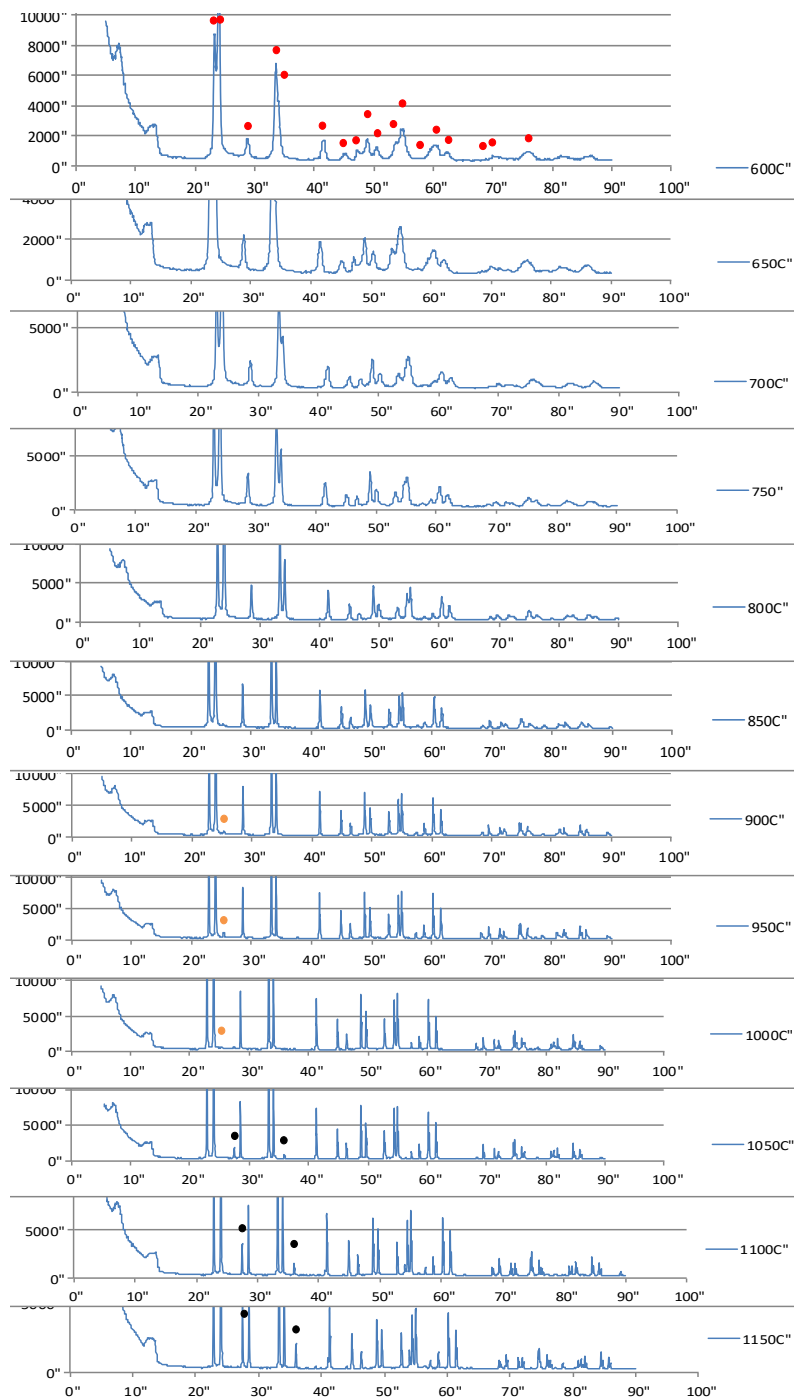
- ● 01-085-0808 (A) - Tungsten Oxide - WO$_3$ - Tetragonal - a 5.25000 - b 5.25000 - c 3.91500
- ● 01-070-6826 (A) - Anatase, syn - TiO$_2$ - Tetragonal - a 3.77100 - b 3.77100 - c 9.43000
- ● 01-076-0317 (A) - Rutile, syn - TiO$_2$ - Tetragonal - a 4.59240 - b 4.59240 - c 2.95750

support materials. Pt was electrochemically depostited onto the support by galvanic displacement of Cu, as detailed in **Chapter 2**. The Cyclic voltammograms (CVs) of Pt supported on WO_3 and Ti/WO_3 with 8 at% and 16 at% Ti loading in pure 0.1 M $HClO_4$ were collected and are shown in **Fig. 3.7a**. The different ESCAs of the supported Pt indicated by the hydrogen adsorption/desorption region from 0.05 to 0.3 V might suggest that the doping and different doping amount of Ti have an influence on the exposed facets of Pt and further result in the adsorption ability difference for the surface species. The MOR activities for the three samples increased in the order $Pt/Ti/WO_3$ (8 at%)< Pt/WO_3 < $Pt/Ti/WO_3$ (16 at%), which can be indicated by the peak current density in the anodic scan in the MOR polarization curves (**Fig. 3.7b**). The reason for the initially decrease then increase of the MOR activity maybe explained by the partial suppression of the transformation of WO_3 to H_xWO_3 at lower doping level, and the metallic Ti diffusing to the mixed metal oxide surface to improve the electronic conductivity [175]. For the stability enhancement for doped WO_3 support, the chronoamperometric responses for Pt/WO_3 and $Pt/Ti/WO_3$ (8%) in **Fig. 3.7c** exhibited a current density decrease (at 0.85 V vs. RHE) of 3 and 1 mA/cm^2 after 1 hour, respectively. The improved durability was likely caused by the prevention of tungsten dissolution because of the Ti^{4+} incorporation at a lower doping level into the lattice of WO_3 [176]. Therefore, in order to make full use of the advantages of WO_3 as a support for Pt during the MOR, titanium was incorporated into WO_3 which both stabilized the structure, and improved the activity. Modification influences were observed with two doping percentages, although different effects on activity and stability were demonstrated due to different doping density and surface states. Future studies are recommended in **Chapter 8** for understanding the doping density

59

influence in WO_3 on electrochemical performance in MOR in order to achieve an activity-stability balance or compromise for MOR catalysts, and to provide a new method for elemental doping in electrocatalysis.

3.3 Summary

A sol-gel synthesis procedure for titanium doped tungsten oxide and carbide was explored and the intermediates and final products were extensively characterized. Results showed that 8 at% of titanium was fully doped into the lattice of tungsten oxide, existing as a single phase and uniform structure. However, when the annealing temperature surpassed 900 °C, titanium oxide (anatase and rutile phases) started to segregate as a second phase from in-situ XRD results. At the temperature for the formation of carbide in argon atmosphere, tungsten carbide and titanium carbide were completely separated with small amount of metallic tungsten. The failure of forming titanium-doped tungsten carbide was attributed segregation of the titanium and tungsten oxides at high temperatures and the difference of lattice structures and sizes of the two carbides. However, this work does provide principles, design theory and possible analytical techniques for producing doped metal oxides and carbide. And the intermediate product---titanium doped tungsten oxide can serve as a potential electrocatalyst support for Pt in MOR systems [163–165], with enhanced activity and durability at two different doping percentages: higher activity at 16 at% and better durability at 8 at%. The techniques for the doping density influence mechanism on electrochemical performance in MOR is recommended for future work in **Chapter 8**.
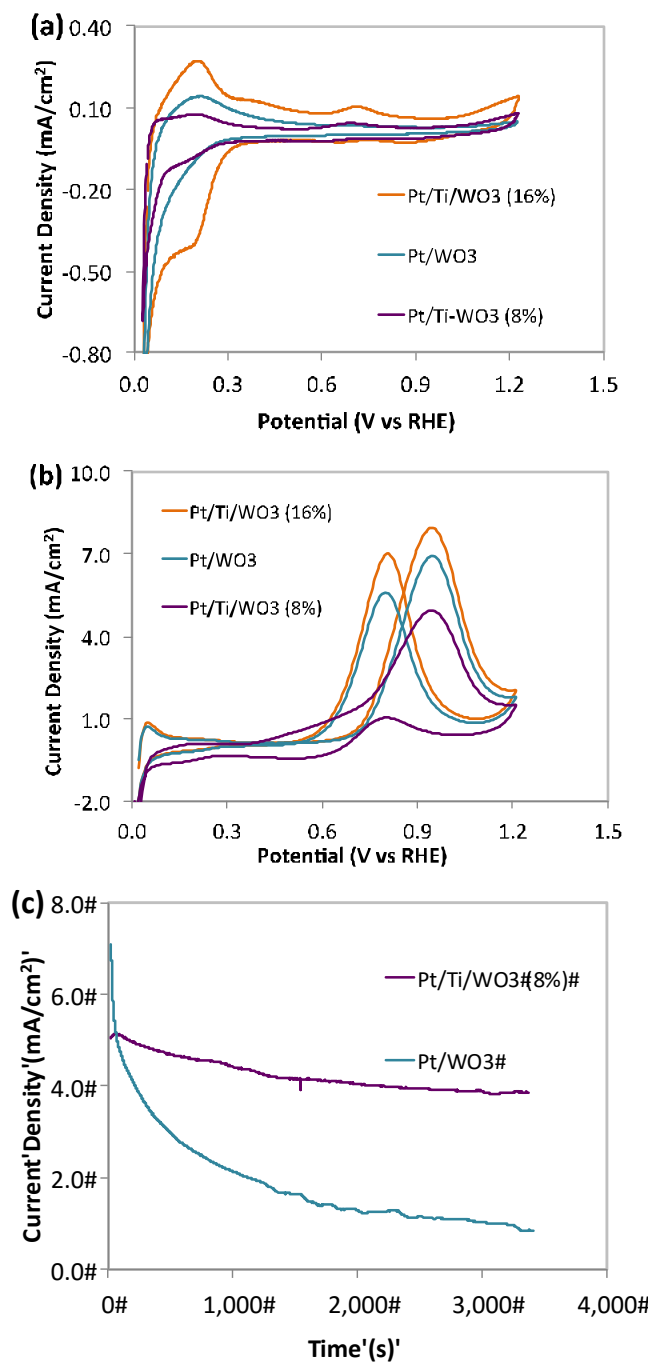
Figure 3.7 (a) Cyclic voltammetries (CVs) in 0.1 M HClO₄; (b) methanol oxidation

polarization curves in 0.1 M HClO₄ with 0.1 M of methanol of Pt/WO₃, Pt/Ti/WO₃ (8%)

and Pt/Ti/WO₃ (16%); (c) Chronoamperometry of Pt/WO₃ and Pt/Ti/WO₃ (8%) in 0.1 M

HClO₄ with 0.1 M of methanol, at 0.85 V vs. RHE.

CHAPTER 4 – DURABILITY STUDY OF TUNGSTEN DOPED TITANIUM OXIDE SUPPORTED IRIDIUM/IRIDIUM OXIDE IN A PEM ELECTROLYZER

4.1 Objective

Proton-exchange membrane (PEM) electrolyzers have been well industrialized for pure hydrogen and oxygen production for mobile applications and energy storage when combined with renewable energy sources such wind and solar. Iridium/iridium oxide is the most widely adopted catalyst for the oxygen evolution reaction (OER) at the anode side of PEM electrolyzer due to its proven combination of activity and durability. A significant effort has been made to support iridium on chemically stable metal oxides such as tintania, or alloying Ir with nickel and copper or noble metals (e.g. Pt and Ru) to either decrease the loading and cost of the catalyst or to manipulate the dispersion of Ir to improve the catalyst efficiency and durability. IrO_2 and Ir nanoparticles supported on a high surface area support material can be an effective approach to reduce the amount of noble metal in the cell. This strategy not only can stabilize the initial catalyst surface area but also significantly improve the mass activity of the catalysts. PEMECs cannot employ carbon supports at the oxygen electrode because of the significant driving force for carbon oxidation to CO_2. Therefore, non-carbon supports are a necessity at the electrolyzer anode, and various conductive metal oxides including modified TiO_2, Nb_2O_5, and antimony doped tin oxide (ATO) have been investigated as support candidates.

In this Chapter, iridium was supported on tungsten doped titanium oxide (W-TiO_2) due to its excellent durability and inertness in strongly oxidizing environments through ethylene glycol reduction. The OER activity and stability of the supported iridium were

compared with commercially available iridium black in both ex-situ RDE and in-situ electrolyzer experiments. The relationship between catalyst durability and synthesis parameters and iridium loadings were systematically investigated to provide supported catalyst design principles to lower the iridium loading in practical systems.

4.2 Results and Discussion

4.2.1 Physical Characterizations of the Initial Batch

In order to investigate the bulk elemental composition, EDS was performed on different regions of the powdered samples after synthesis. The elemental spectra and resulting composition are shown in **Fig. 4.1**. The average weight percent of elemental iridium in the whole catalyst sample was ~29%. From the TEM image shown on the right, it was straightforward to confirm that these Ir/IrO_2 particles, with an averageg size of 1-2 nm in diameter, were homogeneously distributed on the commercial W-TiO_2 support, which had a diameter of 30-50 nm.

4.2.2 Morphology Change by Controlling the Synthesis Parameters

In order to study the relationship between the physical properties and the durability of the catalyst material in a PEM electrolyzer, the synthesis procedure was systematically modified by changing various parameters. According to the literature, in this template-free polyol reduction reaction, the glycolate anion formed in the presence of NaOH acts as a good stabilizer for Ir colloids, possibly forming chelate-type complexes via its carboxyl groups that further prevent the agglomeration of the supported Ir particles[177]. On the contrary, lowering the pH may cause more agglomerates and

further enlarge the Ir particles, as shown in the TEM image of batch 2 in **Fig. 4.2b**. The particle size increased to about 3-4 nm and the clusters appeared to be increasingly connected. Lowering the reaction temperature can also increase the particle size by controlling the particle growth and particle nucleation. The TEM image in **Fig. 4.2c** shows the Ir dispersion of batch 3 with a lower heating temperature 120 °C. The average particle size increased to around 5-6 nm. Increasing the metal precursor concentration can result in higher coverage of catalyst on the support, as shown by the TEM images in **Figs. 4.2c** and **4.2d**. The iridium coverage was more concentrated indicated by darker color, and the iridium weight percent increased to 70% and 80 % in Batches 3 and 4, respectively.

On the other hand, the annealing process may also influence the final morphology of the materials. **Figure 4.3** shows two different annealing procedures instead of drying in a vacuum oven at 110°C for 4 hours for previous batches. Keeping all of the other synthesis parameters the same as in Batch 1, the last drying step was changed to heating in air and argon in a muffle furnace for one hour at 400 °C, with a heating rate of 10 °C/min. The structures are shown in **Fig. 4.3**. After annealing in air, the iridium particles extended into sheet-like structures on the W-TiO$_2$ support in **Fig. 4.3a** and agglomerated into larger particles around 5-6 nm in argon atmosphere in **Fig. 4.3b**.

Element Number	Element Symbol	Element Name	Weight Concentration
22	Ti	Titanium	55.6
6	C	Carbon	15.8
77	Ir	Iridium	28.6
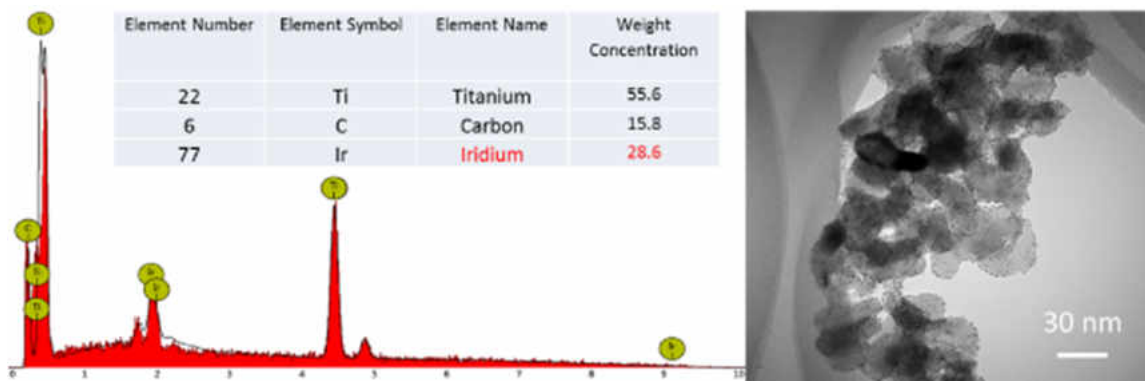
Figure 4.1 Physical characterizations of the initial batch: EDS result on the left and TEM image on the right.
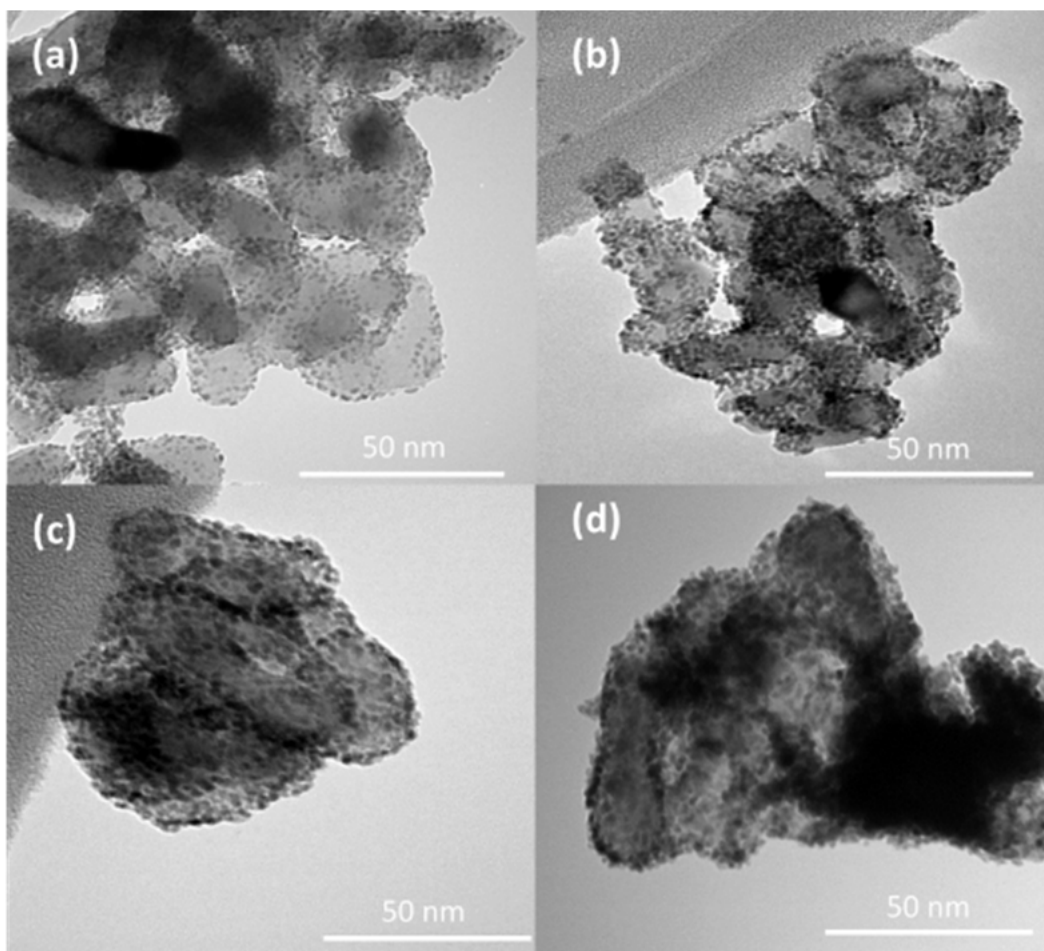
Figure 4.2 Different morphologies of the supported structure by different synthesis procedures: (a) Batch 1; (b) Batch 2; (c) Batch 3; (d) Batch 4.
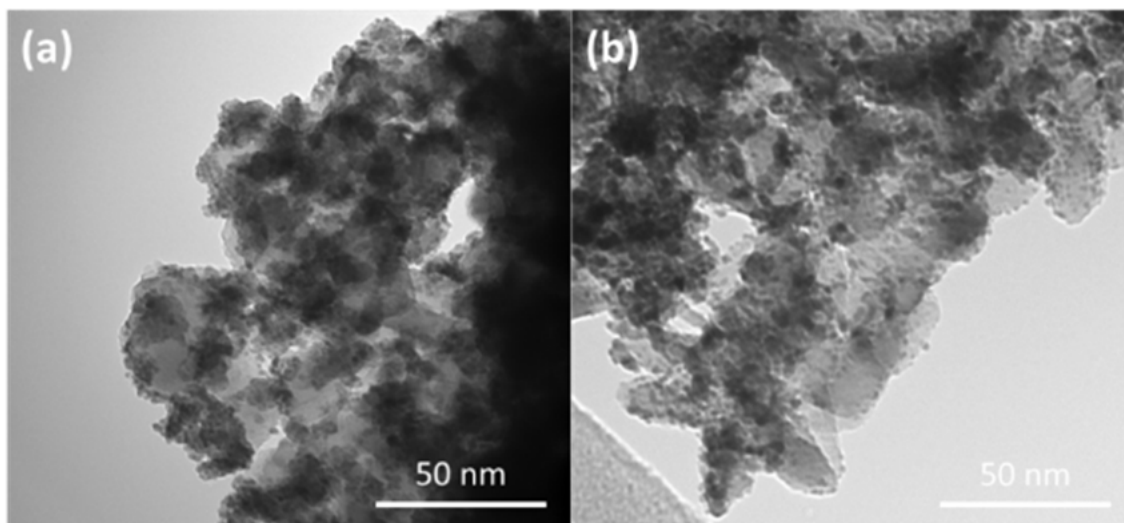
Figure 4.3 Different morphologies of the supported structure by different annealing procedures: (a) Batch 1 annealed in air at 400 ℃ for 1 h; (b) Batch 1 annealed in argon at 400 ℃ for 1 h.

4.2.3 Durability Analysis

The oxygen evolution reaction activity and durability for Batch 1 both ex-situ and in-situ are shown in **Figure 4.4**. The polarization curve showing the mass activity was collected from 1.3 to 2.0 V, at 20 mV/s in 0.1 M perchloric acid with an electrode rotation rate of 900 rpm. The OER activity of Batch 1 was higher than commercial Ir black (**Fig. 4.4a**). A durability test was performed, exposing the catalyst to 1000 cycles between 1.3 and 2.0 V at 200 mV/s, and no obvious degradation was observed (**Fig. 4.4b**), a very good result. However, in the in-situ electrolyzer test, the OER activity was only comparable to standard Ir black (**Fig. 4.4c**), and low loading achieved the best performance (**Fig. 4.4d**). From the durability test in an operating electrolyzer, a significant HFR increase of 1 mohm was observed in the first hour, as well as a profound morphology change after hot pressing (**Fig. 4.4e**) and after durability testing (**Fig. 4.4f**) were observed. Large agglomerates rendered much more exposed, uncovered supported material, which caused the higher resistance and the poor durability.

Batch 2 showed similar phenomena without much improvement. But Batch 3 exhibited much better durability for over 20 hours, **(Fig. 4.5)** with much higher coverage of iridium on the support surface, leaving less exposed support area. However, a 1 mohm increase in the high frequency resistance (HFR) over a 25-cm^2 active area of the cell after 24 h still degraded the cell performance appreciably, which may be caused by the Ir active area loss.

With an even higher Ir coverage in Batch 4, the electrolyzer durability test with low loadings (0.6 mg/cm^2) **(Figs. 4.6a and b)**, showed a similar trend in the first 24 hours as in Batch 3, but stabilized after that, up to 150 hours. However, with high loadings (1.5

mg/cm^2) (**Figs. 4.6c and d**), Batch 4 had much smaller initial HFR, and the HFR increase in the first 24 hours was greatly decreased, and then stabilized after 24 hours. Good activity and durability was achieved with higher catalyst loading. Agglomeration of Ir still occurred over the 100-hour durability test, but the support material was still mostly covered with Ir, **(Figs. 4.6e and f)** and only a very small portion of regions with less Ir resulted in isolated regions of Ir and support **(Fig. 4.6g)**. Therefore, with a higher loading (70%) of Ir on the W/TiO$_2$ support material, and a higher coverage of catalyst on the support, the durability was much improved. In addition, the catalysts showed similar acitivity as standard commercial Ir black.

4.3 Summary

In this study, it was shown that the Ir supported on tungsten doped titanium oxide with a loading lower than 30 wt% material by polyol reduction method resulted in poor durability in an operating electrolyzer due to the agglomeration of the iridium particles and an increase in the exposed area of the support materials regardless of the particle size. However, with higher iridium loading of Ir (70 wt%), the durability was much improved with very limited HFR increase, due to a slight initial morphology change in the first 24 hours, and then stabilized after that, because less support material was exposed. Therefore, with the comparable initial OER activity to standard commercial Ir black, and good durability at current density of 1.5 A/cm^2 in an operating electrolyzer, the electrochemical performance of the homemade Ir/W-TiO$_2$ catalyst is likely to get industrial implementation. However, further improvement on the Ir utilization can likely be achieved by balancing the Ir loading and durability, which is recommended for future work.
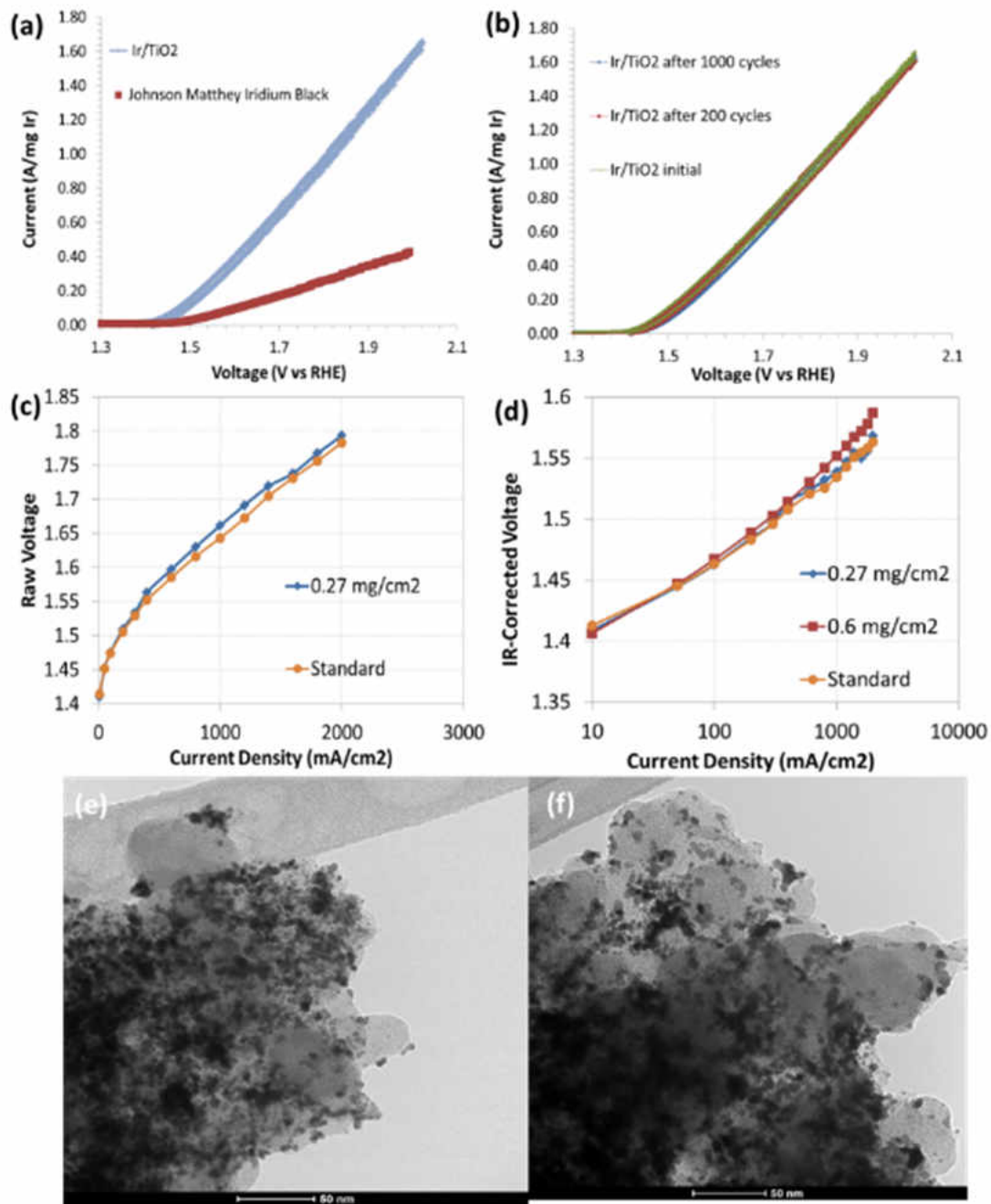
Figure 4.4 (a) OER activity of Batch 1 at RDE level, compared with commercial Ir black; (b) OER durability of Batch 1 at RDE level, for 1000 cycles; (c) (d) OER polarization curve of Batch 1 at PEM electrolyzer level, raw data and IR-corrected, respectively, compared with standard commercial Ir black; (e) Morphology change after hot pressing process; (f) Morphology change after 1000 cycles of durability test.
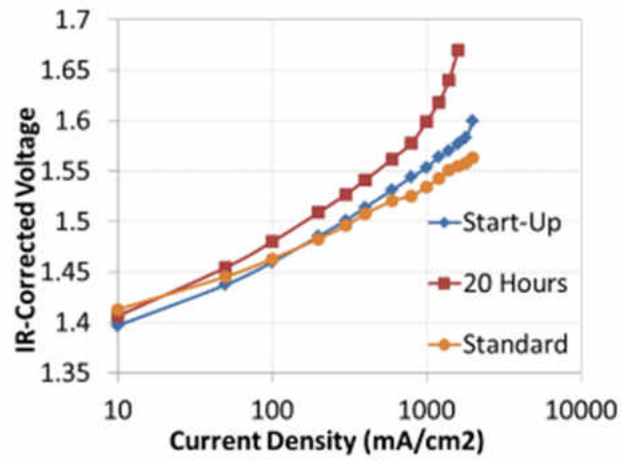
Figure 4.5 OER polarization curve and durability of Batch 3 at PEM electrolyzer level,

IR-corrected data, compared with standard commercial Ir black.
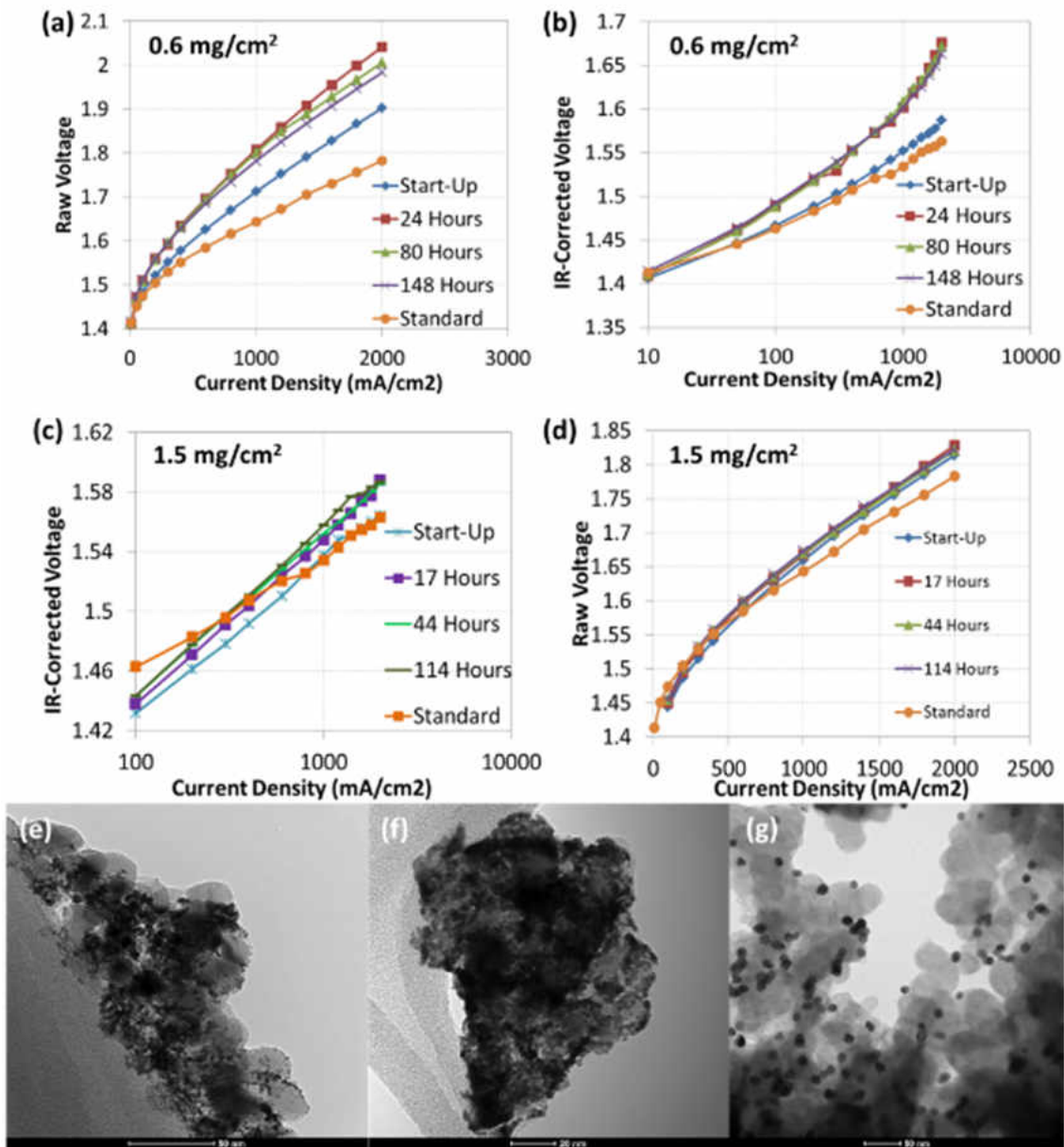
Figure 4.6 (a) (b) OER polarization curve of Batch 4 at PEM electrolyzer level with low loading: 0.6 mg/cm², raw data and IR-corrected, respectively, compared with standard commercial Ir black; (c) (d) OER polarization curve of Batch 4 at PEM electrolyzer level with high loading: 1.5 mg/cm², IR-corrected and raw data, respectively, compared with standard commercial Ir black; (e) (f) (g) Morphology change after more than 100 hours of durability test.

CHAPTER 5 – CALCULATING THE ELECTROCHEMICALLY ACTIVE SURFACE AREA OF IRIDIUM OXIDE IN OPERATING PROTON EXCHANGE MEMBRANE ELECTROLYZERS

5.1 Objective

One of the most common methods to calculate the electrochemically active surface area (ECSA) of a catalyst is to collect a cyclic voltammogram (CV) in N_2-saturated electrolyte and measure the hydrogen adsorption charge (Q_r) in the negative-going scan after correction for double-layer charging. This works for platinum because Pt has the ability to undergo hydrogen underpotential deposition (H_{upd}). However, iridium oxide does not have access to the same mechanism for underpotential deposition of H onto its surface, which makes it difficult to determine the ECSA. In 1990, Savinell et al. [156] found area-pseudocapacitive charge correlations for ruthenium dioxide and iridium dioxide electrodes on titanium substrates using a zinc ion adsorption method. Though their method was able to correlate mass loading with ECSA and pseudocapacitive charge, they were not able to explain why the kinetic rate constant for Fe^{2+}/Fe^{3+} redox couple on IrO_2 was one order of magnitude below the expected value using the estimated ECSA, suggesting that the result was systems-dependent, not a universal constant. Additionally, their electrolyte solution was HCl, which does not well mimic the perfluorosulfonic acid environment of commercial MEAs. Both limitations called into question whether this method could be extended to electrocatalyst operation in state-of-the-art commercial MEAs.

In this work, the Savinell method is improved upon by introducing a more accurate zinc concentration detection technique, UV-Vis spectrophotometry, and performing the experiments in sulfuric acid electrolytes. The method is applied to two distinct electrocatalyst systems (electrochemically deposited IrO_x thin film and IrO_x powder film systems), showing that the results are not microstructural or systems-dependent. The new method was extended to an operating PEM electrolyzer membrane electrode assembly (MEA) from Proton OnSite. For the first time it was possible to calculate a definitive ECSA constant for IrO_2, and determine the surface utilization of IrO_2 as well as the OER specific activity.

Before applying to IrO_2 in an operating electrolyzer MEA, the method was developed and validated on both well-defined electrodeposited surfaces and powder catalysts ex-situ. The overall experimental flowsheet to determine the ECSA of IrO_2 oxygen evolution reaction catalysts is shown in **Figure 5.1** [178,179].

Both electrodeposited IrO_x and IrO_x powder catalysts were prepared and physically characterized as discussed in **Chapter 2**. IrO_x mass loadings were determined. The electrodes were then introduced to a three-electrode electrochemical cell to collect CVs in order to calculate pseudocapacitive charge. The resulting electrodes were soaked into solutions containing zinc cations to allow zinc adsorption onto the IrO_x surfaces. The true ex-situ ECSA was calculated by multiplying the surface area occupied by each zinc cation by the total number of adsorbed zinc cations, which was determined by UV-Vis spectrophotometry. Details of each step are given in the following sections.
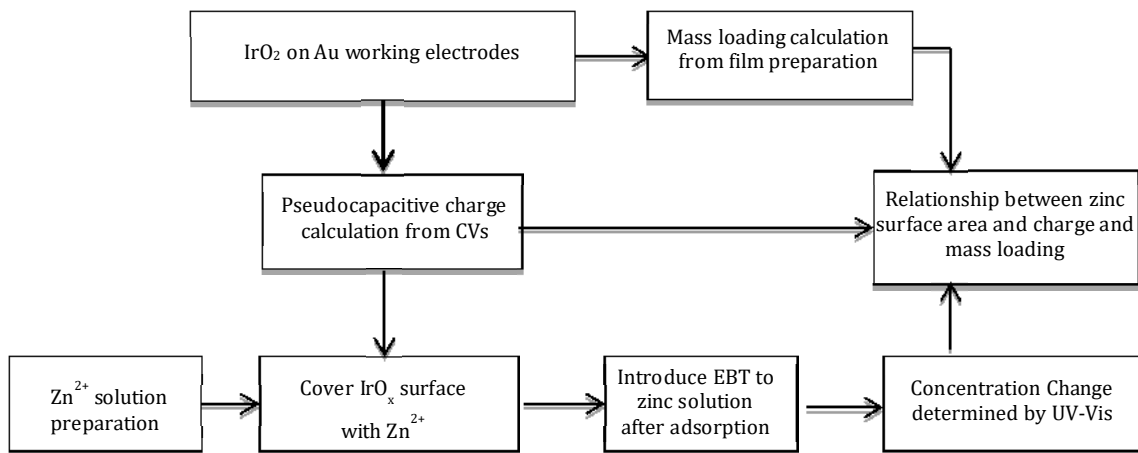
Figure 5.1 Method flowsheet to determine the ex-situ IrO$_2$ ECSA.

5.2 Results and Discussion

5.2.1 Electrodeposition of Ir and IrO₂ thin films onto polycrystalline gold electrodes

Sawy et al. studied the effect of potential on Ir electrodeposition on gold substrates in H_2IrCl_6 solution [180]. They observed the maximum deposition rate (measured by in-situ quartz crystal microbalance) was achieved from 0.1 V to 0.2 V because the rate-limiting step leverages H_{upd} as the reducing agent for $IrCl_6^{3-}$ to metallic Ir. They also found that the current efficiency of Ir electrodeposition is close to 100% at 0.2 V when the H_2IrCl_6 concentration in solution is ≤0.05 mM. The insight from these findings guided the Ir deposition bath in this work; the deposition potential was set at 0.2 V, and the H_2IrCl_6 solution concentration was 0.04 mM.

The chronoamperometric response of the working electrode during Ir deposition is shown in **Fig. 5.2a**. The successful deposition of Ir onto the gold electrode is evident by the increasing hydrogen evolution and oxidation current from CVs (**Fig. 5.2b**) collected intermediately during the deposition, because the gold is a very poor hydrogen evolution catalyst in acid media as shown in the CV in **Fig. 5.2c**. After cleaning the deposited Ir surface with copious DI water, the surface Ir was oxidized to iridium oxide in 0.5 M H_2SO_4 electrolyte by sweeping the potential up to 1.5 V. The oxidation of Ir was accompanied by appearance of two characteristic redox peaks at 0.9 V and 1.4 V as well as the decreasing current density of the hydrogen adsorption/desorption at low potentials with increased cycle number, which is shown in the CVs in **Fig. 5.2d**.

5.2.2 Physical Characterization of electrodeposited Ir and IrOₓ thin films

The as-electrodeposited metallic Ir surface was silver in color and had a near mirror finish. The morphology of this surface was observed under SEM, **Fig. 5.3a**. The

surface had a high density of irregular surface defects around a few hundred nanometers and many smaller-sized pores with a diameter of approximately 50 nm. The yellowish oxidized IrO_x surface in **Figs. 5.3b** and **5.3c** showed that there were pores approximately 100~300 nm in diameter caused by surface cracking and defects, and other deep pores around 50 nm in diameter. This semi-porous structure led to linearly increased surface area with increased IrO_x loading. The approximate elemental composition was found by EDS. **Fig. 5.3d** showed the surface of IrO_x with adsorbed zinc ions. From **Fig. 5.3e** (EDS map for **Fig. 5.3d**), it can be seen that iridium and oxygen were homogeneously distributed. Significant zinc could also be seen in the area, even after a thorough cleaning with DI water, showing that Zn was very strongly adsorbed on the surface.

The composition of the IrO_x surface was investigated by XPS. The high-resolution spectra for Ir 4f in **Fig. 5.4** were calibrated to the graphite C 1s peak at 284.6 eV. The Ir 4f spectra were deconvoluted into two doublets (four peaks). The binding energies of the first deconvoluted doublet peaks (green and purple lines, respectively) corresponded to that of the Ir^{4+} $4f_{5/2}$ and Ir^{4+} $4f_{7/2}$. The second doublet at lower binding energy (orange and blue lines, respectively) was consistent with metallic Ir $4f_{5/2}$ and Ir $4f_{7/2}$. Approximately 28 atom % of the near surface Ir in the thin film existed in the Ir^{4+} state with the balance being Ir. The penetration depth of the XPS X-ray probe is 8-10 nm, which is approximately 23 atomic layers. The electrolyte is only exposed to the outmost layer. Therefore, the oxidation of the bulk relies heavily on oxygen solid-state diffusion and it is most likely that the near surface Ir was nearly completely oxidized to IrO_2, but the bulk was not.
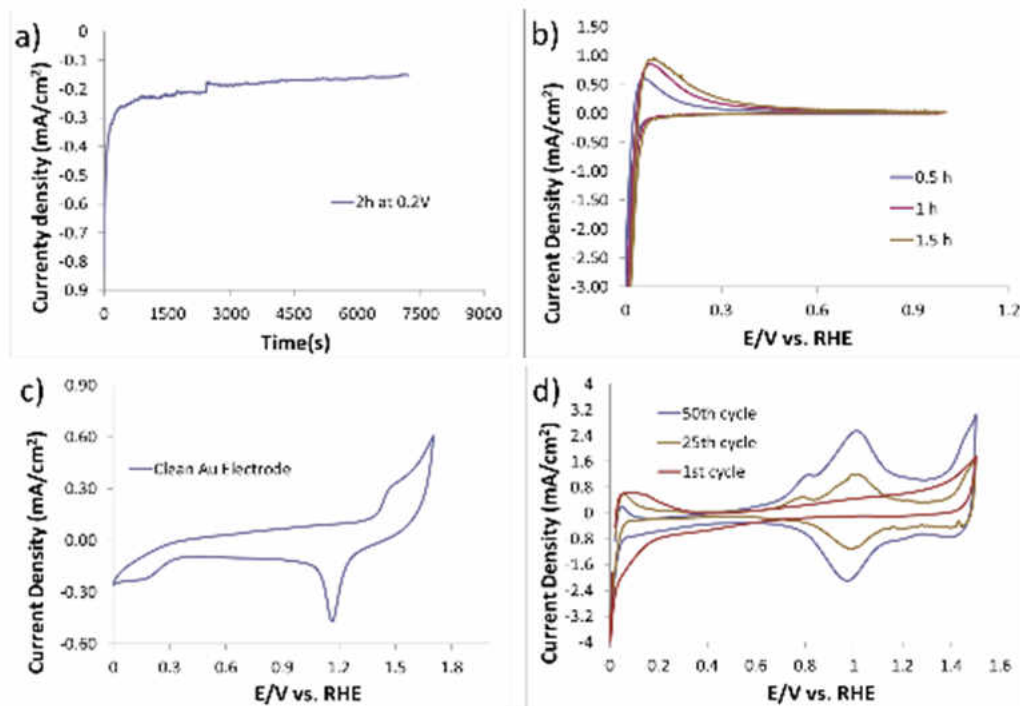
Figure 5.2 (a) Chronoamperometry of Ir deposition; (b) Cyclic voltammetry of Ir deposition; (c) Cyclic voltammetry of clean Au electrode; (d) Ir surface oxidation by cyclic voltammetry.
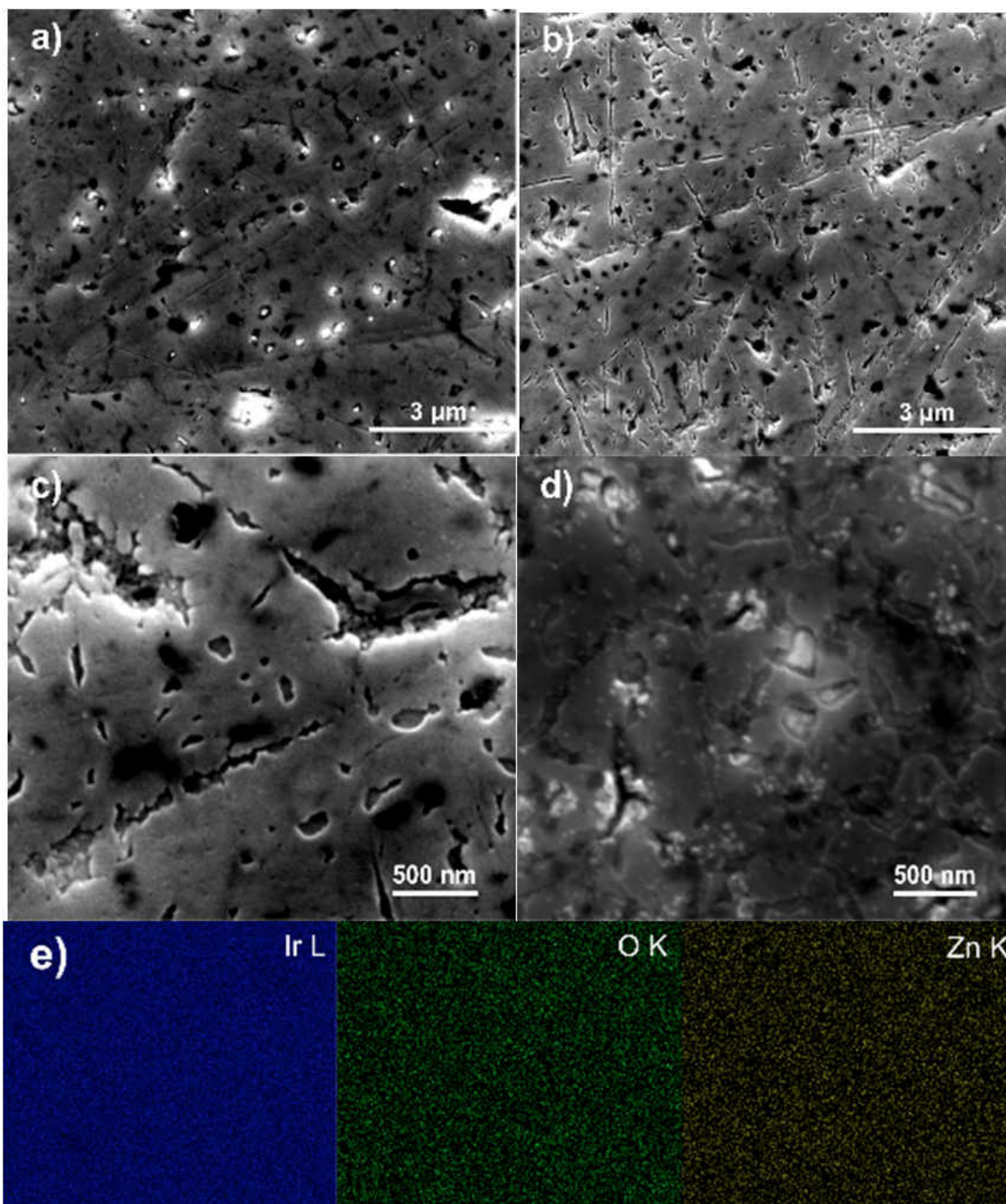
Figure 5.3 (a) SEM image of electrodeposited Ir surface; (b) (c) (d) SEM images of

electrodeposited IrOx surface; (e) EDS analysis of image 5.3d.
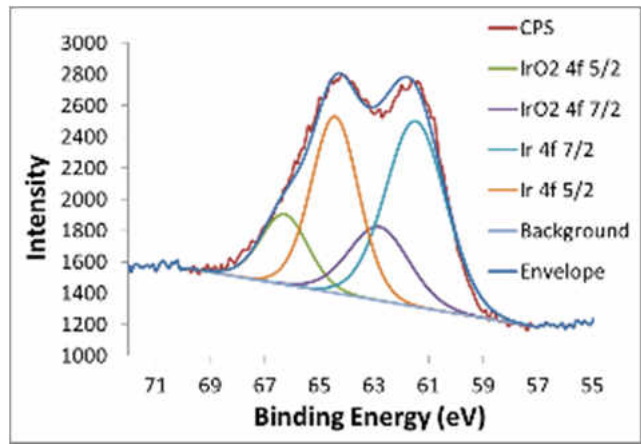
Figure 5.4 XPS spectra of electrodeposited IrOx: Ir 4f spectrum.

5.2.3 Relationship between the electrochemically active surface area and pseudocapacitive charge for electrodeposited IrO$_x$ thin films

The standard UV-Vis intensity-Zn^{2+} concentration curve is plotted in **Fig. 5.5a**. The Zn^{2+} concentration range for the standard curve was 10^{-6}-10^{-5} M. As expected, the amount of absorbed light proportionally decreased with an increase in the zinc concentration. The standard curve provided a reliable way to estimate the quantity of zinc ions adsorbed onto the metal oxide surface by detecting the intensities of the zinc/EBT solution before and after the electrode was immersed.

The pseudocapacitive charge of each catalyst was determined by integrating the CV from 0.3 V to 1.25 V and dividing by the scan rate of 50 mV/s [181–183]. The mass loading was determined by integrating the deposition curve (**Fig. 5.2a**). The pseudocapacitive charge has been shown to be a useful relative measure of the active surface area of iridium oxide [184]. The correlation of zinc surface area with pseudocapacitive charge and zinc surface area with oxide loading are shown in **Figs. 5.5b** and **5.5c**, respectively. The linearity of the ECSA vs. loading plot showed that the bulk and surface structure of the electrodeposited electrode remained similar. The correlation of ECSA vs. charge showed the potential promise to find a constant for the IrO$_2$ system similar to the conversion factor [185–187] for calculating the ECSA of Pt electrocatalysts. The ECSA-charge and ECSA-loading correlations for the electrodeposited IrO$_x$ films were 1776 ($\pm$46) cm^2/C and 34.2 ($\pm$1.3) m^2/g, respectively.

Additionally, the current density at 1.6 V from the OER polarization curve (Fig. 4d) was used to determine the specific and mass activities of the electrodeposited IrO$_x$ catalyst, which were 0.477 ($\pm$ 0.012) mA/cm^2 and 163 mA/mg, respectively.
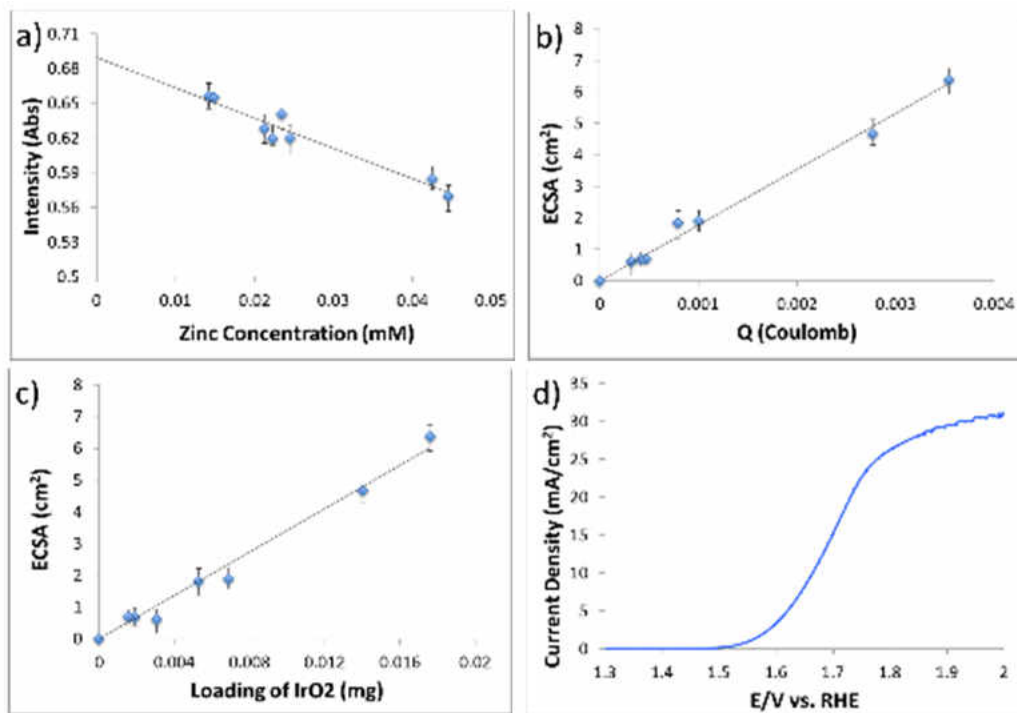
Figure 5.5 (a) Standard intensity-concentration curve; (b) Relationship between the zinc surface area and pseudocapacitive charge; (c) Relationship between the zinc surface area and catalyst mass loading; (d) Polarization curve of IrOx for electrodepostion system at 5 mV/s, 1600 rpm.

5.2.4 Physical characterization of IrO$_x$ powder catalysts

As-received IrO$_x$ powders were observed under SEM and are shown in **Figs 5.6a** and **5.6b**. A single IrO$_x$ particle size around 100 nm in diameter was observed. Most of the particles existed as agglomerates with the diameter around a few hundred nanometers. The pores between agglomerates ranged from tens to several hundreds of nanometers. In order to obtain an accurate pore size distribution and BET surface area, nitrogen adsorption was performed. The pore size distribution of these particles is shown in **Fig 5.6c**. The majority of the pores were mesopores ~2-50 nm in diameter, which are most favorable in electrochemical systems, not only because they are large enough to be accessible to reactants but small enough to significantly increase the surface area of catalysts [188]. Less than one third were micropores, which are not typically electrochemically accessible [189]. The cumulative surface area plot, **Fig. 5.6d**, showed that the mesoporous and macroporous surface area comprised approximately 46.6 m^2/g, 71% of the total BET surface area (65.6 m^2/g).

5.2.5 Extending the IrO$_x$ ECSA method to in-situ powder catalysts

The as-received IrO$_x$ powders were mixed into an ink to be dispersed onto Au disk electrodes. The catalyst layers were oxidized by CV between 0.05 and 1.5 V (**Fig. 5.7a**) in 0.5 M H$_2$SO$_4$. Then, the electrodes were treated identically to the electrodeposited IrO$_x$ electrodes to obtain the ECSA vs. charge and ECSA vs. loading correlations.

Figs. 5.7b and **5.7c** show the correlations of the zinc surface area with pseudocapacitive charge and mass loading of the powders, 1663 ($\pm$97) cm^2/C and 34.8

($\pm$1.3) m^2/g, respectively. These are comparable to the values of the electrodeposited samples. The ECSA was 34.84 m^2/g, 53% of the total BET surface area (65.6 m^2/g) and 75% of the mesoporous and macroporous (expected electrochemically accessible) area, which may be caused by poor infiltration of the electrolyte into relatively deep pores. The specific and mass activities of the in-situ powder catalyst were also similar to the electrodeposited samples, though slightly lower, 0.418 ($\pm$0.024) mA/cm^2 and 145 mA/mg, respectively.

It should be noted that both the ECSA-charge and ECSA-loading slopes for the powdered film were close to those of the electrodeposited IrO$_x$ film, despite the fact that considerable differences existed in the loading and material morphology. This suggests that a universal ECSA-charge constant may exsit for polycrystalline IrO$_x$ in sulfonic acid systems. Therefore, the data from the powder and electrodeposited IrO$_x$ was combined (**Fig. 5.7d**), yielding a "universal" ECSA-charge constant for IrO$_x$ of 1681 ($\pm$60) cm^2/C (or 596 ($\pm$21) μC/cm^2 to be consistant with Pt$_{upd}$ convention).

The experimental correlation above was validated by comparing the electrokinetic parameters of the ferrocyanide/ferricyanide (FEFI) redox couple for both a polycrystalline platinum disk and the IrO$_x$ powder electrodes. The FEFI redox couple was selected because it is a simple outer shell electron transfer, which means facile kinetics where the base metal should have minimal influence on the observed activity. This means that one would expect the kinentic rate constant and the transfer coefficient for the FEFI to be very close to one another for the Pt and IrO$_x$ materials if true ECSA was determined.

The linear sweep voltammogram for the FEFI was collected at 1600 rpm at 5

mV/s in N_2 saturated 0.01 M $K_3Fe(CN)_6$, 0.01 M $K_4Fe(CN)_6$, 0.5 M H_2SO_4 solution between 0 and 1 V. The rate constants were calculated based on the true surface area (H_{upd} region for Pt electrode, and the proposed method for the IrO_x electrode). The rate constant of the FEFI redox couple for Pt electrode, $4.62*10^{-3}$ cm/s, was very close to the literature value, $4.7 (\pm 0.07)*10^{-3}$ cm/s [190]. The rate constant based on the calculated IrO_x ECSA, $4.20*10^{-3}$ cm/s, was very close to the Pt disk value, though differences existed on the electrode surfaces. Also, the transfer coefficients for the reduction of $Fe(CN)_6^{3+}$ for the Pt disk and IrO_x electrodes were nearly identical, 0.312 and 0.338, respectively, and reasonably close to the literature value, 0.23 ± 0.03.

The expected similarity of the Pt and IrO_2 FEFI rate constants further demonstrated the improvement of this method over Savinell's study. Since the measurment must quantify an essetially infinitesimal concentration change ($\Delta\mu M$), the measurement sensivity is very important. For UV-Vis, the sensitivity is mostly machine-dependent and the method can easily detect the color change related to concentration in this work. However, the error in titration experiments is mostly human-based and even small variations in determining the end point for the color change from blue to pink can yield large differences in the measured Zn adsorption. In addition, Savinell's work used HCl to measure the FEFI rate constants and transfer coefficients though the psuedocapacitive charge was determined in H_2SO_4. The differing electrolytes are important because Pt is well known to strongly specifically adsorb Cl^- and IrO_2 can be used as the HCl oxidation catalysts [191] and also strongly adsorbs Cl^- [16]. Therefore, it is not unexpect that these two effects operating in concert would result in the one order of magnitude difference between the theoretical and experimental value in Savinell's

method.

5.2.6 Extending the IrO$_2$ ECSA method to electrolyzer MEAs

Next, the IrO$_x$ ECSA was determined in-situ, in an operating PEM electrolyzer, and the specific and mass activity of the catalyst were determined. CVs were collected at a 50 mV/s scan rate with 100% humidified H$_2$ fed to the Pt electrode and nitrogen saturated liquid DI water fed to the IrO$_x$ electrode, **Fig. 5.7e**. The voltammogram achieved a steady state after around 50 cycles. The shape and characteristic peaks for IrO$_x$ in the electrolyzer were slightly different from the ones collected in the three-electrode RDE setup-this is because the Pt electrode in the electrolyzer is only a pseudo reference electrode where the absolute potential is unknown and its polarizability questionable. Most notably for the electrodeposited IrO$_x$ CV shown in **Fig. 5.2d**, characteristic redox peaks at around 0.9 V, corresponding to the Ir(III)/Ir(IV) solid state redox transitions [192], were profound. In the IrO$_x$ powder catalyst (**Fig. 5.7a**), two similarly broad peaks appeared at 0.9 and 1.4 V; however, the pre-peak at around 0.8 V preceding the Ir^{3+}/Ir^{4+} redox transition (as shown in **Fig. 5.2a**) disappeared. In the MEA, the two peaks at 0.9 and 1.4 V observed with the previous two systems were merged together in the CV. Additionally, the potential window was shifted by 0.3 V. In the ex-situ tests, the integrated potential window was 0.3-1.25 V. In the MEA, the integratable voltage limits were shifted to 0.6-1.55 V. The integration limits were selected based on the position of the IrO$_x$ characteristic peaks.

The ECSA obtained from the pseudocapacitive charge was 1.81 (±0.065) m^2, and specific ECSA was 32.55 m^2/g. Comparing with the ex-situ specific ECSA in the operating electrolyzer, the surface utilization was over 93%. Finally, the specific and

mass activities of the catalyst in the electrolyzer at 80 □ were determined by the current density at 1.6 V in the polarization curve (**Fig. 5.7f**), 0.401 ($\pm$0.014) mA/cm^2 and 131.82 mA/mg, respectively, only slightly less than the ex-situ activity.

5.3 Summary

A method was demonstrated to calculate the ECSA of iridium oxide as an anode catalyst material for the oxygen evolution reaction in an operating PEM electrolyzer, which showed promising results at the bench scale. The ECSA was estimated using the total area of the adsorbed zinc ions onto the metal oxide ex-situ. The ECSA demonstrated good linearity with the pseudocapacitive charge for both electrodeposited and powder IrO$_x$ films. The experimental ECSA-charge constant for IrO$_x$ was 1681 ($\pm$60) cm^2/C (or 596 ($\pm$21) μC/cm^2). The final application of this method to the in-situ ECSA calculation of IrO$_x$ in PEM electrolyzer gave the estimated ECSA, 1.81 ($\pm$0.065) m^2 over a 25-cm^2 geometric area. The catalyst utilization in the MEA was >93%, and the specific and mass activities were 0.401 ($\pm$0.014) mA/cm^2 and 132 mA/mg at 1.6 V, respectively.
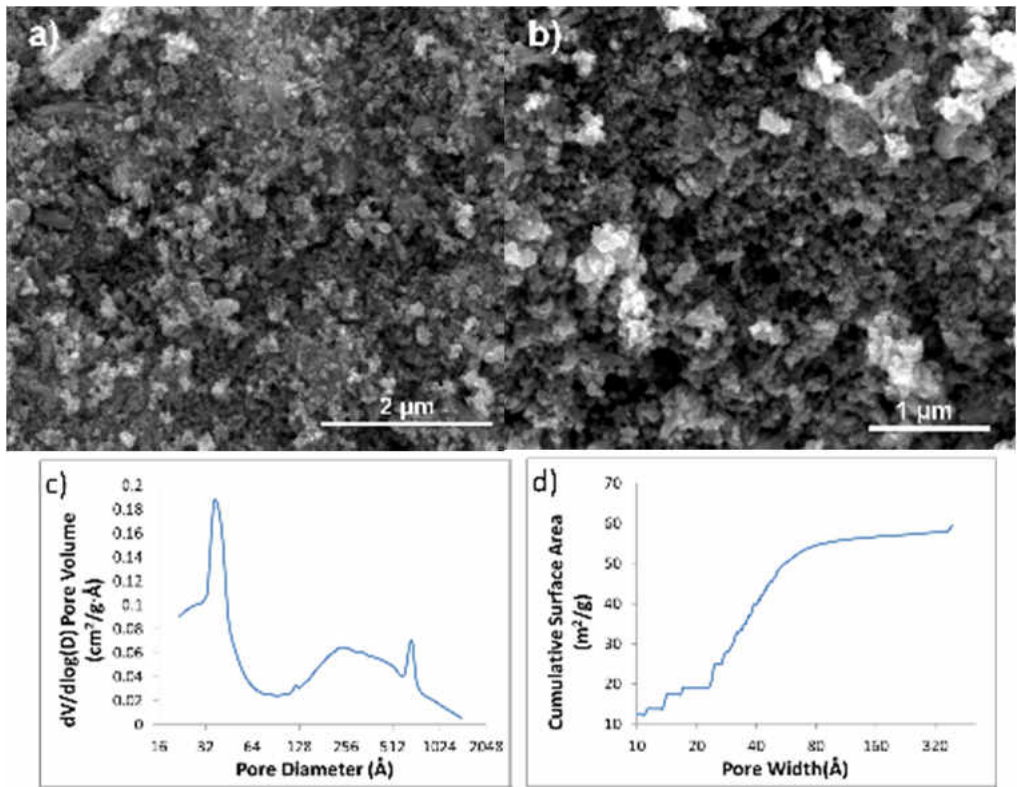
Figure 5.6 (a) (b) SEM images of IrOx powder catalysts; (c) Pore size distribution of

IrOx powder catalysts; (d) Cumulative surface area of IrOx powder catalysts.
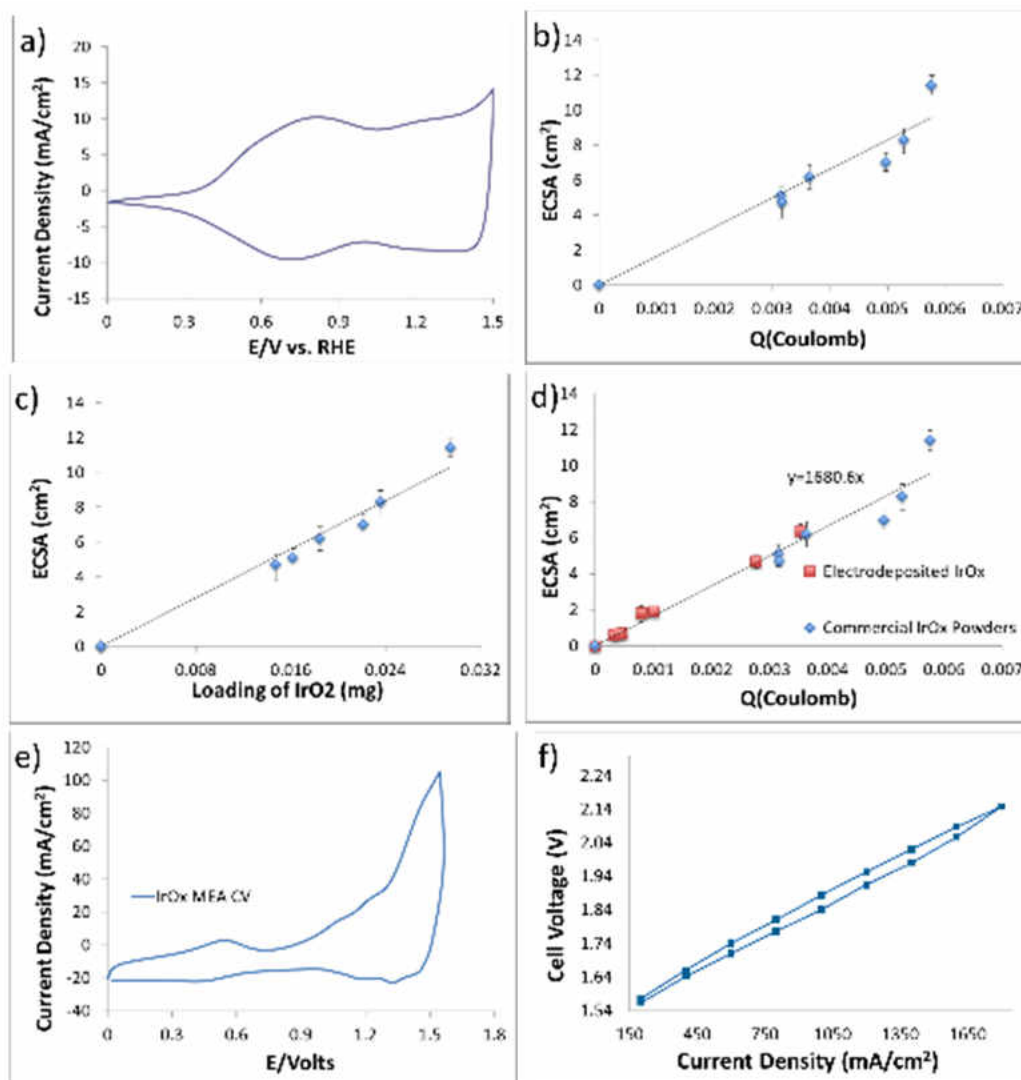
Figure 5.7 (a) CV oxidation of IrOx powders; (b) Relationship between the zinc surface area and pseudocapacitive charge for catalyst powder electrode; (c) Relationship between the zinc surface area and catalyst mass loading for catalyst powder electrode; (d) Relationship between the zinc surface area and pseudocapacitive charge for two systems; (e) Cyclic voltammetry of IrOx anode material in MEA; (f) OER polarization curve of IrOx anode material in MEA.

CHAPTER 6 – STABILITY AND ACTIVITY OF PT-ITO ELECTROCATALYST FOR OXYGEN REDUCTION REACTION IN ALKALINE MEDIA

6.1 Objective

The oxygen reduction reaction (ORR), which occurs at the (alkaline fuel cell) AFC and anion exchange membrane fuel cell (AEMFC) cathode, is one of the most widely studied reactions to date. Though the shift in potential with pH is very well known (0.059V/pH) and often discussed, the differences in the electrochemical interface and its role in the ORR mechanism are not as well known or widely discussed. First, the lower potential required for the ORR in alkaline media changes the surface free energy, weakening the Pt-O bond energy compared to acid electrolyte [30]. This decreased bond energy decreases the overpotential for the ORR in alkaline media relative to acidic media. Simply put, the ORR in alkaline media is more facile than it is in acid and catalytic activity has been observed over much of the periodic table from carbon compounds, to various transition metals and metal oxides. Although some high activity non-platinum group metal catalysts have been shown for the ORR in alkaline media, Pt-based catalysts still remain the most popular in the literature because of their proven combination of high stability and activity. However, the properties of the ORR suggest that even lower Pt loading are possible in alkaline media, leading to lower overall system cost.

One method to decrease the Pt loading is to use alternative support materials to carbon that are able to manipulate the Pt dispersion, size, shape, etc. through electron transfer between the catalyst and support. Metal−support interactions can also improve the electrocatalytic activity of the supported Pt in several ways such as modification of

91

the electronic states of Pt to increase the potential of the formation of Pt-OH groups and reduction of the equilibrium OH adsorption by lateral repulsion between Pt-OH and oxide surface [72]. Recent study on ITO nanoparticles (NPs) as a high stability non-carbon support for Pt NPs [154] showed that the mass activity of Pt/ITO for the ORR in acidic media was considerably higher than that of the 2020 DOE goal [193], which may be due in part to epitaxial Pt orientation dictated by the metal oxide surface [194]. The ITO support material also demonstrated great stability, even in a harsh acidic and oxidizing environment. This result further supported previous work that the strong interaction between Sn and Pt suppresses the formation of Pt-oxide species at high potentials to provide a clean surface over a wide potential range and is beneficial for the stability of Pt [195]. Therefore, metal oxides, as catalyst support materials, can provide modifications for Pt to increase the electrocatalytic activity and stability.

In this study, the application of ITO as an electrocatalyst support for Pt in alkaline media was explored. The ORR activity and stability of Pt/ITO were compared with a commercial Pt/Vulcan electrocatalyst. The differences of Pt/ITO catalyst in acidic and alkaline media, and the possible reasons for its high activity and stability are discussed.

6.2 Results and Discussion

6.2.1 Evaluation of Crystal Structure Using XRD

A powder XRD pattern of the as-synthesized support material composed of ITO NPs with phase identification is shown in **Figure 6.1**. Five major peaks and three minor peaks were observed between the 20° and 65° diffraction angle (2θ) located at 21.32° (211), 30.60° (222), 35.45° (400), 37.51° (411), 41.74° (332), 45.54° (431), 50.96° (440)

and 60.55° (622). The observed pattern corresponded well with a bixbyite In_2O_3 cubic structure (JCPDS 06-0416) with no secondary phases showing that elements tin and indium did not exist as segregated solid oxides, rather tin existing as a dopant into the indium oxide lattice. The average grain boundary size for the ITO NPs was calculated from the Scherrer equation, **Eq. 6.1**:

$$D = \frac{k\lambda}{B\cos\vartheta} \tag{6.1}$$

where D is the grain boundary size (nm), k is the shape factor (taken as 0.89), λ is the X-ray wavelength (nm), B is the width (radians) at half the maximum peak intensity, and θ is the Bragg angle. The average side length for the cubic ITO NPs was 26.74 nm.

6.2.2 Nanostructure of As-Synthesized ITO Electrocatalyst Supports and Platinized ITO.

The representative morphological features of the as-prepared metal oxides were examined by transmission electron microscopy (TEM), shown in **Figure 6.2a**. The support ITO NPs exhibited a cubic-like shape with a mean particle size around 22 nm (side length), which were evaluated from an ensemble of approximately 50 particles in arbitrary areas of the corresponding TEM images, such as **Figure 6.2a**. The high-resolution TEM images in **Figure 6.2b** show a well-crystalized lattice structure with a highly ordered continuous fringe pattern. The size of the Pt NPs supported on ITO was around 5 nm (typical value) in diameter, as can be observed from the small darkly contrasting spherical Pt NPs dispersed on the supports in **Figure 6.2c**.
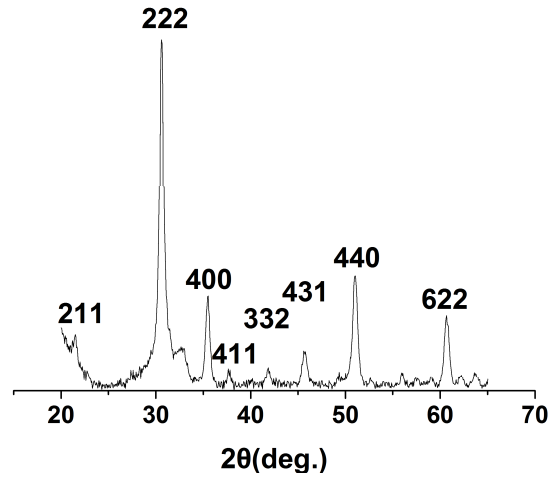
Figure 6.1 Powder XRD patterns for pure ITO crystals with 5 atom % of Sn content.
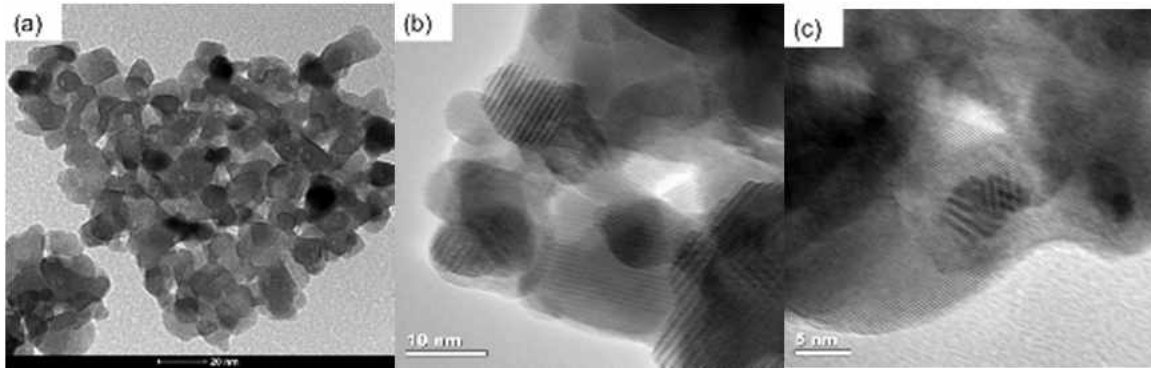
Figure 6.2 (a) TEM images of ITO NPs; (b) high-resolution TEM images of ITO NPs; (c) Pt NP supported on ITO.

6.2.3 Surface Characterization of Prepared ITO Support and Pt/ITO

The surface compositions of ITO and Pt/ITO were examined by XPS. The activity and stability of electrocatalysts can be evaluated by the surface composition. Changes that occur during operation can provide critical information about what happens to the electrocatalyst in the reaction environment. **Figure 6.3** shows the broad XPS survey (**a**), focused C 1s (from carbon tape) (**b**), focused In 3d (**c**) and focused Sn 3d (**d**) spectra of the as-synthesized ITO NPs. In the survey spectra, with binding energy from 1100 to 0 eV, all of the expected elements were observed: fluorine (Nafion®), oxygen, tin, indium, and carbon (substrate). The atomic percentage of tin on the surface was about 14%, almost three times that of the bulk, which could be caused by Sn surface segregation in the ITO structure.

The binding energies for all the elements were referenced to the C 1s main peak. As shown in **Figure 6.3b**, there was a small satellite peak on the higher binding energy side of the C 1s main peak suggesting there were more than one types of carbon on the sample holder. Six different peaks were fitted to the main and satellite peaks to get the closest value of full width at half maximum (FWHM), which is 1.8 for graphitic carbon. Therefore the peak with the largest area was chosen as the calibration reference.

The high-resolution spectra for In 3d in **Figure 6.3c** could only be deconvoluted into one doublet at 444.37 eV and 451.91 eV. They corresponded with the binding energy of In^{3+} $3d_{5/2}$ and In^{3+} $3d_{3/2}$. However, the high-resolution spectra for Sn 3d was deconvoluted into two doublets (four peaks). The generally accepted value for the deconvoluted peaks of Sn^{4+} $3d_{5/2}$ and Sn^{2+} $3d_{5/2}$ are 487.1 eV and 486.1 eV, respectively, which can be used to distinguish Sn^{4+} and Sn^{2+} states and their relative concentrations on

the ITO surface as shown in **Figure 6.3d**. The binding energies of the first deconvoluted doublet peaks labeled by blue lines corresponded to the Sn^{4+} $3d_{5/2}$ and Sn^{4+} $3d_{3/2}$. The second doublet peaks labeled in red lines in the lower binding energy area were consistent with Sn^{2+} $3d_{5/2}$ and Sn^{2+} $3d_{3/2}$. 96.5 atom % of Sn in the as-prepared ITO support existed in the Sn^{4+} state with the balance being Sn^{2+}.

The surface compositions of fresh Pt/ITO and Pt/ITO after 40 break-in cycles in N_2-saturated $HClO_4$ electrolyte were also investigated by XPS. From the survey spectra of Pt/ITO shown in **Figure 6.4a**, Pt 4f peak was also observed in addition to the expected elements from ITO.

The high-resolution spectra for Sn 3d was again deconvoluted into two doublets for Sn^{4+} and Sn^{2+} states, with the difference that the percentage of Sn^{2+} on the surface increased from 3.5% (fresh ITO in **Figure 6.3d**) to 9% (as-deposited Pt/ITO in **Figure 6.4b**) and then to 20% (Pt/ITO after break-in cycles in **Figure 6.4c**). Both the electrochemical deposition of Pt onto the ITO NPs and the protonated break-in cycling in the electrolyte played a role in the reduction of the surface Sn. It is known that the tin atoms at the interface with Pt can be reduced by a Schottky junction formed by aligning Fermi levels [196]. Another significant difference was that after referencing to the C 1s main peak for all the XPS samples, the positions of the Sn and In for Pt/ITO shifted negatively by around 0.3 eV compared to those in pure ITO NPs. This may support the existence of a strong metal-support interaction between Pt and ITO, which may result in electron transfer between Pt and surface Sn, impacting activity and stability of Pt/ITO.
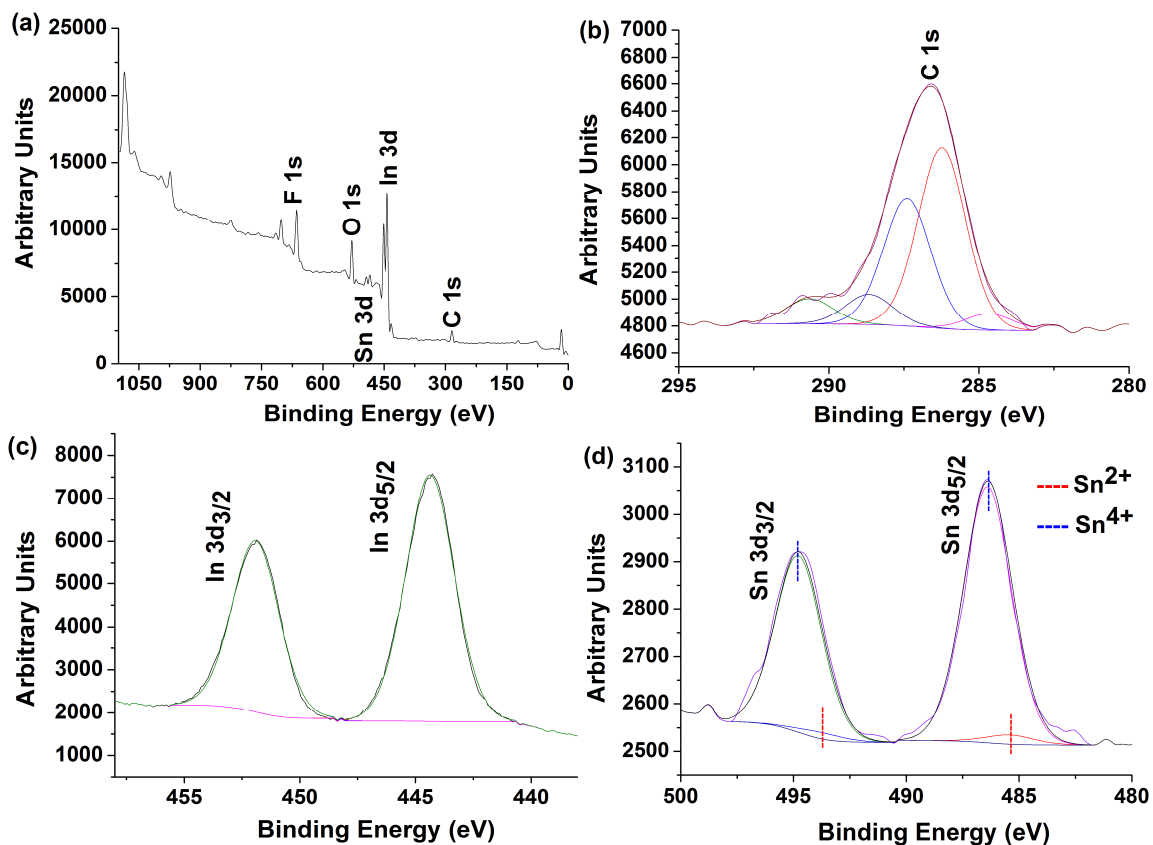
Figure 6.3 (a) XPS survey spectra of the as-synthesized ITO NPs; (b) focused C 1s spectra of ITO NPs supported on carbon tape; (c) focused In 3d spectra of the as-synthesized ITO NPs; (d) focused Sn 3d spectra of the as-synthesized ITO NPs.
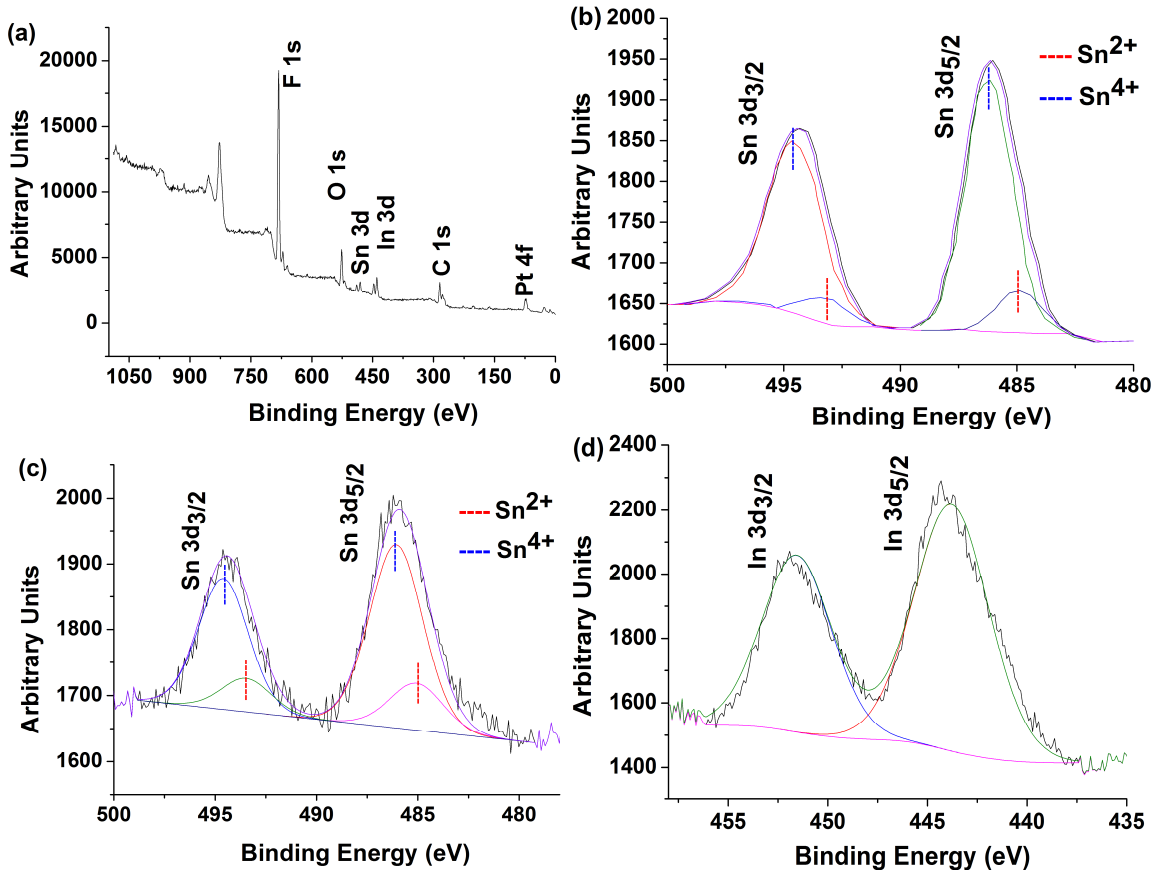
Figure 6.4 (a) XPS survey spectra of the Pt/ITO; (b) focused Sn 3d spectra of fresh Pt/ITO; (c) focused Sn 3d spectra of Pt/ITO after 40 cycles of breaking in; (d) focused In 3d spectra of Pt/ITO.

6.2.4 CVs and ECSA of Pt/ITO in alkaline media

CV of Pt/ITO in N_2-saturated 0.1 M KOH solution at 25°C is shown in black in **Figure 6.5** after positively shifting the working potential range by 0.708V ($E_{shifted}$ = 0.059V/pH* (13_{pH} -1_{pH}) = 0.708 V) in order to be consistent with activity studies in acidic media. The shifted CV showed two distinct potential regions. The specific adsorption of hydroxide anions and Pt oxidation was observed above 0 V [197]. Hydrogen adsorption/desorption processes were observed between -0.7 < E < -0.35 V, caused by proton transfer from water molecules co-adsorbed on the electrode surface in alkaline media as opposed to direct proton underpotential adsorption in acid media. The difference in the proton source in alkaline vs. acid media explains why the hydrogen adsorption/desorption peaks are much smaller than that in acidic solution, which can be clearly observed in the comparison in **Figure 6.5**. It also explains why the double layer region is not as wide in alkaline media as it is in acid media [198].

On account of the more complex interface between the catalyst and electrolyte in alkaline media, electrochemically active surface area (ECSA) determination is nearly always performed by hydrogen adsorption in acid media. The ECSA was determined by integrating the hydrogen adsorption charge (Q_r) in the negative-going underpotential scan (0.40-0.075 V) in N_2-saturated 0.1 M $HClO_4$ electrolyte (**Figure 6.5**) after correction for double-layer charges. As shown in **Equation 6.2**,

$$ECSA = \frac{Q_r}{m \times C} \tag{6.2}$$

where m is the mass of Pt loading, Q_r is the H_2 underpotential adsorption charge, C is the charge of a full monolayer coverage of H atoms on clean polycrystalline Pt (210 µC cm^{-2}).
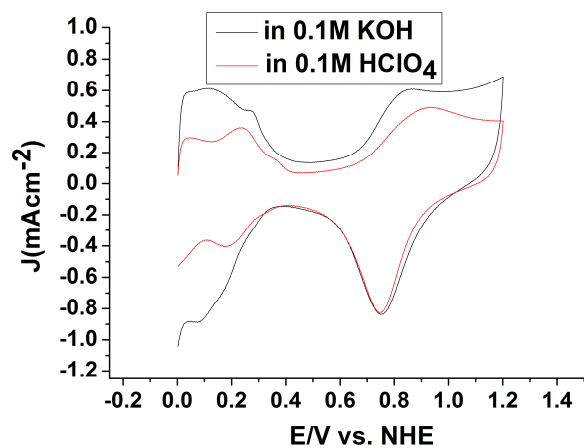
Figure 6.5 Pt/ITO CV comparison in acidic and alkaline media (CV in KOH was shifted by ~0.7 V).

The Pt/ITO ECSA in this work was 74.4 m^2/g_{Pt}, almost three times that of Pt/Vulcan ($27.3 \ m^2/g_{Pt}$).

6.2.5 ORR activity of Pt/ITO in alkaline media

The oxygen reduction activity of Pt/ITO in alkaline media was studied by anodic linear sweep voltammograms and compared to that of Pt/Vulcan in alkaline media. The ORR measurements for both Pt/ITO and Pt/Vulcan rotating-disk electrodes (RDEs) were performed in O_2-saturated 0.1 M KOH at a scanrate of 10mV/s from 400 RPM to 2500 RPM, which was repeated five times to ensure reproducibility. The Pt/ITO loading was approximately 16.5 µg cm^{-2} (the total loading of Pt and ITO NPs), whereas the loading was approximately 27.6 µg cm^{-2} for Pt/Vulcan. From the comparison of the 1600-RPM polarization curves (**Figure 6.6a**) of Pt/ITO and Pt/Vulcan, the half-wave potential of Pt/ITO was 17 mV more positive than that of Pt/Vulcan, suggesting more facile kinetics.

A complete ORR kinetic investigation was carried out by Koutecky-Levich analysis of the background-corrected (by subtracting background current measured under identical conditions under N_2 atmosphere without rotation) and IR-corrected (by subtracting the current multiplied by the solution resistance) polarization curves. A well-developed diffusion limited current density plateau for Pt/ITO, J_{lim} (~5.2 mA cm^{-2}), was observed from -0.7 V to -0.1 V. J_{lim} was within the 10% margin of the theoretical diffusion limiting current calculated from Levich Equation ($J_{lim} = 0.62nFD_i^{2/3}v^{-1/6}C_o^*w^{1/2}$ = 5.66 mA cm^{-2}), followed by the mixed kinetic-diffusion control region -0.1 V < E < 0.1 V. Therefore the kinetic current (I_k) was obtained by **Equation 6.3** [4]:

$$I_k(A) = \frac{I_{lim}(A) \times I(A)}{(I_{lim} - I)} \qquad (6.3)$$

Then, the specific activity of the Pt/ITO catalyst (calculated from the 1600-RPM polarization curve) in KOH electrolyte was calculated by normalizing I_k to the Pt electrochemical surface area according to **Equation 6.4** [4]:

$$I_s(\mu A cm_{Pt}^{-2}) = \frac{I_k(A)}{Q_{H-adsorption}(C)/210\mu Ccm_{Pt}^{-2}} \tag{6.4}$$

Which was 0.326 ± 0.04 mA cm^{-2} at 0.1 V, 2.65 times of that of Pt/Vulcan (0.123±0.01 mA cm^{-2}). The obtained experimental value of the specific activity of Pt/Vulcan was comparable to the activity of synthesized Pt/Vulcan (0.120 mA cm^{-2}) previously reported [199]. The mass activity of Pt/ITO catalyst in KOH was obtained by normalizing I_s to Pt mass loading on the electrode. The mass activity for the Pt/ITO catalyst (243 mA/mg$_{Pt}$) was about 1.47 times greater than that of Pt/Vulcan (98.3 mA/mg$_{Pt}$) in alkaline media, and much higher than the previously reported (60 mA/mg$_{Pt}$).

From -0.4V to 0.05V, linear Koutecky−Levich plots of both Pt/ITO (**Figure 6.6c**) and Pt/Vulcan were observed (assuming both first order kinetics), plotting J^{-1} vs. ω$^{-1/2}$ [200].

$$\frac{1}{J} = \frac{1}{J_k} + \frac{1}{J_{diff}} = \frac{1}{J_k} + \frac{1}{B\omega^{1/2}} \tag{6.5}$$

$$B = 0.62nFC_0D_0^{2/3}\eta^{-1/6} \tag{6.6}$$

where J_k and J_{diff} are the kinetic and diffusion limited current densities respectively, F is the Faraday constant, C_0 is the saturated concentration of O$_2$ in the 0.1 M KOH electrolyte (1.21 × 10^{-3} mol/L), D_0 is the diffusion coefficient of O$_2$ in the KOH electrolyte (1.86 × 10^{-5} cm^2 s), and η is the viscosity of the electrolyte (1.008 × 10^{-2} cm^2 s). From the slopes (1/B) of the Koutecky-Levich plots at different potentials between -0.4V to 0.05V, the average number of electrons, n, involved in the ORR in alkaline media can be obtained. Over the entire potential range, it was found that for Pt/ITO, n≅4 and for

Pt/Vulcan, n≅3.54, which indicated that Pt/Vulcan can be more active in alkaline media to produce peroxide-like intermediates in the ORR mechanism than Pt/ITO.

Figure 6.6d shows the Tafel plot for the ORR on Pt/ITO in KOH electrolyte at 1600 RPM. It shows two clearly discerned Tafel regions, which are 0.05 V to 0.15 V and 0.15 V to 0.2 V, with corresponding slopes of 129 mV/dec and 69 mV/dec, respectively. They can be attributed to the formation and adsorption of surface oxides on the Pt surface. This is consistent with literature data on supported polycrystalline Pt nanoparticles.

6.2.6 Electrochemical Stability of Raw and Platinized ITO Supports.

Though ITO crystals have shown good bulk chemical stability in acid and alkaline media, previous studies have shown that the ITO surface composition can change significantly during electrochemical treatment, particularly at elevated potentials [201]. CVs of raw ITO supports in both O_2-saturated and N_2-saturated 0.1 M KOH were collected at room temperature without rotation to determine the intrinsic redox stability of ITO in the potential window relevant to the ORR. For all curves in the oxygenated alkaline electrolyte, there were no obvious redox peaks, and raw ITO only showed typical capacitive behavior.

Stability was investigated by cycling the potential of Pt/ITO between -0.2 and 0.4 V for 300 cycles at 10 mV/s without rotation in O_2-saturated 0.1 M KOH electrolyte. There was a slight decrease in both the ECSA (**Figure 6.7a**) and the current density for the reduction of Pt-O. After 300 cycles, the ECSA (**Figure 6.7a**) decrease was approximately 17.4%, less than half of the 37.5% decrease found for the commercial Pt/Vulcan electrocatalyst (**Figure 6.7b**). After 300 cycles, the ORR half-wave potential shifted negatively by 20mV, the specific activity was decreased from 0.326 ± 0.04 mA

cm^{-2} to 0.291 ± 0.001 mA cm^{-2} (**Figure 6.7c**), which compared favorably to both the shift in the half-wave potential (50mV) and specific activity of Pt/Vulcan. The stability of Pt/Vulcan was also explored under the same conditions as Pt/ITO. But the half-wave potential shift of Pt/Vulcan was 50mV (**Figure 6.7d**), which means the performance stability of Pt/ITO catalyst for ORR in alkaline media was improved compared to Pt/Vulcan.

The change in the surface composition after cycling was investigated by XPS (**Figure 6.8**). In the XPS spectra, surface In existed only as In$_2$O$_3$ showing no other state even after 300 cycles (**Figure 6.8a**). However, the percentage of Sn^{2+} on the surface increased from 20% before electrochemical reaction to 87% after 300 cycles (**Figure 6.8b**). Although the surface Sn^{4+} was gradually reduced to Sn^{2+} state during the stability cycling (**Figure 6.8c**), the specific activity of Pt/ITO after stability test was still 2.77 times that of commercial Pt after its stability test.
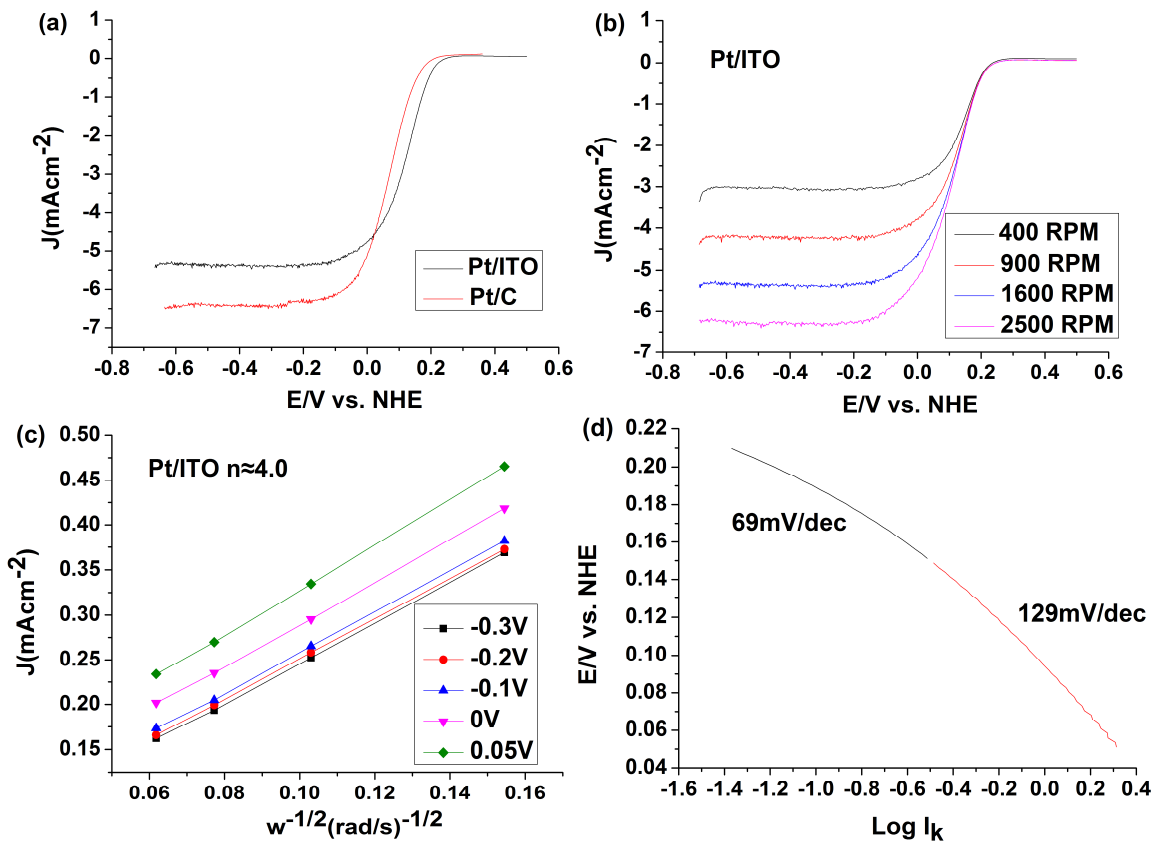
Figure 6.6 (a) Comparison of the ORR polarization curves in alkaline media under 1600 RPM of Pt/ITO and Pt/Vulcan; (b) room temperature rotating disk voltammograms of Pt/ITO electrocatalyst in O_2-saturated 0.1 M KOH, scanrate, 10 mV/s; (c) Koutecky−Levich plots (J^{-1} vs. $\omega^{-0.5}$) of Pt/ITO at different potentials; (d) Tafel plot of Pt/ITO derived by the mass-transport-corrected 1600 RPM polarization curve.
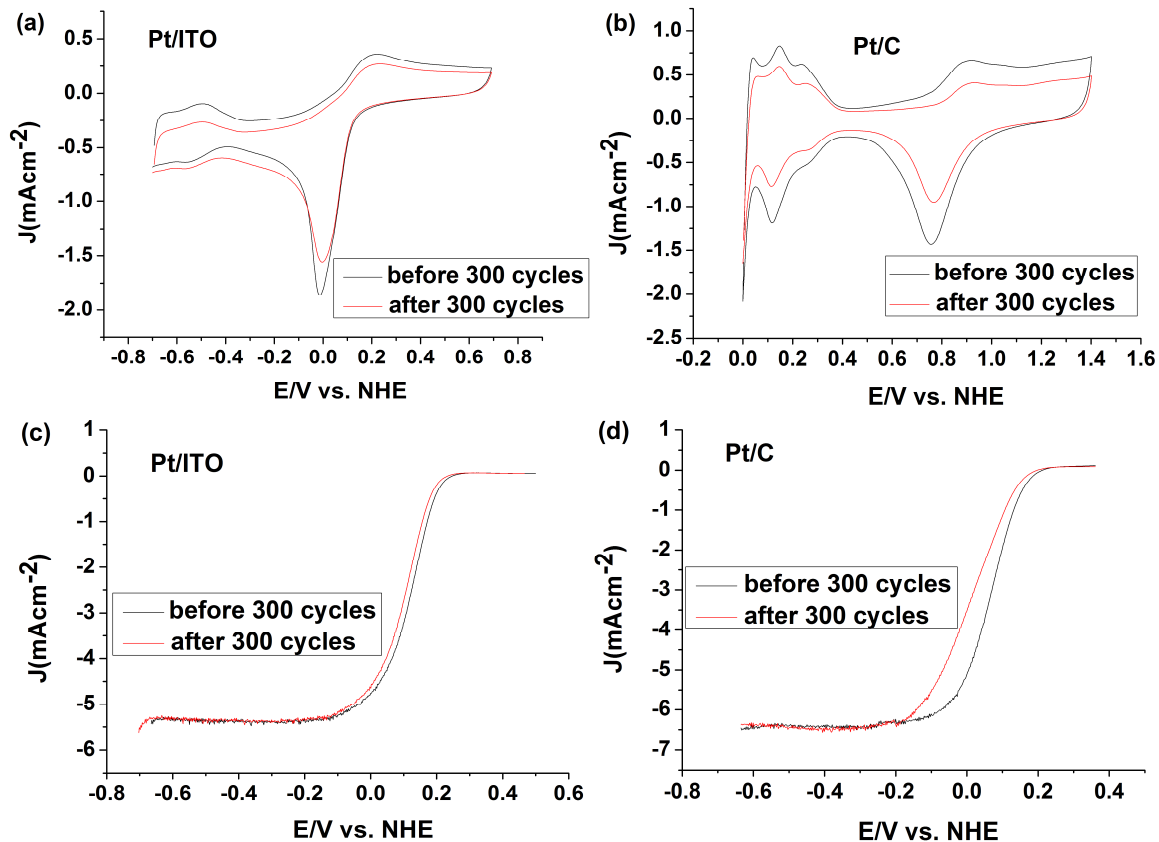
Figure 6.7 (a) CV comparison of Pt/ITO between -0.7 V and 0.7 V of before and after 300 cycles, in oxygen-saturated electrolyte; (b) CV comparison of Pt/Vulcan before and after 300 cycles, in nitrogen-saturated electrolyte; (c) ORR polarization curve comparison before and after 300 cycles on Pt/ITO catalysts on RDE. Sweep rate, 10 mV/s; rotating rate, 1600 RPM, (Pt loading: 6.3μg cm^{-2}); (d) ORR polarization curve comparison before and after 300 cycles on Pt/Vulcan catalysts on RDE. Sweep rate, 10 mV/s; rotating rate, 1600 RPM, (Pt loading: 17.3 μg cm^{-2}).
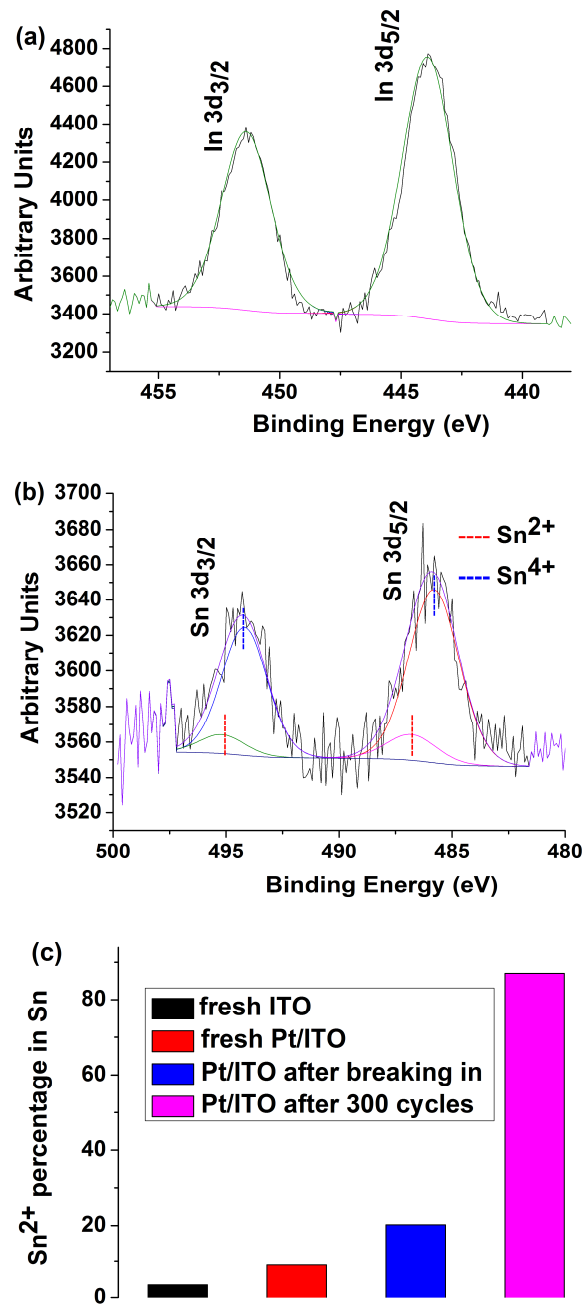
Figure 6.8 (a) In spectra in Pt/ITO after durability test; (b) Sn spectra in Pt/ITO after durability test; (c) surface composition differences between fresh ITO, fresh Pt/ITO, Pt/ITO before (after breaking in cycles) and after 300 cycles of reaction.

6.3 Summary

ITO was used as a support material for Pt and the electrocatalytic performance of Pt/ITO was evaluated for the ORR in alkaline environment and compared to commercial Pt/Vulcan. It was found that the mass activity and specific activity of Pt in Pt/ITO were significantly higher than Pt/Vulcan. Additionally, the stability of the Pt/ITO electrocatalyst was also better than Pt/Vulcan after a 300-cycle stability test between -0.2-0.4V in O_2-saturated alkaline electrolyte. The ECSA loss in Pt/ITO was less than half of that in Pt/Vulcan. The Pt/ITO electrocatalyst maintained a high activity for ORR despite progressively reduced surface Sn during potentiometric cycling, which raises further questions into the Pt-support interaction mechanism for the oxygen reduction reaction in alkaline media, which should be investigated in future work. The purposeful utilization of Pt-support interactions may lead to promising new catalysts for the ORR and many other reactions of commercial interest.

CHAPTER 7 – HIGHLY DURABLE AND ACTIVE COBALT OXIDE NANOCRYSTALS SUPPORTED ON CARBON NANOTUBES AS BIFUNCTIONAL ELECTROCATALYSTS IN ALKALINE MEDIA

7.1 Objective

The unitized regenerative fuel cell (URFC), which at its core is an integration of a fuel cell and electrolyzer in the same stack, has received significant attention as an alternative technology for energy conversion and storage. Among these unitized reversible fuel cells, alkaline URFCs have become increasingly attractive over the past few years due to their potential low cost and high-energy storage capacity. Unfortunately, the adoption of alkaline URFCs have been challenging due to limited membrane stability and slow reaction kinetics [26][202]. Therefore, developing high-performance oxygen reduction reaction (ORR)/oxygen evolution reaction (OER) bifunctional catalysts is considered one of the most critical needs to enable the commercial viability of reversible AMFCs.

Modified transition metal oxides [102][109][203–205] and novel synthesis techniques [206] have been shown to lead to catalysts with improved ORR/OER activities and durability, but they still generally suffer from poor dispersion and low conductivity with slow charge carrier mobility. Carbon nanotubes (CNTs) have been extensively used as electrode materials in many energy storage systems because of their high electronic conductivity and excellent stability [142][207–211]. Therefore, hybrid transition metal oxide-CNT structures have become popular in recent bifunctional catalyst studies [78][140][148][212,213]. Dai et al. discovered excellent ORR activity for Co_3O_4

supported on reduced graphene oxide, which also showed reasonable OER activity [136]. Liang et al. found that the ORR activity can even be enhanced by incorporating Mn into the Co_3O_4 lattice to increase the catalytic sites in the same hybrid structure using the same synthesis technique [77]. Later, Singh et al. proposed an approach to synthesize Co_3O_4 supported on N-doped graphene with preferential exposure of low surface energy facets, which showed a low overpotential (~280 mV) for OER at a current density of 10 $mAcm^{-2}$ [141]. Mao et al. reported high-performance ORR/OER bifunctional 3D crumpled graphene-cobalt oxide nanohybrids, which were amongst the best-performing non-PGM OER catalysts in 2014 [214]. Though catalysts with high activity have been shown, almost none of these studies discussed the durability of these bifunctional catalysts in the combined potential range of both ORR and OER reactions.

Here, a procedure to develop durable and active bifunctional ORR/OER electrocatalysts in alkaline media is reported [215]. Catalysts with hybrid structures (metal oxides on functionalized CNTs) that can survive the harsh ORR/OER environments (from 0.0 V to 1.9 V) and demonstrate long-term stability are synthesized for the first time. A rational durability-mechanism-synthesis relationship for the application of hybrid electrocatalysts for alkaline URFCs was identified. The hybrid structure was achieved by nucleating cobalt oxides on functionalized CNTs through hydrolysis and hydrothermal treatment. The supported catalyst was subsequently reduced to repair the CNTs as much as possible to minimize the number of corrosion sites. A combination of physical and electrochemical characterization techniques were used to analyze the effect of synthesis parameters upon catalyst durability and activity.

7.2 Results and Discussion

7.2.1 Oxidation Agents

In order to grow transition metal oxides onto CNTs forming a covalent bond between the oxide and support to promote adhesion, the CNTs need to be functionalized initially to provide enough anchoring sites for metal oxide deposition. One of the most common ways to introduce oxygen functional groups to carbon materials is chemical oxidation. The various oxygen functional groups introduced in this process may include the generally present carboxyls, carboxylic anhydrides, and lactones, as well as aldehydes, ethers, hydroxyl groups exhibiting phenolic character, carbonyl groups such as quinones or pyrones [132–134]. V. Datsyuk et al. measured the oxidation degree of multi-walled CNTs treated by different oxidation agents through Raman spectroscopy and X-ray photoelectron spectroscopy [129]. They concluded that the increase in the degree of surface oxidation follows the trend of hydrochloric acid < ammonium hydroxide/hydrogen peroxide < piranha < refluxed nitric acid. Treatment with all these oxidizing agents, except nitric acid, does not lead to production of additional defects on the outer walls of multi-walled CNTs. Therefore, the oxidants used in this work were narrowed down to nitric acid and potassium permanganate [131]. The two batches of oxidized CNTs (oCNTs) used in this study were oxidized ($KMnO_4$ and HNO_3) for different lengths of time to achieve the same overall oxidation degree.

The high-resolution C 1s XPS spectra of the oCNTs prepared by $KMnO_4$ (**Fig. 7.1a**) and HNO_3 (**Fig. 7.1b**) were collected with a pass energy of 50 eV within binding energy window from 280 eV to 294 eV, which was determined by a survey scan from 0 to 1100 eV with a 100 eV pass energy. Both oCNT high-resolution C 1s spectra of the oCNTs

112

were analyzed with a Gaussian fitting model and Linear curve as the background to control the full width at half maximum height of all the fitted peaks between 1.78 to 1.82. Then both C 1s spectra were deconvoluted into 5 bands, corresponding to (from low to high binding energy): graphitic carbon at 284.5 eV, carbon singly bound to oxygen in phenols and ethers like C-O at 286.1 eV, carbon doubly bound to oxygen in ketones and quinones such as C=O at 287.5 eV, carbon bound to two oxygens in carboxyls, carboxylic anhydrides, and esters (i.e., -COO) at 288.7 eV, and the characteristic shakeup line of carbon in aromatic compounds at 290.5 eV (π-π*transition), respectively[130][216]. They demonstrated similar associated oxygen percentages, leaving the graphitic C percentage around 52%. However, they showed a different composition than the functionalized carbon. The $KMnO_4$-derived oCNT exhibited a larger shoulder at higher binding energy (around 289 eV) area showing a higher percentage of carbon doubly bound to oxygen and bound to two oxygens. The deconvolution of the O 1s spectrum for the oCNTs ($KMnO_4$) (**Fig. 7.1c**) and oCNTs (HNO_3) (**Fig. 7.1d**) resulted in two peaks: oxygen doubly bound to carbon (i.e., O=C) in quinones, ketones, and aldehydes at 531.6 eV, and oxygen singly bound to carbon (i.e., O-C) in ethers and phenols at 533.2 eV. The difference between the two was that the ratio of C-O double bonds to single bonds is 1:1 for oCNTs ($KMnO_4$), similar to the literature value [217] and 1:2 for oCNTs (HNO_3) [130], corresponding well with the C 1s analysis. These differences in surface oxidation may account for the different crystallization observed in TEM images (**Fig. 7.2**).

The TEM images for both methods revealed differences in nucleation and distribution of the metal oxides along the oCNTs. The batch oxidized by $KMnO_4$ shown
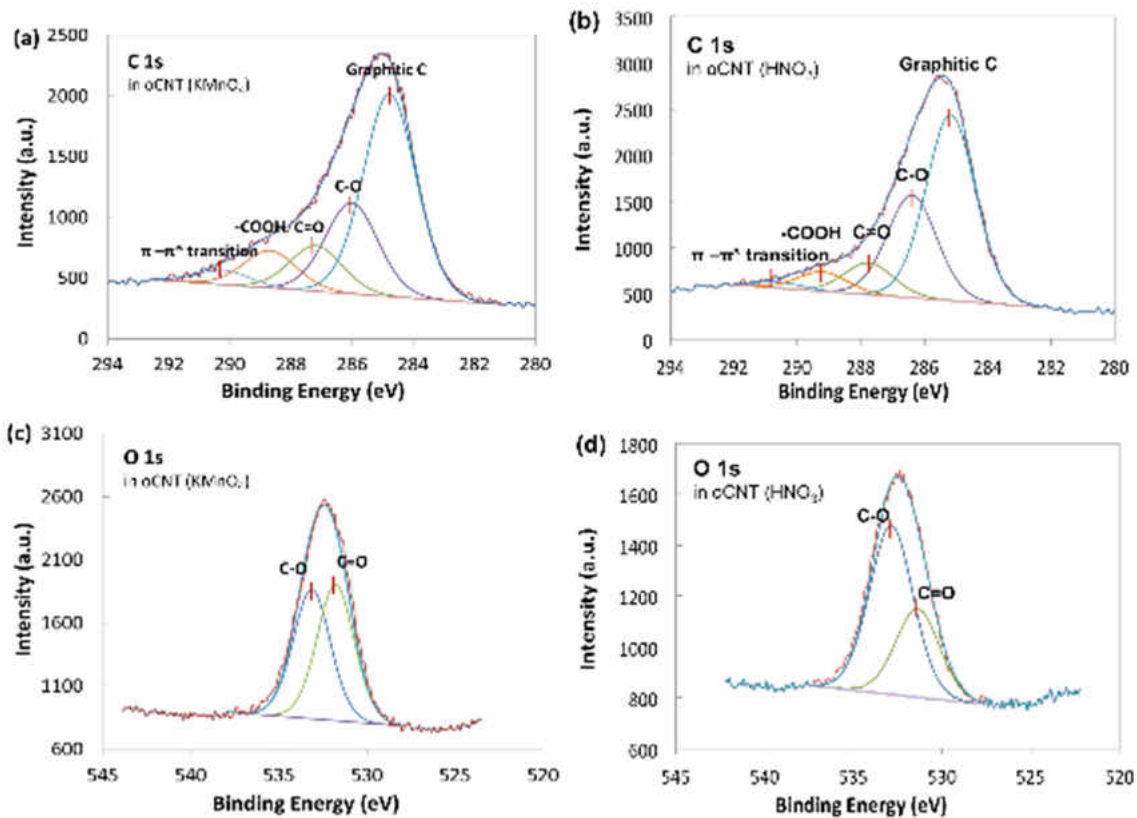
Figure 7.1 XPS spectra of high resolution C 1s in (a) oCNTs (KMnO$_4$); (b) oCNTs (HNO$_3$); O 1s in (c) oCNTs (KMnO$_4$); (d) oCNTs (HNO$_3$).
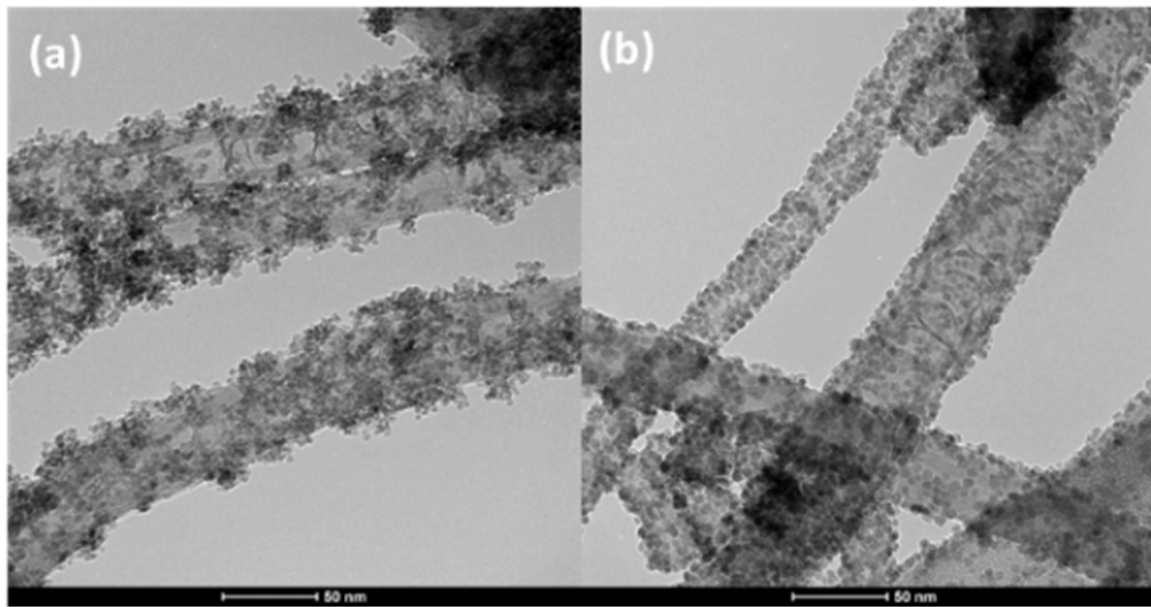
Figure 7.2 TEM images of (a) Co_3O_4 /oCNT($KMnO_4$); (b) Co_3O_4 /oCNT(HNO_3) with $Co(C_2H_3O_2)_2 \cdot 4H_2O$ to oCNT weight ratio of 15:1.

in **Fig. 7.2a** exhibited dendrite crystallization, forming islands among particles with a significant amount of uncovered CNT surface area. However, the batch oxidized by HNO_3 shown in **Fig. 7.2b** resulted in a single layer coverage with a homogeneous particle distribution, indicating that with the similar defect sites on the CNT surface oxidizing by nitric acid may introduce more efficient anchoring sites for metal oxides, with less corrosion to the CNT surface. This would be further elaborated on during discussion of the oxide-support bridging mechanism in **Section 3.3**.

7.2.2 X-ray Diffraction (XRD)

XRD was used to understand the crystal structure and structural transformations of synthesized cobalt oxide catalysts before and after NH_3 treatment (**Fig. 7.3**). The five major characteristic peaks of the well-defined face-centered cubic Co_3O_4 (red) appeared at 2θ values of 31.27, 36.85, 44.81, 59.36 and 65.24°, which correspond to the (220), (311), (400), (511) and (440) reflections (JCPDS 43-1003, red triangles), respectively [136]. Two peaks appeared at 26.2° and 43.2°, indicated with black squares, corresponding to the (002) and (100) planes of the MWCNTs, respectively [218,219]. After NH_3 treatment (blue pattern), the Co_3O_4 character decreased with the disappearance of the (511) and (440) peaks and a slight shift of the two major peaks at 36.85, 44.81° to lower 2θ values, which are closer to the (101) and (110) facets of the CoO phase at 36.62 and 42.36° (JCPDS 65-5474, blue dots) [141]. However, it is unlikely that there was a complete phase transition to CoO because the two primary CoO peaks corresponding to the (200) and (112) reflections did not emerge. Therefore, the oxide is likely an amalgam of one Co (III) and two Co (II) states, which was explored by X-ray Photoelectron Spectroscopy.

7.2.3 X-ray Photoelectron Spectroscopy (XPS)

The C 1s high-resolution spectra for the as-oxidized CNTs, Co_3O_4/oCNT and NH_3 treated Co_3O_4/oCNT samples are shown in **Figs. 7.4a-c**. The C spectrum for the oxidized CNTs (**Fig. 7.4a**) was deconvoluted into 5 bands, corresponding to (from low to high binding energy): graphitic carbon (284.5 eV), carbon singly bound to oxygen (286.1 eV) in phenols and ethers like C-O, carbon doubly bound to oxygen (287.5 eV) in ketones and quinones, carbon bound to two oxygens (288.3 eV) in carboxyls, carboxylic anhydrides, and esters (i.e., -COO), and the π-π*transition (290.1 eV), respectively. The surface C associated with O was 46.3%, and graphitic carbon was still the primary component. After growing Co_3O_4 along the oCNT surface, the percentage of C associated with O increased from 46.3% to 62.9% (**Fig. 7.4b**) and no additional C-metal bonds appeared, suggesting that the anchoring bridges for the metal intermediates were oxygen functional groups. The increase of -C=O and -COO- (**Table 7.1**) during Co deposition may exclude the possibility of growing metal oxides by breaking double bonds between C and O. One possible explanation is that single bond oxygen functional groups, such as phenols, -C-O-, provided the anchoring sites [213][220] for cobalt deposition. A schematic for this possible mechanism is shown in **Fig. 7.5**. With a phenol group on the oxidized CNT, it is possible that the oxygen in the phenol group would attract the Co^{3+} ion from the intermediate species – CoOOH in alkaline media by giving up a proton. The Co^{3+} ion then donates electrons to the oxygen ion in the phenol group by breaking up the double bond with the oxygen ion in CoOOH, converting to Co^{4+} by further releasing the bond with the hydroxide group, which can form water molecule with the proton from the phenol group. The breaking of the double bond in CoOOH can possibility form an

intermediate metastable hexagonal ring during the growth of cobalt oxides on oCNTs. Thus, much more oxygen ions would be singly bound to the carbons in oCNTs during the hydrothermal reaction, and further increase their possibility to be oxidized to -C=O bonds. This proposed mechanism helps understand the significant increase of the portion of -C-O- and -C=O bonds after introducing cobalt oxide onto oCNTs in this work. After post-treatment with NH_3, the portion of both single and double bonds decreased significantly (**Fig. 7.4c**).

The deconvolution of the Co 2p spectrum in Co_3O_4/oCNT resulted in two doublets, with the two main peaks corresponding to Co 2p 3/2 in Co_3O_4 at 779.95 eV and Co 2p 1/2 in Co_3O_4 at 795.78 eV, respectively. The satellite doublets with binding energy ca. 6 eV higher than the major peaks are the characteristic satellites of Co^{2+} in CoO, since Co_3O_4 is actually a mixture of Co^{3+} and Co^{2+} and the binding energy of the Co^{2+} in CoO and Co_3O_4 are too close to separate. Therefore, the increase of the satellite doublets from 19.2% to 29.0% suggest more reduced CoO in the catalyst, which agrees well with the XRD results.
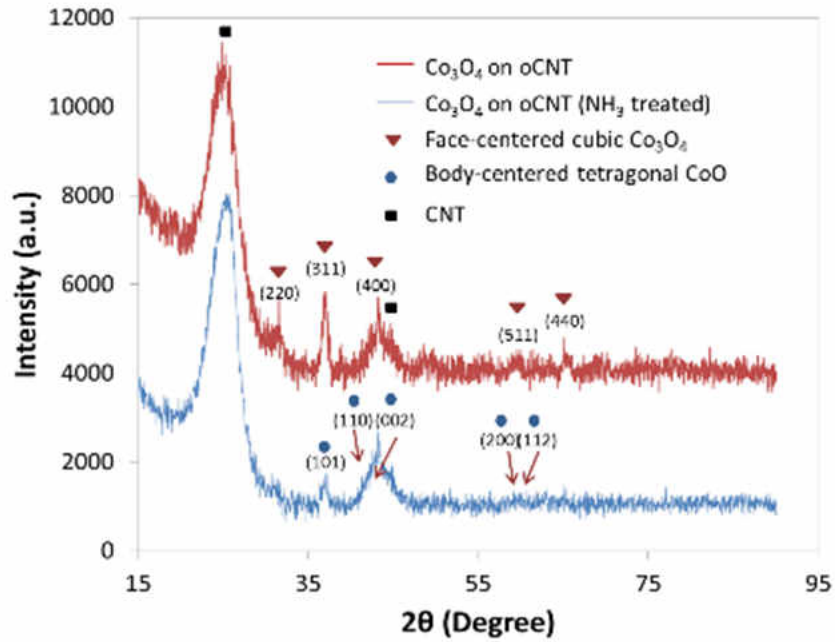
Figure 7.3 XRD patterns of Co$_3$O$_4$/oCNT (red) and NH$_3$ treated Co$_3$O$_4$/oCNT (blue)
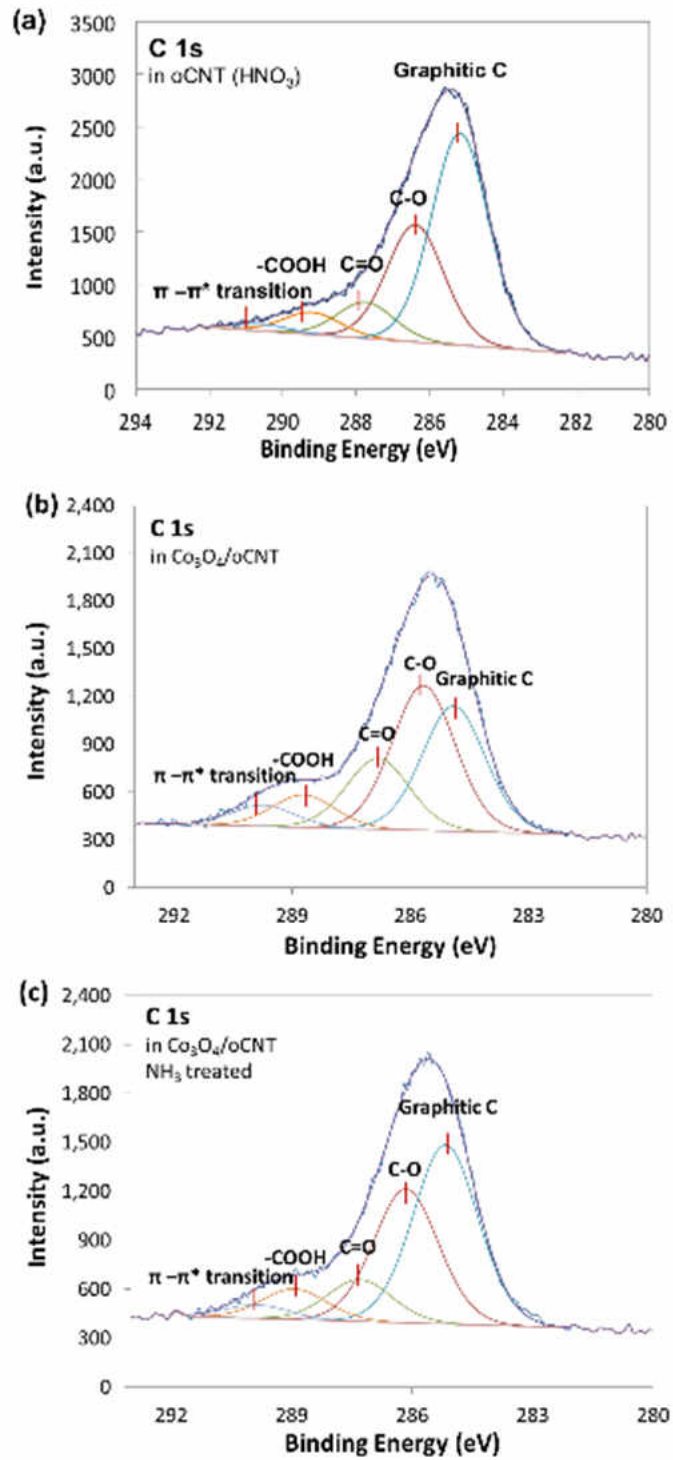
Figure 7.4 XPS spectra of high resolution C 1s in (a) oCNT; (b) Co_3O_4 /oCNT; (c) NH_3 treated Co_3O_4 /oCNT.

Table 7.1 Relative Content of Functional Groups Determined by C 1s High-Resolution XPS Spectra.

Samples	Relative atomic concentrations (%)			
	Graphitic C	-C-O-	-C=O	-COO-
as-oxidized CNT	54.7	30.2	9.35	5.7
Co_3O_4 /oCNT	33.5	38.8	19.0	8.7
NH_3 treated Co_3O_4 /oCNT	45.1	37.3	10.9	6.7
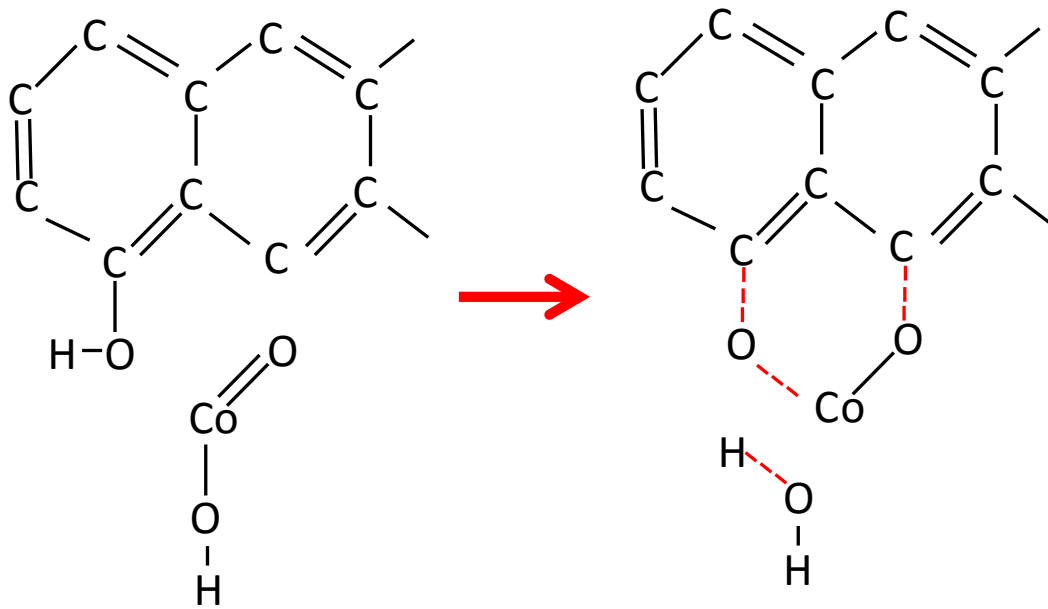
Figure 7.5 Proposed mechanism for Co_3O_4 growth mechanism on oCNTs.

7.2.4 Fourier Transform Infrared Spectroscopy (FTIR)

The FTIR spectra of the oxidized CNTs, Co_3O_4/oCNT and NH_3 treated Co_3O_4/oCNT are shown in **Fig. 7.6**. The oxidized CNTs (purple) showed two absorption peaks at intermediate frequencies between 1600 cm^{-1} and 1100 cm^{-1}, which belong to C=O, C=C and C=N bending from 1500 to 2000 cm^{-1}, and C-O, C-C and C-N bending from 1000 to 1500 cm^{-1}, respectively [221–223]. This indicated the introduction of oxygen functional groups onto the CNTs after being oxidized with concentrated HNO_3. The peaks between 1600 cm^{-1} and 1100 cm^{-1} became more profound when cobalt oxides were introduced to the CNTs (blue and green), which may be due to the bond formation between the oxygen or hydroxide groups in the cobalt intermediate and the non-functionalized graphitic C after the metal ions were attracted by the anchoring oxygen bridges. Vibrations corresponding to the metal oxide were observed as absorption peaks at wavenumbers below 800 cm^{-1}. After NH_3 treatment, the single and double bonds between oxygen and carbon decreased significantly (orange), similar to the as-oxidized CNTs. The peak representing the metal oxide below 800 cm^{-1} remained in the spectrum. The increase and decrease trends of the oxygen functional groups after depositing Co_3O_4 onto oCNTs and the ammonia reduction step agreed well with the XPS results.

7.2.5 Transmission Electron Microscopy (TEM)

Figures 7.7a and **7.7b** show the morphology of Co_3O_4/oCNT with an optimized cobalt precursor to oCNT weight ratio of 5:3, before and after ammonia treatment, respectively. Smaller particles with irregular oxide grains (ca. 1-4 nm in diameter) aggregated at specific areas along the tubes with a significant portion of the oCNT surface exposed before ammonia treatment. After treating the catalysts with NH_3 at low

123

temperature (**Fig. 7.7b**), bundles of small particles grew larger (between 20 and 50 nm) with blunt edges, and much cleaner CNTs were achieved afterwards. High-resolution TEM (HRTEM) images in **Fig. 7.7c** clearly confirmed the hybrid structure of a single Co_3O_4 particle supported on CNT from the ammonia treated sample in **Fig. 7.7b**. Part of the Co_3O_4 particle was imbedded into the CNT even after heat treatment and a strong sonication, suggesting a strong interaction between CNT and Co_3O_4 particles. The largely exposed lattice with a d-spacing of 0.47 nm indicated the high percentage of the (111) facet on the Co_3O_4 crystal surface. According the structure shown in **Fig. 1.6**, the (111) facet possesses higher density of Co^{2+}. Together with the XRD and XPS analysis from previous sections, the percentage of Co^{2+} increased in both the bulk and surface of the Co_3O_4 particles after NH_3 treatment. Catalysts synthesized with different cobalt precursor to oCNT weight ratios and based on different oxidation degree of oCNTs were also compared. A higher ratio (15:1) resulted in Co_3O_4 grains being fully packed along the oCNTs without exposing any bare oCNT surface area. The larger single particles were cubic with side lengths of less than 10 nm. However, if only the degree of CNT oxidation was lowered (0.5 h with concentrated HNO_3), the morphology of the single particles was slightly changed, and the particle distribution was more sparse along the CNTs.
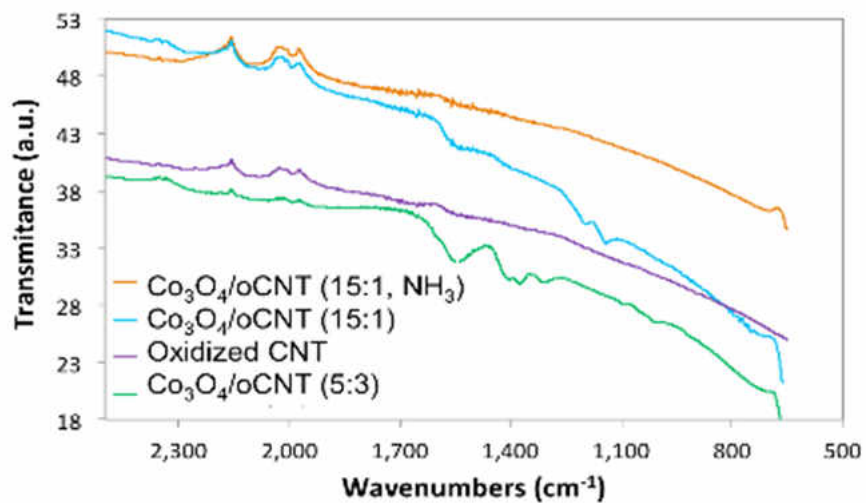
Figure 7.6 FTIR spectra of oxidized CNT (purple); Co_3O_4 /oCNT ($Co(C_2H_3O_2)_2 \cdot 4$ H_2O:oCNT=15:1) (green); Co_3O_4 /oCNT ($Co(C_2H_3O_2)_2 \cdot 4H_2O$:oCNT=5:3) (blue); NH_3 treated Co_3O_4 /oCNT ($Co(C_2H_3O_2)_2 \cdot 4H_2O$: oCNT=5:3) (orange).
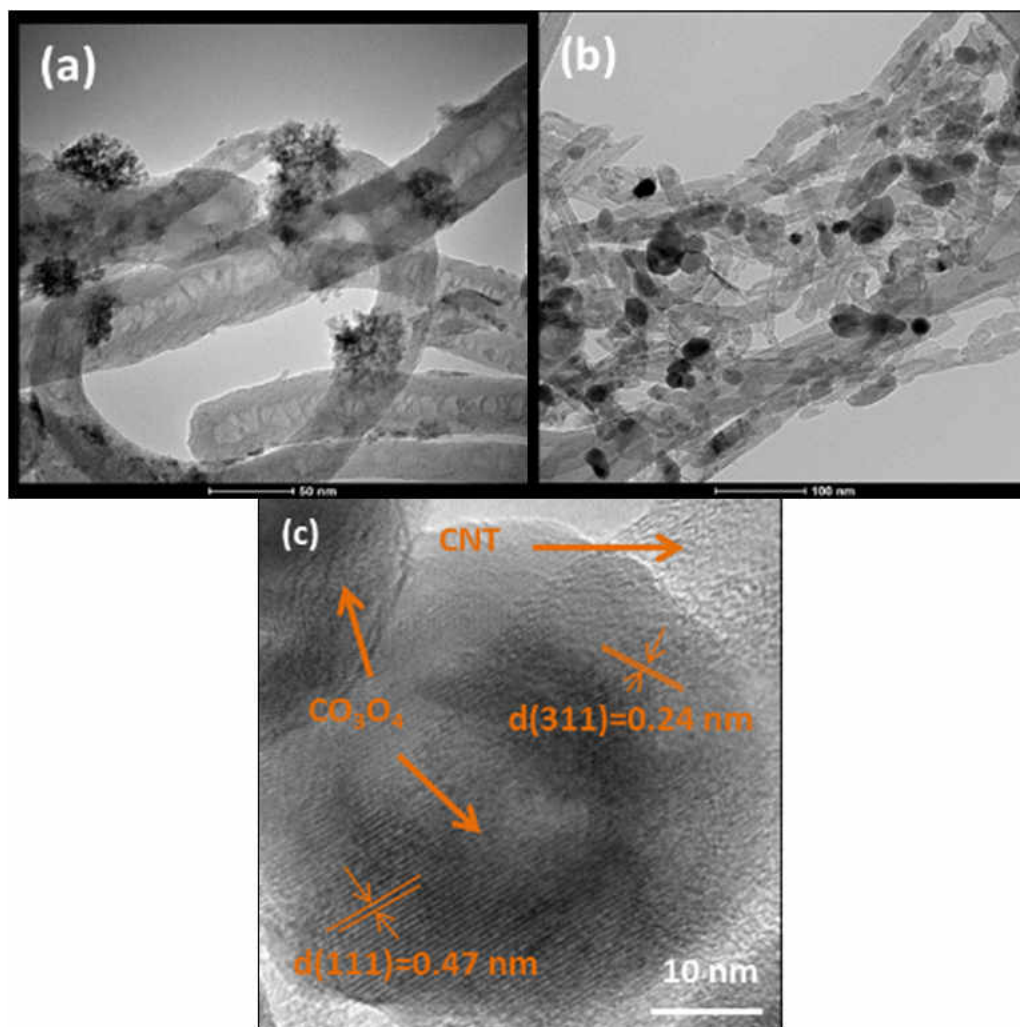
Figure 7.7 TEM images of Co₃O₄/oCNT (a) before ammonia treatment; (b) after ammonia treatment (with $Co(C_2H_3O_2)_2\cdot4H_2O$ to oCNT weight ratio of 5:3 for both (a) and (b)); (c) high-resolution TEM of image 7.7b

7.2.6 Electrochemical Characterization

The ORR/OER activities of Co_3O_4/oCNT samples with the various synthesis parameters discussed in **Section 7.2.5** are compared. The sample presenting the best combination of activity and durability (discussed below) possessed the morphology and distribution shown in **Fig. 7.7b** (with fuming HNO_3 oxidizing for 1 h, metal precursor to oCNT weight ratio of 5:3 and additional ammonia reduction step). The ORR polarization curve of this top-performing Co_3O_4/oCNT was compared with commercial 50 wt% Pt/C (TEC10E50E, Tanaka) (**Fig. 7.8a**), with the same total catalyst loading, in O_2-saturated 0.1 M KOH electrolyte. Both the ORR onset and half-wave potential of NH_3 treated Co_3O_4/oCNT were only about 0.1 V negative of commercial Pt/C. In addition, the OER onset potential, 1.48 V, was only 0.05 V higher than that of commercial iridium black (**Fig. 7.8b**), equaling the best-known Co_3O_4-based hybrid OER catalysts [141]. The ORR/OER activities were much improved over the starting N-CNT material shown in **Fig. 7.8c**. The excellent bifunctional activity demonstrated by the Co_3O_4/oCNT catalyst is among the highest when compared to the literature [78][136][141].

Koutecky−Levich plots from the ORR polarization curves at different electrode rotation rates for both NH_3 treated Co_3O_4/oCNT and commercial Pt/C are shown in **Fig. 7.8d**. From 0.5 V to 0.75V, linear Koutecky−Levich plots of NH_3 treated Co_3O_4/oCNT and Pt/C black were obtained (assuming first order kinetics), by plotting J^{-1} *vs.* $\omega^{-1/2}$ [200]. From **Eqns. 7.1** and **7.2**, the slopes ($1/B$) of the Koutecky-Levich plots at different potentials yield the average number of electrons transferred, n, involved in the ORR in alkaline media.

$$1/J = 1/J_k + 1/J_{diff} = 1/J_k + 1/(B\omega^{\frac{1}{2}}) \qquad (7.1)$$

$$B = 0.62nFC_0D_0^{2/3}\eta^{-1/6} \tag{7.2}$$

where J_k and J_{diff} are the kinetic and diffusion limited current densities respectively, F is the Faraday constant, C_0 is the saturated concentration of O_2 in the 0.1 M KOH electrolyte (1.21×10^{-3} mol/L), D_0 is the diffusion coefficient of O_2 in the KOH electrolyte (1.86×10^{-5} cm^2 s), and η is the viscosity of the electrolyte (1.008×10^{-2} cm^2 s) [200]. Over the entire potential range, it was found that for NH$_3$ treated Co$_3$O$_4$/oCNT, $n \approx 4$ (on average) and for Pt/C, $n \approx 3.6$, close to reported literature values [199][224,225]. The lower electron transfer number of Pt/C could be linked to its higher degree of 2-electron ORR in alkaline media to produce peroxide-like intermediates when compared with NH$_3$ treated Co$_3$O$_4$/oCNT.

Catalyst durability tests were first conducted on raw and oxidized CNTs. The ORR activity was significantly compromised after only 500 cycles at scan rate of 500 mV/s in O$_2$-saturated 0.1 M KOH electrolyte, which showed that the ammonia reduction step was necessary to restore structural and chemical stability to the CNTs. The stability of NH$_3$ treated Co$_3$O$_4$/oCNT was investigated over 2000 cycles, from 0-1.9 V, at scan rate of 500 mV/s. The intermediate polarization curves were collected at 1600 rpm, 20 mV/s (**Fig. 7.8e**), demonstrating no significant change for both activities even after 2000 cycles in this harsh oxidizing environment. A new redox couple appeared during cycling (**Fig. 7.8f**), which verified the existence of cobalt oxide [226]. However, for the catalysts without any post NH$_3$ treatment, the ORR activity was nearly absent within the first 50 cycles. Therefore, the NH$_3$ reduction plays a critical role in the stabilization of the surface metal oxide and improvement of the CNT support's durability.

7.3 Summary

A highly stable, ORR/OER active, bifunctional, CNT-based hybrid catalyst for reversible alkaline fuel cells was obtained at the bench scale. For the first time, a carbon based hybrid material demonstrated significant durability over a large potential range from 0 to 1.9 V for 2000 cycles. This study examined the impact of the synthesis approach, oxidation agent, metal oxide anchoring bridges, particle morphology, and metal oxidation states to functional groups reduction in order to provide an optimization pathway and new insights for next generation catalyst design. Future work will focus on optimizing parameters in the procedure, such as oxidizing conditions, precursor substitution, CNT size, post-treatment, etc. Eventually, the novel materials will be scaled up to test in unitized regenerative fuel cells.
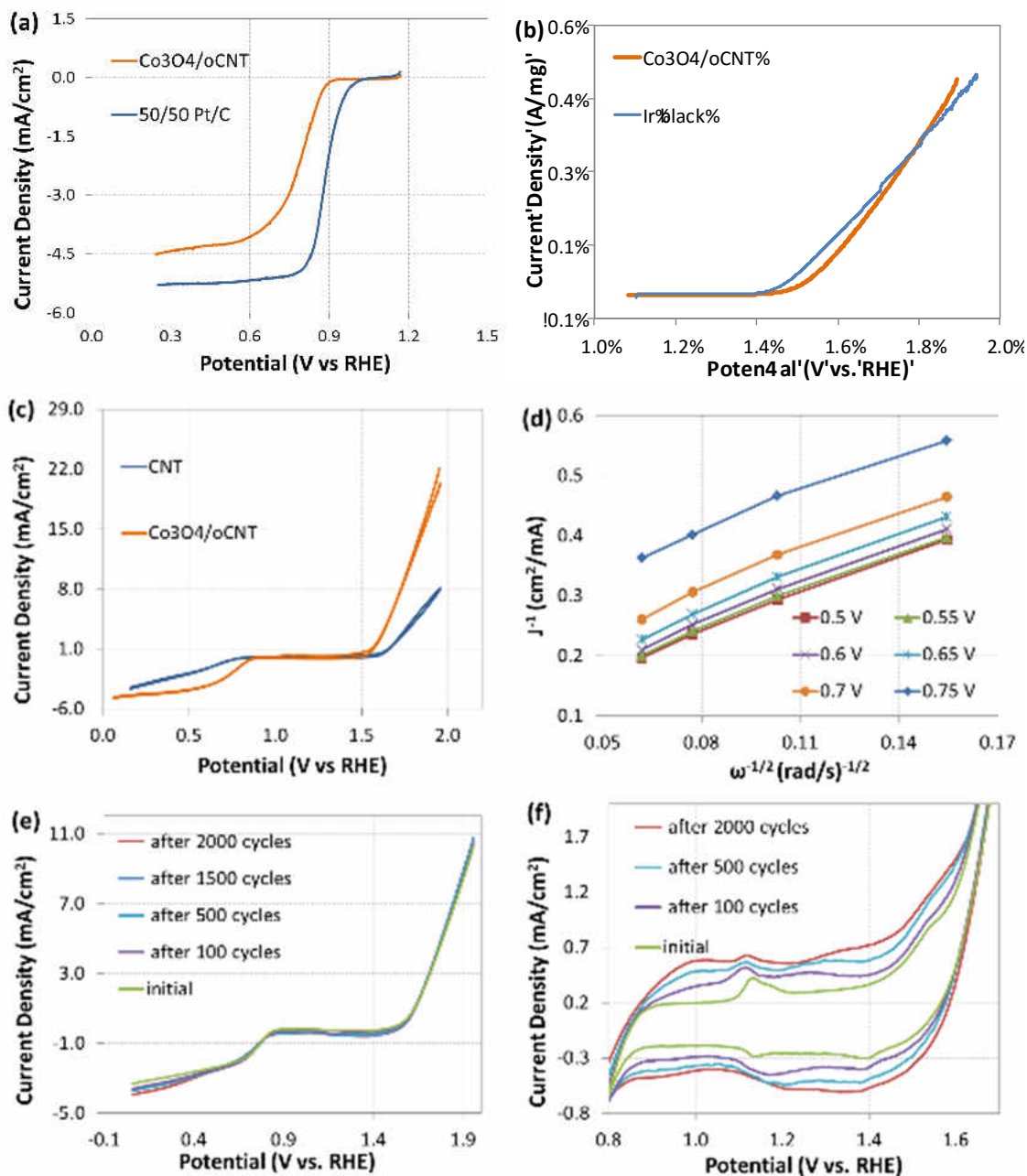
Figure 7.8 (a) ORR polarization curve of NH_3 treated Co_3O_4/oCNT compared with that of commercial Pt/C; (b) OER polarization curve of NH3 treated Co_3O_4/oCNT compared with that of commercial Ir black; (c) OER/ORR polarization curve of NH_3 treated Co_3O_4/oCNT compared with that of commercial raw N-CNT; (d) Koutecky−Levich plots of NH_3 treated Co_3O_4/oCNT from 0.5 V to 0.75V; (e) durability test of NH_3 treated Co_3O_4/oCNT for 2000 cycles; (f) zoom-in plot from 0.8 to 1.6 V of Fig. 7.7e.

130

CHAPTER 8 - CONCLUSIONS AND FUTURE WORK

8.1 Conclusions

This study discussed the function of transition metal oxides in electrochemical catalysis for reactions, with a primary focus on oxygen reduction and evolution, in devices such as PEMFCs, PEMECs, AFCs and alkaline URFCs. The former part of this work investigated metal oxide candidates as support materials for precious metal catalyst such as Pt and Ir/IrO$_2$ in both acidic and alkaline media. Metal oxide modification by elemental doping was thoroughly explored in the sol-gel route of Ti/WO$_3$ and Ti/WC synthesis through physical characterizations including in-situ XRD and FESEM with FIB for in-situ sample preparation. The lattice structure and parameters and thermodynamic limits for stability of various phases should be referred to as two basic requirements for the formation of solid solution [227][228]. The opposite tendency of the 8 at% and 16 at% of titanium in WO$_3$ for acidic methanol oxidation activity and durability indicated the appearance of a metallic Ti phase at higher doping percentage accounting for higher conductivity and activity, but no stability enhancement. The failure of forming titanium-doped tungsten carbide was attributed segregation of the titanium and tungsten oxides at high temperatures and the difference of lattice structures and sizes of the two carbides.

The study of the durability of Ir/W/TiO$_2$ exhibited different performance in RDE and electrolyzer. For the batch with lower Ir loading (30 %), the supported catalyst showed nearly zero OER activity degradation in RDE; however, the catalyst could not survive even the first 24 hours of electrolyzer operation, indicating the importance of

catalyst screening and analysis in scale-up application, although there may be other component degradation including membrane poisoning or hardware contamination. The agglomeration of the iridium particles and increase in the exposed area of the support materials were detected through TEM. However, with higher loading than 70 % of iridium, the durability was much improved, with only a slight initial morphology change in the first 24 hours, and then stabilized after that, because less support material was exposed. This suggests that the support itself may be at least somewhat unstable in OER-relevant conditions. Therefore, an intermediate loading is worth investigating in the future.

For the Pt/ITO, which had an extremely steady performance in acidic ORR shown in previous study, its functionality and surface phase change were further explored in alkaline electrolyte. 5% ITO was prepared as the support material for monolayer Pt and the mass activity and specific activity of Pt/ITO were nearly 2.5 times that of Pt/Vulcan in alkaline media, respectively. Its stability was also greater than that of Pt/Vulcan after a 300-cycle stability test between -0.2-0.4V in O_2-saturated alkaline electrolyte. The ECSA loss in Pt/ITO was less than half of that in Pt/Vulcan. During this long-term potentiometric cycling, a progressively reduced Sn^{2+} species was observed on the surface, from 9% at the beginning of life to 87% at the end of life. Further investigation into the Pt-support interaction is recommended to understand the mechanism for the ORR in alkaline media in order to purposefully utilize Pt-support interactions in future catalysts. The latter part of this work used metal oxides as direct reversible ORR/OER catalyst in alkaline media, which were supported on CNTs. For the first time, a CNT based hybrid material demonstrated significant durability over a large potential range from 0 to 1.9 V.

The oxidizing agent, metal oxide anchoring bridges, particle morphology, metal oxidation states, and functional group reduction in the synthesis approach were discussed with regards to their impact on the electrochemical stability. It was concluded that metal oxide growth on the functionalized CNT prefer oxygen sites in a single bond between carbon and oxygen by introducing different ratio of functional groups on the CNTs. The fundamental discussion in this work provides design principles for novel advanced carbon-based catalysts for electrocatalysis.

8.2 Future Work

Future work can be focused on a few directions based on the work above: first is to understand the doping density quantitatively and its influence on oxygen electrocatalysis with new methods and models, such as Mott-Schottky (MS) analysis. Take Ti/WO_3 as an example: besides temperature, future work can extend the doping range to study the phase segregation on the doping percentage dimension in Ti/WO_3 and experimentally understand the doping effect on activity and durability of WO_3 through the doping density analyzed by MS plot. MS analysis can be used to describe a three-phase system: the Ti/WO_3 support, the Pt catalyst and the electrolyte, particularly in this case, to understand the unique value of the Fermi level and redox potential for the three-phase system at equilibration [229]. Acquisition of Mott-Schottky plots (inverse square of space charge layer capacitance, C_{sc}^{-2}, versus electrode potential E, as shown in **Equation 8.1** is a normal way for semiconductor materials electrochemical characterization [230][231,232]:

$$(C_{sc})^{-2} = 2(E - E_{fb} - kT/e) / N_D \varepsilon \varepsilon_0 e A^2 \qquad (8.1)$$

where N_D is the doping density, E_{fb} – flatband potential, k, the Boltzmann constant, T, the

temperature, ε, the relative dielectric constant of the anodic film, ε_0, the permittivity of free space, e, the charge of an electron and A, the electrode surface. Mott-Schottky plot yields the doping density through the slope of the straight line and flatband potential by the intercept. Experimental data can be obtained by potentiodynamic electrochemical impedance spectroscopy at various frequencies from 0 to 0.6 V; the data can be fitted into equivalent electric circuit (EEC) models and the parameters can provide the space charge layer capacitance vs. the electrode potential.

The second area for additional work is the fundamental understanding of the active sites for reversible ORR/OER catalysts. Defining the active sites for both ORR and OER on mixed valence metal oxides by systematic experimental confirmation is always desirable and necessary. Take Co_3O_4 for example; it is well agreed that the active site for OER is the Co^{4+} oxidized from Co^{3+} in the aqueous solution, though the ORR active sites remain controversial. Different morphologies of Co_3O_4 powders alone, with no support materials in order to rule out additional factors, can be synthesized with different exposure of major facets, and after quantitative characterization the ORR and OER activity can be examined together on these materials. Asynchronized activity increase for both reactions should be expected since opposite bonding energies are desired in the RDS for either reaction. Another mysterious issue about active sites is with the hybrid structure. A significant amount of literature has agreed on the ORR active sites of M-N-C for a lower metal loading, but hybrid materials with relatively high loading of metal oxides still have not exhibited any clear evidence for the function of N doping or the Schottky junction [196]. Therefore, accurate control experiments are needed in the system for further investigations.

Last, but not least, in terms of the durability of catalyst, which is the ultimate target for electrochemical device commercialization, it is important to understand the in-situ phase transition, electronic structure modification, such as the d-band center or fermi level changing, which can be realized by creating an in-situ FTIR and conductivity test in the RDE electrochemical test, as shown in **Fig. 8.1**. The through-plane conductivity measurements for both the hybrid Co_3O_4/oCNT catalyst for reversible ORR/OER and the Pt/ITO catalyst for ORR can be realized by using Au/Ti/quartz interdigitated array (IDA) electrodes [226] (CH instruments, 2 μm electrode width, 2 μm gap, 2 mm length, 65 pairs). The conductivity of the catalyst layer shown on the right Y axis in the left image of **Fig. 8.1**, σ_{eff}, can be calculated from the equation in image **Fig. 8.1**, where I_{cond} is the through-film conductivity current (calculated below in **Equations 8.2-8.6**), w is the IDA gap spacing (2 μm), N is the number of electrodes (130), d is the film thickness, and ΔV is the voltage offset between working electrode 1 (WE1) and working electrode 2 (WE2)**:**

$$I_{WE1} = I_{OER1} + I_{cat1} + I_{cond} \tag{8.2}$$

$$I_{WE2} = I_{OER2} + I_{cat2} - I_{cond} \tag{8.3}$$

$$I_{OER2} \approx I_{OER1} \tag{8.4}$$

$$I_{cat1} \approx I_{cat2} \tag{8.5}$$

$$I_{WE1} - I_{WE2} \approx 2I_{cond} \tag{8.6}$$

The in-situ measured catalyst conductivity can help analyze the contact status between the CNT and supported metal oxide. To further improve the ORR/OER reversibility and durability of the hybrid catalyst, raw CNTs with different wall thicknesses, lengths, functional groups and reduction degree should be screened systematically. The same can be done for the raw, unsupported metal oxides. Then, the

improved properties of the hybrid structure could be compared accordingly.

On the other hand, the MS analysis model can be applied to ITO system to in-situ determine the doping density change during durability cycling in-situ, along with ITO surface oxidation state change from XPS. This would allow one to determine catalyst properties at different reaction stages where the intermediate status can be deliberately synthesized. In terms of the ORR enhancement mechanism, there have been controversial proposals about the Sn^{4+} and Sn^{2+} states' function in the interaction with the supported Pt. A previous study [154] concluded that in acidic electrolyte, surface Sn^{4+} is helpful for the orientation of Pt in the {111} facet, which is agreed to be the most active facet for ORR that can be realized with high concentration. However, in this work, it is most likely that the progressively increased surface Sn^{2+} ions have a synergistic effect with Pt since with 87% of Sn^{2+} on the surface the specific activity only dropped 10% but the ECSA dropped 17.4% [225].

Therefore, using new microscopic in-situ experimental setups, such as in-situ FTIR and the interdigitated electrode array for in-situ conductivity test, a new model for data analysis like the MS plot and systematic experimental design for intermediate phase characterizations can be realized in future work. Using these tools, more experimental evidence can be gained to generate a comprehensive theoretical hypothesis about the influence of metal-support interactions (such as electronic modification and elemental doping effect) on the active sites for ORR/OER on mixed valence metal oxide surfaces, as well as the stability of the bonding between catalyst and support materials. This new understanding would further provide guidance for catalyst modification and novel catalyst design from a broader perspective.
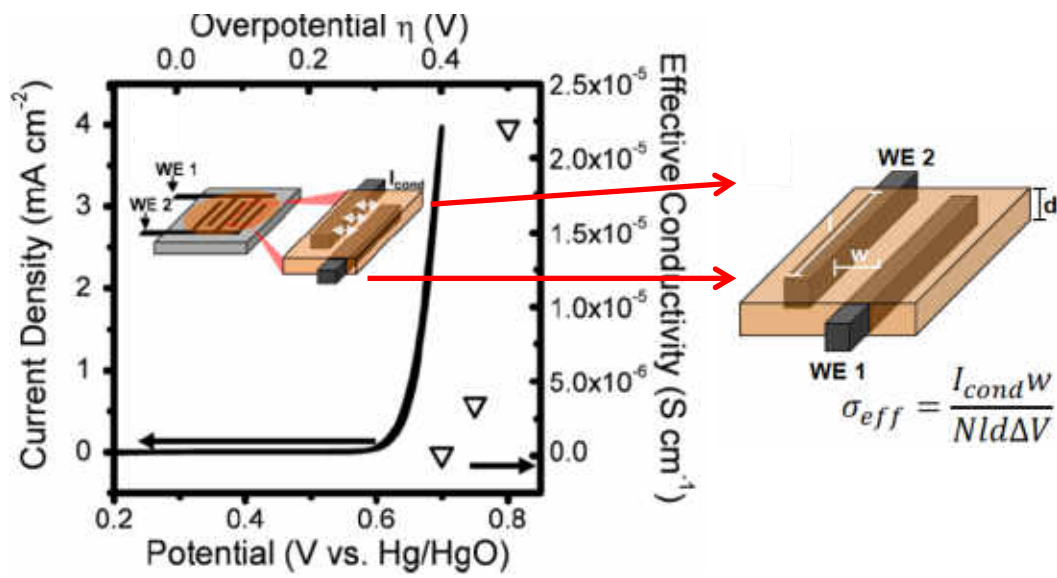
Figure 8.1 Schematic of electrodes and conductivity calculation [226].

References:

[1] W. Yao, J. Yang, J. Wang, Y. Nuli, Chemical deposition of platinum nanoparticles on iridium oxide for oxygen electrode of unitized regenerative fuel cell, Electrochem. Commun. 9 (2007) 1029–1034.

[2] Y. Zhang, H. Zhang, Y. Ma, J. Cheng, H. Zhong, S. Song, et al., A novel bifunctional electrocatalyst for unitized regenerative fuel cell, J. Power Sources. 195 (2010) 142–145.

[3] H. Dau, C. Limberg, T. Reier, M. Risch, S. Roggan, P. Strasser, The mechanism of water oxidation: from electrolysis via homogeneous to biological catalysis, ChemCatChem. 2 (2010) 724–761.

[4] H.A. Gasteiger, S.S. Kocha, B. Sompalli, F.T. Wagner, Activity benchmarks and requirements for Pt, Pt-alloy, and non-Pt oxygen reduction catalysts for PEMFCs, Appl. Catal. B Environ. 56 (2005) 9–35.

[5] H.A. Gasteiger, W. Gu, R. Makharia, M.F. Mathias, B. Sompalli, Beginning-of-life MEA performance—efficiency loss contributions, Handb. Fuel Cells. (2003).

[6] J.A. Keith, G. Jerkiewicz, T. Jacob, Theoretical investigations of the oxygen reduction reaction on Pt (111), ChemPhysChem. 11 (2010) 2779–2794.

[7] J.K. Nørskov, J. Rossmeisl, A. Logadottir, L. Lindqvist, J.R. Kitchin, T. Bligaard, et al., Origin of the overpotential for oxygen reduction at a fuel-cell cathode, J. Phys. Chem. B. 108 (2004) 17886–17892.

[8] Y. Okamoto, O. Sugino, Hyper-Volcano Surface for Oxygen Reduction Reactions over Noble Metals, J. Phys. Chem. C. 114 (2010) 4473–4478.

[9] M. Shao, P. Liu, J. Zhang, R. Adzic, Origin of enhanced activity in palladium alloy electrocatalysts for oxygen reduction reaction, J. Phys. Chem. B. 111 (2007) 6772–6775.

[10] V. Stamenkovic, B.S. Mun, K.J.J. Mayrhofer, P.N. Ross, N.M. Markovic, J. Rossmeisl, et al., Changing the activity of electrocatalysts for oxygen reduction by tuning the surface electronic structure, Angew. Chemie. 118 (2006) 2963–2967.

[11] N. US Department of Commerce, Energy Storage & Delivery, (n.d.). http://www.nist.gov/mml/msed/functional_polymer/fuelcell.cfm.

[12] R. Tunold, A.T. Marshall, E. Rasten, M. Tsypkin, L.-E. Owe, S. Sunde, Materials for electrocatalysis of oxygen evolution process in PEM water electrolysis cells, ECS Trans. 25 (2010) 103–117.

[13] E. Connor, Performance of Palladium Diffusers for Reliable Purification of Hydrogen, (2015). http://www.peakscientific.com/articles/performance-of-palladium-diffusers-for-reliable-purification-of-hydrogen/.

[14] J. Rossmeisl, A. Logadottir, J.K. Nørskov, Electrolysis of water on (oxidized) metal surfaces, Chem. Phys. 319 (2005) 178–184.

[15] J. Rossmeisl, Z.-W. Qu, H. Zhu, G.-J. Kroes, J.K. Nørskov, Electrolysis of water on oxide surfaces, J. Electroanal. Chem. 607 (2007) 83–89.

[16] H.A. Hansen, I.C. Man, F. Studt, F. Abild-Pedersen, T. Bligaard, J. Rossmeisl, Electrochemical chlorine evolution at rutile oxide (110) surfaces, Phys. Chem. Chem. Phys. 12 (2010) 283–290.

[17] I.C. Man, H.Y. Su, F. Calle-Vallejo, H.A. Hansen, J.I. Martínez, N.G. Inoglu, et al., Universality in Oxygen Evolution Electrocatalysis on Oxide Surfaces, ChemCatChem. 3 (2011) 1159–1165.

[18] S.A. Grigoriev, V.I. Porembsky, V.N. Fateev, Pure hydrogen production by PEM electrolysis for hydrogen energy, Int. J. Hydrogen Energy. 31 (2006) 171–175.

[19] S. Trasatti, Electrocatalysis in the anodic evolution of oxygen and chlorine, Electrochim. Acta. 29 (1984) 1503–1512.

[20] Y. Matsumoto, E. Sato, Electrocatalytic properties of transition metal oxides for oxygen evolution reaction, Mater. Chem. Phys. 14 (1986) 397–426.

[21] S.B. Brummer, The use of large anodic galvanostatic transients to evaluate the maximum adsorption on platinum from formic acid solutions, J. Phys. Chem. 69 (1965) 562–571.

[22] K.J.J. Mayrhofer, D. Strmcnik, B.B. Blizanac, V. Stamenkovic, M. Arenz, N.M. Markovic, Measurement of oxygen reduction activities via the rotating disc electrode method: From Pt model surfaces to carbon-supported high surface area catalysts, Electrochim. Acta. 53 (2008) 3181–3188.

[23] G.F. McLean, T. Niet, S. Prince-Richard, N. Djilali, An assessment of alkaline fuel cell technology, Int. J. Hydrogen Energy. 27 (2002) 507–526.

[24] R.S. Jayashree, L. Gancs, E.R. Choban, A. Primak, D. Natarajan, L.J. Markoski, et al., Air-Breathing Laminar Flow-Based Microfluidic Fuel Cell, J. Am. Chem. Soc. 127 (2005) 16758–16759.

[25] J.R. Varcoe, R.C.T. Slade, An electron-beam-grafted ETFE alkaline anion-exchange membrane in metal-cation-free solid-state alkaline fuel cells, Electrochem. Commun. 8 (2006) 839–843.

[26] J.R. Varcoe, P. Atanassov, D.R. Dekel, A.M. Herring, M.A. Hickner, P.A. Kohl, et al., Anion-exchange membranes in electrochemical energy systems, Energy Environ. Sci. 7 (2014) 3135–3191.

[27] K. Ota, S. Mitsushima, O2 reduction on the Pt/polymerelectrolyte interface, Handb. Fuel Cells. (2010).

[28] F. Cheng, J. Shen, B. Peng, Y. Pan, Z. Tao, J. Chen, Rapid room-temperature synthesis of nanocrystalline spinels as oxygen reduction and evolution electrocatalysts., Nat. Chem. 3 (2011) 79–84.

[29] I. Roche, E. Chaînet, M. Chatenet, J. Vondrák, Carbon-supported manganese oxide nanoparticles as electrocatalysts for the oxygen reduction reaction (ORR) in alkaline medium: physical characterizations and ORR mechanism, J. Phys. Chem. C. 111 (2007) 1434–1443.

[30] B.B. Blizanac, P.N. Ross, N.M. Markovic, Oxygen electroreduction on Ag(1 1 1): The pH effect, Electrochim. Acta. 52 (2007) 2264–2271.

[31] J.O. Bockris, S.S. Penner, J. Robert Selman, D. Shores, E.B. Yeager, J. Appleby, et al., MEMBERS AND EX OFFICIO MEMBERS OF THE DOE ADVANCED FUEL CELL WORKING GROUP (AFCWG), in: S.S.B.T.-A. of R.N. for A.F.C. Penner (Ed.), Pergamon, 1986: pp. vii–viii.

[32]   A.J. Appleby, Electrocatalysis, in: B. Conway, J. Bockris, E. Yeager, S.M. Khan, R. White (Eds.), Compr. Treatise Electrochem. SE - 4, Springer US, 1983: pp. 173–239.

[33]   P.S.D. Brito, C.A.C. Sequeira, Cathodic oxygen reduction on noble metal and carbon electrodes, J. Power Sources. 52 (1994) 1–16.

[34]   J. Xu, W. Huang, R.L. McCreery, Isotope and surface preparation effects on alkaline dioxygen reduction at carbon electrodes, J. Electroanal. Chem. 410 (1996) 235–242.

[35]   I. Morcos, E. Yeager, Kinetic studies of the oxygen—peroxide couple on pyrolytic graphite, Electrochim. Acta. 15 (1970) 953–975.

[36]   V.S. Bagotzky, N.A. Shumilova, G.P. Samoilov, E.I. Khrushcheva, Electrochemical oxygen reduction on nickel electrodes in alkaline solutions—II, Electrochim. Acta. 17 (1972) 1625–1635.

[37]   D.B. Sepa, M. V Vojnovic, A. Damjanovic, Kinetics and mechanism of O_2 reduction at Pt IN alkaline solutions, Electrochim. Acta. 25 (1980) 1491–1496.

[38]   T.J. Schmidt, V. Stamenkovic, M. Arenz, N.M. Markovic, P.N. Ross Jr, Oxygen electrocatalysis in alkaline electrolyte: Pt (< i> hkl</i>), Au (< i> hkl</i>) and the effect of Pd-modification, Electrochim. Acta. 47 (2002) 3765–3776.

[39]   D. Šepa, M. Vojnovic, A. Damjanovic, Oxygen reduction at silver electrodes in alkaline solutions, Electrochim. Acta. 15 (1970) 1355–1366.

[40]   B.B. Blizanac, P.N. Ross, N.M. Markovic, Oxygen Reduction on Silver Low-Index Single-Crystal Surfaces in Alkaline Solution: Rotating Ring DiskAg (h kl) Studies, J. Phys. Chem. B. 110 (2006) 4735–4741.

[41]   M.H. Shao, R.R. Adzic, Spectroscopic identification of the reaction intermediates in oxygen reduction on gold in alkaline solutions, J. Phys. Chem. B. 109 (2005) 16563–16566.

[42]   J.R. Varcoe, R.C.T. Slade, G.L. Wright, Y. Chen, Steady-state dc and impedance investigations of H2/O2 alkaline membrane fuel cells with commercial Pt/C, Ag/C, and Au/C cathodes, J. Phys. Chem. B. 110 (2006) 21041–21049.

[43]   W. Li, H. Hu, N.K. Dutta, High speed all-optical encryption and decryption using quantum dot semiconductor optical amplifiers, J. Mod. Opt. 60 (2013) 1741–1749.

[44]   W. Li, S. Ma, H. Hu, N.K. Dutta, All optical latches using quantum-dot semiconductor optical amplifier, Opt. Commun. 285 (2012) 5138–5143.

[45]   S.L. Gojković, S. Gupta, R.F. Savinell, Heat-treated iron (III) tetramethoxyphenyl porphyrin chloride supported on high-area carbon as an electrocatalyst for oxygen reduction: Part II. Kinetics of oxygen reduction, J. Electroanal. Chem. 462 (1999) 63–72.

[46]   A. Bettelheim, B.A. White, R.W. Murray, Electrocatalysis of dioxygen reduction in aqueous acid and base by multimolecular layer films of electropolymerized cobalt tetra (< i> o</i>-aminophenyl) porphyrin, J. Electroanal. Chem. Interfacial Electrochem. 217 (1987) 271–286.

[47]   S. Ma, Z. Chen, N.K. Dutta, All-optical logic gates based on two-photon absorption in semiconductor optical amplifiers, Opt. Commun. 282 (2009) 4508–4512.

[48]   H. Hu, W. Li, N.K. Dutta, Dispersion-engineered tapered planar waveguide for coherent supercontinuum generation, Opt. Commun. 324 (2014) 252–257.

[49]   C. Song, L. Zhang, J. Zhang, Reversible one-electron electro-reduction of O 2 to produce a stable superoxide catalyzed by adsorbed Co (II) hexadecafluoro-phthalocyanine in aqueous alkaline solution, J. Electroanal. Chem. 587 (2006) 293–298.

[50]   J. Zagal, M. Paez, A.A. Tanaka, Electrocatalytic activity of metal phthalocyanines for oxygen reduction, J. Electroanal. Chem. 339 (1992) 13–30.

[51]   H. Hu, W. Li, N.K. Dutta, Supercontinuum generation in dispersion-managed tapered-rib waveguide., Appl. Opt. 52 (2013) 7336–41.

[52]   H. Hu, W. Li, S. Ma, N.K. Dutta, Coherence Properties of Supercontinuum Generated in Dispersion-Tailored Lead-Silicate Microstructured Fiber Taper, Fiber Integr. Opt. 32 (2013) 209–221.

[53]   L. Jörissen, Bifunctional oxygen/air electrodes, J. Power Sources. 155 (2006) 23–32.

[54]   T.S. Olson, S. Pylypenko, P. Atanassov, K. Asazawa, K. Yamada, H. Tanaka, Anion-Exchange Membrane Fuel Cells: Dual-Site Mechanism of Oxygen Reduction Reaction in Alkaline Media on Cobalt−Polypyrrole Electrocatalysts, J. Phys. Chem. C. 114 (2010) 5049–5059. doi:10.1021/jp910572g.

[55]   A. Kucernak, F. Bidault, G. Smith, Membrane electrode assemblies based on porous silver electrodes for alkaline anion exchange membrane fuel cells, Electrochim. Acta. 82 (2012) 284–290.

[56]   H.A. Gasteiger, N.M. Marković, Just a dream—or future reality?, Science (80-.). 324 (2009) 48–49.

[57]   L.M. Roen, C.H. Paik, T.D. Jarvi, Electrocatalytic corrosion of carbon support in PEMFC cathodes, Electrochem. Solid-State Lett. 7 (2004) A19–A22.

[58]   E. Passalacqua, P.L. Antonucci, M. Vivaldi, A. Patti, V. Antonucci, N. Giordano, et al., The influence of Pt on the electrooxidation behaviour of carbon in phosphoric acid, Electrochim. Acta. 37 (1992) 2725–2730.

[59]   K.H. Kangasniemi, D.A. Condit, T.D. Jarvi, Characterization of vulcan electrochemically oxidized under simulated PEM fuel cell conditions, J. Electrochem. Soc. 151 (2004) E125–E132.

[60]   K. Kinoshita, Carbon: electrochemical and physicochemical properties, (1988).

[61]   S. Shrestha, Y. Liu, W.E. Mustain, Electrocatalytic activity and stability of Pt clusters on state-of-the-art supports: a review, Catal. Rev. 53 (2011) 256–336.

[62]   S. Yang, X. Wang, W. Chu, Z. Song, S. Zhao, An investigation of the surface intermediates of H2-SCR of NOx over Pt/H-FER, Appl. Catal. B Environ. 107 (2011) 380–385.

[63]   B. Lei, J. XUE, D. JIN, S. NI, H. SUN, Fabrication, annealing, and electrocatalytic properties of platinum nanoparticles supported on self-organized TiO$_2$ nanotubes, Rare Met. 27 (2008) 445–450.

[64] J. Shim, C.-R. Lee, H.-K. Lee, J.-S. Lee, E.J. Cairns, Electrochemical characteristics of Pt–WO$_3$/C and Pt–TiO$_2$/C electrocatalysts in a polymer electrolyte fuel cell, J. Power Sources. 102 (2001) 172–177.

[65] M. Wang, D. Guo, H. Li, High activity of novel Pd/TiO$_2$ nanotube catalysts for methanol electro-oxidation, J. Solid State Chem. 178 (2005) 1996–2000.

[66] T. Ioroi, Z. Siroma, N. Fujiwara, S. Yamazaki, K. Yasuda, Sub-stoichiometric titanium oxide-supported platinum electrocatalyst for polymer electrolyte fuel cells, Electrochem. Commun. 7 (2005) 183–188.

[67] X. Cui, J. Shi, H. Chen, L. Zhang, L. Guo, J. Gao, et al., Platinum/mesoporous WO3 as a carbon-free electrocatalyst with enhanced electrochemical activity for methanol oxidation, J. Phys. Chem. B. 112 (2008) 12024–12031.

[68] S.H. Kang, Y.-E. Sung, W.H. Smyrl, The effectiveness of sputtered PtCo catalysts on TiO2 nanotube arrays for the oxygen reduction reaction, J. Electrochem. Soc. 155 (2008) B1128–B1135.

[69] K.-S. Lee, I.-S. Park, Y.-H. Cho, D.-S. Jung, N. Jung, H.-Y. Park, et al., Electrocatalytic activity and stability of Pt supported on Sb-doped SnO$_2$ nanoparticles for direct alcohol fuel cells, J. Catal. 258 (2008) 143–152.

[70] O.A. Baturina, Y. Garsany, T.J. Zega, R.M. Stroud, T. Schull, K.E. Swider-Lyons, Oxygen reduction reaction on platinum/tantalum oxide electrocatalysts for PEM fuel cells, J. Electrochem. Soc. 155 (2008) B1314–B1321.

[71] K. Sasaki, L. Zhang, R.R. Adzic, Niobium oxide-supported platinum ultra-low amount electrocatalysts for oxygen reduction, Phys. Chem. Chem. Phys. 10 (2008) 159–167.

[72] N. Zhang, S. Zhang, C. Du, Z. Wang, Y. Shao, F. Kong, et al., Pt/Tin Oxide/Carbon Nanocomposites as Promising Oxygen Reduction Electrocatalyst with Improved Stability and Activity, Electrochim. Acta. 117 (2014) 413–419.

[73] Y. Liu, W.E. Mustain, Stability limitations for Pt/Sn–In2O3 and Pt/In–SnO2 in acidic electrochemical systems, Electrochim. Acta. 115 (2014) 116–125.

[74] J. Suntivich, K.J. May, H.A. Gasteiger, J.B. Goodenough, Y. Shao-Horn, A

perovskite oxide optimized for oxygen evolution catalysis from molecular orbital principles, Science (80-.). 334 (2011) 1383–1385.

[75]   J. Suntivich, H.A. Gasteiger, N. Yabuuchi, H. Nakanishi, J.B. Goodenough, Y. Shao-Horn, Design principles for oxygen-reduction activity on perovskite oxide catalysts for fuel cells and metal–air batteries, Nat. Chem. 3 (2011) 546–550.

[76]   S. Faculty, N. Singh, 2010 - Co3O4 and Co- Based Spinel Oxides Bifunctional Oxygen Electrodes - Unknown.pdf, 5 (2010) 556–577.

[77]   Y. Liang, H. Wang, J. Zhou, Y. Li, J. Wang, T. Regier, et al., Covalent hybrid of spinel manganese-cobalt oxide and graphene as advanced oxygen reduction electrocatalysts, J. Am. Chem. Soc. 134 (2012) 3517–3523.

[78]   G. Zhang, B.Y. Xia, X. Wang, X.W. David Lou, Strongly Coupled $NiCo_2O_4$ -rGO Hybrid Nanosheets as a Methanol-Tolerant Electrocatalyst for the Oxygen Reduction Reaction, Adv. Mater. 26 (2014) 2408–2412.

[79]   F. Jiao, H. Frei, Nanostructured manganese oxide clusters supported on mesoporous silica as efficient oxygen-evolving catalysts, Chem. Commun. 46 (2010) 2920–2922.

[80]   S.C. Petitto, E.M. Marsh, G.A. Carson, M.A. Langell, Cobalt oxide surface chemistry: the interaction of CoO (100), Co 3 O 4 (110) and Co 3 O 4 (111) with oxygen and water, J. Mol. Catal. A Chem. 281 (2008) 49–58.

[81]   M.H. Miles, Evaluation of electrocatalysts for water electrolysis in alkaline solutions, J. Electroanal. Chem. Interfacial Electrochem. 60 (1975) 89–96.

[82]   J.G. McAlpin, T.A. Stich, W.H. Casey, R.D. Britt, Comparison of cobalt and manganese in the chemistry of water oxidation, Coord. Chem. Rev. 256 (2012) 2445–2452.

[83]   N.H. Chou, P.N. Ross, A.T. Bell, T.D. Tilley, Comparison of Cobalt-based Nanoparticles as Electrocatalysts for Water Oxidation, ChemSusChem. 4 (2011) 1566–1569.

[84]   R. Bashyam, P. Zelenay, A class of non-precious metal composite catalysts for fuel cells, Nature. 443 (2006) 63–66.

[85]   A. Restovic, E. R??os, S. Barbato, J. Ortiz, J.L. Gautier, Oxygen reduction in alkaline medium at thin MnxCo3-xO4 spinel films prepared by spray pyrolysis. Effect of oxide cation composition on the reaction kinetics, J. Electroanal. Chem. 522 (2002) 141–151.

[86]   J. Xu, P. Gao, T.S. Zhao, Non-precious Co3O4 nano-rod electrocatalyst for oxygenreduction reaction in anion-exchange membranefuelcells, Energy Environ. Sci. 5 (2012) 5333–5339.

[87]   R.G. Compton, Electrode Kinetics: Reactions. Comprehensive Chemical Kinetics, Elsevier Science & Technology, 1987.

[88]   J. Xiao, Q. Kuang, S. Yang, F. Xiao, S. Wang, L. Guo, Surface structure dependent electrocatalytic activity of Co3O4anchored on graphene sheets toward oxygen reduction reaction., Sci. Rep. 3 (2013) 2300.

[89]   J. Ziókowski, Y. Barbaux, Identification of sites active in oxidation of butene-1 to butadiene and CO2 on Co3O4 in terms of the crystallochemical model of solid surfaces, J. Mol. Catal. 67 (1991) 199–215.

[90]   J.P. Beaufils, Y. Barbaux, Study of adsorption on powders by surface differential diffraction measurements. Argon on Co3O4, J. Appl. Crystallogr. 15 (1982) 301–307.

[91]   E. Yeager, Dioxygen electrocatalysis: mechanisms in relation to catalyst structure, J. Mol. Catal. 38 (1986) 5–25.

[92]   Y. Liang, H. Wang, P. Diao, W. Chang, G. Hong, Y. Li, et al., Oxygen reduction electrocatalyst based on strongly coupled cobalt oxide nanocrystals and carbon nanotubes, J. Am. Chem. Soc. 134 (2012) 15849–15857.

[93]   S. Guo, S. Zhang, L. Wu, S. Sun, Co/CoO nanoparticles assembled on graphene for electrochemical reduction of oxygen, Angew. Chemie - Int. Ed. 51 (2012) 11770–11773.

[94]   D. Huang, Y. Luo, S. Li, B. Zhang, Y. Shen, M. Wang, Active catalysts based on cobalt oxide@cobalt/N-C nanocomposites for oxygen reduction reaction in alkaline solutions, Nano Res. 7 (2014) 1054–1064.

[95]   X. Deng, H. Tuysuz, Cobalt-Oxide-Based Materials as Water Oxidation Catalyst: Recent Progress and Challenges, ACS Catal. 4 (2014) 3701=3714.

[96]   B.S. Yeo, A.T. Bell, Enhanced activity of gold-supported cobalt oxide for the electrochemical evolution of oxygen, J. Am. Chem. Soc. 133 (2011) 5587–5593.

[97]   X. Lu, Y.H. Ng, C. Zhao, Gold nanoparticles embedded within mesoporous cobalt oxide enhance electrochemical oxygen evolution, ChemSusChem. 7 (2014) 82–86. doi:10.1002/cssc.201300975.

[98]   J. Greeley, J.K. Nørskov, Combinatorial density functional theory-based screening of surface alloys for the oxygen reduction reaction, J. Phys. Chem. C. 113 (2009) 4932–4939.

[99]   J.B. Gerken, J.G. Mcalpin, J.Y.C. Chen, L. Rigsby, W.H. Casey, R.D. Britt, et al., 0 – 14 : The Thermodynamic Basis for Catalyst Structure , Stability and Activity Electrochemical Water Oxidation with Cobalt-Based Electrocatalysts from pH 0 – 14 : The Thermodynamic Basis for Catalyst Structure , Stability and Activity, (2011) 0–41.

[100] M. Lenglet, R. Guillamet, J. Dürr, D. Gryffroy, R.E. Vandenberghe, Electronic structure of NiCo2O4 by XANES, EXAFS and 61Ni Mössbauer studies, Solid State Commun. 74 (1990) 1035–1039.

[101] N. Heller-Ling, M. Prestat, J.-L. Gautier, J.-F. Koenig, G. Poillerat, P. Chartier, Oxygen electroreduction mechanism at thin NixCo3−xO4 spinel films in a double channel electrode flow cell (DCEFC), Electrochim. Acta. 42 (1997) 197–202.

[102] P. Manivasakan, P. Ramasamy, J. Kim, Use of urchin-like NixCo3-xO4 hierarchical nanostructures based on non-precious metals as bifunctional electrocatalysts for anion-exchange membrane alkaline alcohol fuel cells., Nanoscale. 6 (2014) 9665–72. doi:10.1039/c4nr01802h.

[103] V. Rashkova, S. Kitova, I. Konstantinov, T. Vitanov, Vacuum evaporated thin films of mixed cobalt and nickel oxides as electrocatalyst for oxygen evolution and reduction, Electrochim. Acta. 47 (2002) 1555–1560. doi:10.1016/S0013-4686(01)00897-0.

[104] P. Boldrin, A.K. Hebb, A. a. Chaudhry, L. Otley, B. Thiebaut, P. Bishop, et al., Direct Synthesis of Nanosized NiCo 2 O 4 Spinel and Related Compounds via Continuous Hydrothermal Synthesis Methods, Ind. Eng. Chem. Res. 46 (2007) 4830–4838.

[105] L. Li, L. Shen, P. Nie, G. Pang, J. Wang, H. Li, et al., Porous $NiCo_2O_4$ nanotubes as a noble-metal-free effective bifunctional catalyst for rechargeable Li–O_2 batteries, J. Mater. Chem. A. 3 (2015) 24309–24314.

[106] L. Li, A. Manthiram, Decoupled bifunctional air electrodes for high-performance hybrid lithium-air batteries, Nano Energy. 9 (2014) 94–100. doi:10.1016/j.nanoen.2014.07.002.

[107] P. Rasiyah, A.C.C. Tseung, D.B. Hibbert, A Mechanistic Study of Oxygen Evolution on NiCo2 O 4 I. Formation of Higher Oxides, J. Electrochem. Soc. 129 (1982) 1724–1727.

[108] C. Bocca, a Barbucci, M. Delucchi, G. Cerisola, NICKEL–COBALT oxide-coated electrodes: influence of the preparation technique on oxygen evolution reaction (OER) in an alkaline solution, Int. J. Hydrogen Energy. 24 (1999) 21–26.

[109] T. Maiyalagan, K. a Jarvis, S. Therese, P.J. Ferreira, A. Manthiram, Spinel-type lithium cobalt oxide as a bifunctional electrocatalyst for the oxygen evolution and oxygen reduction reactions., Nat. Commun. 5 (2014) 3949.

[110] L.-P. Wang, T. Van Voorhis, Direct-coupling O2 bond forming a pathway in cobalt oxide water oxidation catalysts, J. Phys. Chem. Lett. 2 (2011) 2200–2204.

[111] Y. Surendranath, M.W. Kanan, D.G. Nocera, Mechanistic studies of the oxygen evolution reaction by a cobalt-phosphate catalyst at neutral pH, J. Am. Chem. Soc. 132 (2010) 16501–16509.

[112] X. Wu, K. Scott, A Li-doped Co3O4 oxygen evolution catalyst for non-precious metal alkaline anion exchange membrane water electrolysers, Int. J. Hydrogen Energy. 38 (2013) 3123–3129. doi:10.1016/j.ijhydene.2012.12.087.

[113] I. Nikolov, R. Darkaoui, E. Zhecheva, R. Stoyanova, N. Dimitrov, T. Vitanov, Electrocatalytic activity of spinel related cobalties MxCo3−xO4 (M= Li, Ni, Cu) in the oxygen evolution reaction, J. Electroanal. Chem. 429 (1997) 157–168.

[114] D.G. Wickham, W.J. Croft, Crystallographic and magnetic properties of several spinels containing trivalent ja-1044 manganese, J. Phys. Chem. Solids. 7 (1958) 351–360.

[115] E. Rios, P. Chartier, J.-L. Gautier, Oxygen evolution electrocatalysis in alkaline medium at thin MnxCo3-xO4 ($0 \leq x \leq 1$) spinel films on glass / SnO2: F prepared by spray pyrolysis, Solid State Sci. 1 (1999) 267–277.

[116] S. Ma, W. Li, H. Hu, N.K. Dutta, High speed ultra short pulse fiber ring laser using photonic crystal fiber nonlinear optical loop mirror, Opt. Commun. 285 (2012) 2832–2835.

[117] X. Zhang, H. Hu, W. Li, N.K. Dutta, Mid-infrared supercontinuum generation in tapered As $_2$ S $_3$ chalcogenide planar waveguide, J. Mod. Opt. 63 (2016) 1965–1971.

[118] B.T. Kolomiets, I.T. Sheftel, E. V Kurlina, Electrical properties of some compound oxide semiconductors, Sov. PHYSICS-TECHNICAL Phys. 2 (1957) 40–58.

[119] B. Boucher, R. Buhl, R. Di Bella, M. Perrin, Etude par des mesures de diffraction de neutrons et de magnétisme des propriétés cristallines et magnétiques de composés cubiques spinelles Co3-xMnxO4 (0, 6$\leq$ x$\leq$ 1, 2), J. Phys. 31 (1970) 113–119.

[120] X. Zhang, H. Hu, W. Li, N.K. Dutta, High-repetition-rate ultrashort pulsed fiber ring laser using hybrid mode locking, Appl. Opt. 55 (2016) 7885–7891.

[121] W. Li, S. Ma, H. Hu, N.K. Dutta, All-optical latches based on two-photon absorption in semiconductor optical amplifiers, JOSA B. 29 (2012) 2603–2609.

[122] G. Blasse, Superexchange in the spinel structure. Some magnetic properties of oxides M2+ Co2O4 and M2+ Rh2O4 with spinel structure, Philips Res Rep Suppl. 18 (1963) 383.

[123] E. Rios, J.-L. Gautier, G. Poillerat, P. Chartier, Mixed valency spinel oxides of transition metals and electrocatalysis: case of the MnxCo3−xO4 system, Electrochim. Acta. 44 (1998) 1491–1497.

[124] G.G. Wildgoose, C.E. Banks, R.G. Compton, Metal nanoparticles and related materials supported on Carbon nanotubes: Methods and applications, Small. 2 (2006) 182–193.

[125] V. Georgakilas, D. Gournis, V. Tzitzios, L. Pasquato, D.M. Guldi, M. Prato, Decorating carbon nanotubes with metal or semiconductor nanoparticles, J. Mater. Chem. 17 (2007) 2679.

[126] D. Eder, Carbon Nanotube - Inorganic Hybrids, Chem. Rev. 110 (2010) 1348–1385.

[127] T.N. Lambert, D.J. Davis, W. Lu, S.J. Limmer, P.G. Kotula, A. Thuli, et al., Graphene–Ni–α-MnO2 and –Cu–α-MnO2 nanowire blends as highly active non-precious metal catalysts for the oxygen reduction reaction, Chem. Commun. 48 (2012) 7931.

[128] J. Wu, D. Zhang, Y. Wang, Y. Wan, Manganese oxide-graphene composite as an efficient catalyst for 4-electron reduction of oxygen in alkaline media, Electrochim. Acta. 75 (2012) 305–310.

[129] V. Datsyuk, M. Kalyva, K. Papagelis, J. Parthenios, D. Tasis, A. Siokou, et al., Chemical oxidation of multiwalled carbon nanotubes, Carbon N. Y. 46 (2008) 833–840.

[130] Y. Xing, L. Li, C.C. Chusuei, R. V Hull, Sonochemical Oxidation of Multiwalled Carbon Nanotubes, Langmuir. 21 (2005) 4185–4190.

[131] W.S. Hummers Jr, R.E. Offeman, Preparation of graphitic oxide, J. Am. Chem. Soc. 80 (1958) 1339.

[132] M.L. Toebes, J.M.P. van Heeswijk, J.H. Bitter, A.J. Van Dillen, K.P. de Jong, The influence of oxidation on the texture and the number of oxygen-containing surface groups of carbon nanofibers, Carbon N. Y. 42 (2004) 307–315.

[133] T.G. Ros, A.J. Van Dillen, J.W. Geus, D.C. Koningsberger, Surface oxidation of carbon nanofibres, Chem. Eur. J. 8 (2002) 1151–1162.

[134] M.T. Martí, M.A. Callejas, A.M. Benito, M. Cochet, T. Seeger, A. Anson, et al., Sensitivity of single wall carbon nanotubes to oxidative processing: structural

modification, intercalation and functionalisation, Carbon N. Y. 41 (2003) 2247–2256.

[135] H. Wang, H. Dai, Strongly coupled inorganic-nano-carbon hybrid materials for energy storage., Chem. Soc. Rev. 42 (2013) 3088–113.

[136] Y. Liang, Y. Li, H. Wang, J. Zhou, J. Wang, T. Regier, et al., Co3O4 nanocrystals on graphene as a synergistic catalyst for oxygen reduction reaction, Nat. Mater. 10 (2011) 780–786.

[137] C.W.B. Bezerra, L. Zhang, K. Lee, H. Liu, A.L.B. Marques, E.P. Marques, et al., A review of Fe–N/C and Co–N/C catalysts for the oxygen reduction reaction, Electrochim. Acta. 53 (2008) 4937–4951.

[138] J.L. Martin de Vidales, E. Vila, R.M. Rojas, O. Garcia-Martinez, Thermal Behavior in Air and Reactivity in Acid Medium of Cobalt Manganese Spinels MnxCo3-xO4 (1. ltoreq. x. ltoreq. 3) Synthesized at Low Temperature, Chem. Mater. 7 (1995) 1716–1721.

[139] H. Wang, Y. Yang, Y. Liang, G. Zheng, Y. Li, Y. Cui, et al., Rechargeable Li–O2 batteries with a covalently coupled MnCo2O4–graphene hybrid as an oxygen cathode catalyst, Energy Environ. Sci. 5 (2012) 7931.

[140] R. Ning, J. Tian, A.M. Asiri, A.H. Qusti, A.O. Al-Youbi, X. Sun, Spinel CuCo2O4 nanoparticles supported on n-doped reduced graphene oxide: A highly active and stable hybrid electrocatalyst for the oxygen reduction reaction, Langmuir. 29 (2013) 13146–13151.

[141] S.K. Singh, V.M. Dhavale, S. Kurungot, Low surface energy plane exposed Co3O4 nanocubes supported on nitrogen-doped graphene as an electrocatalyst for efficient water oxidation, ACS Appl. Mater. Interfaces. 7 (2015) 442–451. doi:10.1021/am506450c.

[142] M. Gong, Y. Li, H. Wang, Y. Liang, J.Z. Wu, J. Zhou, et al., An Advanced Ni–Fe Layered Double Hydroxide Electrocatalyst for Water Oxidation, J. Am. Chem. Soc. 135 (2013) 8452–8455. doi:10.1021/ja4027715.

[143] Y. Li, M. Gong, Y. Liang, J. Feng, J.E. Kim, H. Wang, et al., Advanced zinc-air batteries based on high-performance hybrid electrocatalysts, Nat Commun. 4 (2013) 1805.

[144] H. Lee, S.M. Dellatore, W.M. Miller, P.B. Messersmith, Mussel-inspired surface chemistry for multifunctional coatings., Science. 318 (2007) 426–430.

[145] Y. Liu, K. Ai, L. Lu, Polydopamine and its derivative materials: Synthesis and promising applications in energy, environmental, and biomedical fields, Chem. Rev. 114 (2014) 5057–5115.

[146] J. Wang, K. Li, H.X. Zhong, D. Xu, Z.L. Wang, Z. Jiang, et al., Synergistic Effect between Metal-Nitrogen-Carbon Sheets and NiO Nanoparticles for Enhanced Electrochemical Water-Oxidation Performance, Angew. Chemie - Int. Ed. 54 (2015) 10530–10534.

[147] G. Zhang, B.Y. Xia, C. Xiao, L. Yu, X. Wang, Y. Xie, et al., General formation of complex tubular nanostructures of metal oxides for the oxygen reduction reaction and lithium-ion batteries, Angew. Chemie - Int. Ed. 52 (2013) 8643–8647.

[148] Q. Liu, J. Jin, J. Zhang, NiCo2S4 @graphene as a Bifunctional Electrocatalyst for Oxygen Reduction and Evolution Reactions, ACS Appl. Mater. Interfaces. 5 (2013) 5002–5008.

[149] X.-Y. Yan, X.-L. Tong, Y.-F. Zhang, X.-D. Han, Y.-Y. Wang, G.-Q. Jin, et al., Cuprous oxide nanoparticles dispersed on reduced graphene oxide as an efficient electrocatalyst for oxygen reduction reaction, Chem. Commun. 48 (2012) 1892.

[150] S. Mao, Z. Wen, H. Kim, G. Lu, P. Hurley, J. Chen, A general approach to one-pot fabrication of crumpled graphene-based nanohybrids for energy applications, ACS Nano. 6 (2012) 7505–7513.

[151] W. Zhang, Y. Zeng, C. Xu, H. Tan, W. Liu, J. Zhu, et al., Fe2O3 nanocluster-decorated graphene as O2 electrode for high energy Li–O2 batteries, RSC Adv. 2 (2012) 8508.

[152] H.-Q. Wang, J. Chen, S.-J. Hu, X.-H. Zhang, X.-P. Fan, J. Du, et al., Direct growth of flower-like 3D MnO2 ultrathin nanosheets on carbon paper as efficient cathode catalyst for rechargeable Li-O2 batteries, Rsc Adv. 5 (2015) 72495–72499.

[153] J. Zhang, Y. Mo, M.B. Vukmirovic, R. Klie, K. Sasaki, R.R. Adzic, Platinum

monolayer electrocatalysts for O2 reduction: Pt monolayer on Pd (111) and on carbon-supported Pd nanoparticles, J. Phys. Chem. B. 108 (2004) 10955–10964.

[154] Y. Liu, W.E. Mustain, High stability, high activity Pt/ITO oxygen reduction electrocatalysts, J. Am. Chem. Soc. 135 (2012) 530–533.

[155] S. Trasatti, O.A. Petrii, Real surface area measurements in electrochemistry, J. Electroanal. Chem. 327 (1992) 353–376.

[156] R.F. Savinell, R.L.Z. Iii, J.A. Adams, Electrochemically Active Surface Area Voltammetric Charge Correlations for Ruthenium and Iridium Dioxide Electrodes, 137 (1990) 2–7.

[157] A. Sandhu, B. Hamilton, A.R. Peaker, R.A.A. Kubiak, W.Y. Leong, E.H.C. Parker, The Electrochemical Society Softbound Proceedings Series, in: 167th Meet. Toronto, 1985: p. 7.

[158] G. Li, J. Tang, J. Sheng, Preparation and electrocatalytic property of WC/carbon nanotube composite, Electrochim. Acta. 52 (2007) 2018–2023.

[159] G. Li, Y. Zheng, W. Zhang, Preparation and electrocatalytic activity of hollow global tungsten carbide with mesoporosity, Microporous Mesoporous Mater. 85 (2005) 234–240.

[160] L. Schlapbach, A. Züttel, Hydrogen-storage materials for mobile applications, Nature. 414 (2001) 353–358.

[161] M. Wu, P.K. Shen, Z. Wei, S. Song, M. Nie, High activity PtPd-WC/C electrocatalyst for hydrogen evolution reaction, J. Power Sources. 166 (2007) 310–316.

[162] D.J. Ham, J.S. Lee, Transition metal carbides and nitrides as electrode materials for low temperature fuel cells, Energies. 2 (2009) 873–899.

[163] R. Ganesan, J.S. Lee, Tungsten Carbide Microspheres as a Noble-Metal-Economic Electrocatalyst for Methanol Oxidation, Angew. Chemie Int. Ed. 44 (2005) 6557–6560.

[164] D.R. McIntyre, G.T. Burstein, A. Vossen, Effect of carbon monoxide on the

electrooxidation of hydrogen by tungsten carbide, J. Power Sources. 107 (2002) 67–73.

[165] R. Ganesan, D.J. Ham, J.S. Lee, Platinized mesoporous tungsten carbide for electrochemical methanol oxidation, Electrochem. Commun. 9 (2007) 2576–2579.

[166] R.B. Levy, M. Boudart, Platinum-like behavior of tungsten carbide in surface catalysis, Science (80-.). 181 (1973) 547–549.

[167] Y.-J. Chen, J.-B. Li, Q.-M. Wei, H.-Z. Zhai, Preparation of different morphology of TaC x whiskers, Mater. Lett. 56 (2002) 279–283.

[168] Y. Liu, S. Shrestha, W.E. Mustain, Synthesis of nanosize tungsten oxide and its evaluation as an electrocatalyst support for oxygen reduction in acid media, ACS Catal. 2 (2012) 456–463.

[169] V.S. Palanker, R.A. Gajyev, D. V Sokolsky, On adsorption and electro-oxidation of some compounds on tungsten carbide; their effect on hydrogen electro-oxidation, Electrochim. Acta. 22 (1977) 133–136.

[170] M. Nie, P.K. Shen, M. Wu, Z. Wei, H. Meng, A study of oxygen reduction on improved Pt-WC/C electrocatalysts, J. Power Sources. 162 (2006) 173–176.

[171] Y. Liu, W.E. Mustain, Structural and Electrochemical Studies of Pt Clusters Supported on WC for ORR.pdf, (2011) 212–220.

[172] J.B. Claridge, A.P.E. York, A.J. Brungs, M.L.H. Green, Study of the temperature-programmed reaction synthesis of early transition metal carbide and nitride catalyst materials from oxide precursors, Chem. Mater. 12 (2000) 132–142.

[173] A.C.C. Tseung, K.Y. Chen, Hydrogen spill-over effect on Pt/WO$_3$ anode catalysts, Catal. Today. 38 (1997) 439–443.

[174] P.J. Kulesza, L.R. Faulkner, Electrocatalytic properties of bifunctional Pt/W (VI, V) oxide microstructures electrodeposited on carbon substrates, J. Electroanal. Chem. Interfacial Electrochem. 259 (1989) 81–98.

[175] V. Raghuveer, B. Viswanathan, Synthesis, characterization and electrochemical studies of Ti-incorporated tungsten trioxides as platinum support for methanol

oxidation, J. Power Sources. 144 (2005) 1–10.

[176] S. Wasmus, A. Küver, Methanol oxidation and direct methanol fuel cells: a selective review, J. Electroanal. Chem. 461 (1999) 14–31.

[177] C. Bock, C. Paquet, M. Couillard, G.A. Botton, B.R. MacDougall, Size-selected synthesis of PtRu nano-catalysts: reaction and size control mechanism, J. Am. Chem. Soc. 126 (2004) 8028–8037.

[178] S. Zhao, H. Yu, R. Maric, N. Danilovic, C. Capuano, K.E. Ayers, et al., Determining the Electrochemically Active Area of IrOx Powder Catalysts in an Operating Proton Exchange Membrane Electrolyzer, ECS Trans. 69 (2015) 877–881.

[179] S. Zhao, H. Yu, R. Maric, N. Danilovic, C.B. Capuano, K.E. Ayers, et al., Calculating the Electrochemically Active Surface Area of Iridium Oxide in Operating Proton Exchange Membrane Electrolyzers, J. Electrochem. Soc. 162 (2015) F1292–F1298.

[180] E.N. El Sawy, V.I. Birss, Nano-porous iridium and iridium oxide thin films formed by high efficiency electrodeposition, J. Mater. Chem. 19 (2009) 8244–8252.

[181] T.R. Ralph, G.A. Hards, J.E. Keating, S.A. Campbell, D.P. Wilkinson, M. Davis, et al., Low cost electrodes for proton exchange membrane fuel cells performance in single cells and Ballard stacks, J. Electrochem. Soc. 144 (1997) 3845–3857.

[182] W. Vielstich, H. Yokokawa, H.A. Gasteiger, Handbook of fuel cells: fundamentals technology and applications, John Wiley & Sons, 2009.

[183] A. Wieckowski, Interfacial electrochemistry: theory: experiment, and applications, CRC Press, 1999.

[184] M.E.G. Lyons, S. Floquet, Mechanism of oxygen reactions at porous oxide electrodes. Part 2—Oxygen evolution at RuO_2, IrO_2 and $Ir_xRu_{1-x}O_2$ electrodes in aqueous acid and alkaline solution, Phys. Chem. Chem. Phys. 13 (2011) 5314–5335.

[185] T. Biegler, D.A.J. Rand, R. Woods, Limiting oxygen coverage on platinized

platinum; relevance to determination of real platinum area by hydrogen adsorption, J. Electroanal. Chem. Interfacial Electrochem. 29 (1971) 269–277.

[186] L.D. Burke, D.P. Whelan, A voltammetric investigation of the charge storage reactions of hydrous iridium oxide layers, J. Electroanal. Chem. Interfacial Electrochem. 162 (1984) 121–141.

[187] E. Guerrini, H. Chen, S. Trasatti, Oxygen evolution on aged IrOx/Ti electrodes in alkaline solutions, J. Solid State Electrochem. 11 (2007) 939–945.

[188] V. Raghuveer, A. Manthiram, Mesoporous carbons with controlled porosity as an electrocatalytic support for methanol oxidation, J. Electrochem. Soc. 152 (2005) A1504–A1510.

[189] D.R. Rolison, Catalytic nanoarchitectures--the importance of nothing and the unimportance of periodicity, Science (80-.). 299 (2003) 1698–1701.

[190] W.J. Blaedel, R.C. Engstrom, Investigations of the ferricyanide-ferrocyanide system by pulsed rotation voltammetry, Anal. Chem. 50 (1978) 476–479.

[191] M. Moser, C. Mondelli, A.P. Amrute, A. Tazawa, D. Teschner, M.E. Schuster, et al., HCl Oxidation on IrO_2-Based Catalysts: From Fundamentals to Scale-Up, ACS Catal. 3 (2013) 2813–2822.

[192] A.A.F. Grupioni, E. Arashiro, T.A.F. Lassali, Voltammetric characterization of an iridium oxide-based system: the pseudocapacitive nature of the $Ir_{0.3}Mn_{0.7}O_2$ electrode, Electrochim. Acta. 48 (2002) 407–418.

[193] U.S. Doe, Fuel Cells Technical Plan, Multi-Year Res. Dev. Demonstr. Plan. (2012) 18.

[194] Y. Liu, S. Zhao, W.E. Mustain, Understanding the Growth of Pt Nanoparticles by Galvanic Displacement on ITO Nanocubes for ORR, 64 (2014) 191–198.

[195] M. Nakada, A. Ishihara, S. Mitsushima, N. Kamiya, K. Ota, Effect of Tin Oxides on Oxide Formation and Reduction of Platinum Particles, Electrochem. Solid-State Lett. . 10 (2007) F1–F4.

[196] M. Batzill, U. Diebold, The surface and materials science of tin oxide, Prog. Surf.

Sci. 79 (2005) 47–154.

[197] N.M. Markovic, H.A. Gasteiger, P.N. Ross, Oxygen reduction on platinum low-index single-crystal surfaces in alkaline solution: rotating ring diskPt (hkl) studies, J. Phys. Chem. 100 (1996) 6715–6721.

[198] S. Park, S.A. Wasileski, M.J. Weaver, Electrochemical infrared characterization of carbon-supported platinum nanoparticles: a benchmark structural comparison with single-crystal electrodes and high-nuclearity carbonyl clusters, J. Phys. Chem. B. 105 (2001) 9719–9725.

[199] L. Genies, R. Faure, R. Durand, Electrochemical reduction of oxygen on platinum nanoparticles in alkaline media, Electrochim. Acta. 44 (1998) 1317–1327.

[200] N.A. Anastasijević, V. Vesović, R.R. Adžić, Determination of the kinetic parameters of the oxygen reduction reaction using the rotating ring-disk electrode: Part I. Theory, J. Electroanal. Chem. Interfacial Electrochem. 229 (1987) 305–316.

[201] E.E. Kohnke, Electrical and optical properties of natural stannic oxide crystals, J. Phys. Chem. Solids. 23 (1962) 1557–1562.

[202] B. Pivovar, F.C.T. Leader, P. Fedkiw, A.R.O.R. Mantz, A.R.O.B. Pivovar, T. Zawodzinski, et al., Alkaline membrane fuel cell workshop final report, in: Work. Held December, 2006: p. 13.

[203] H. Zhu, S. Zhang, Y. Huang, L. Wu, S. Sun, Monodisperse $M_xFe_{3-x}O_4$ (M = Fe, Cu, Co, Mn) Nanoparticles and Their Electrocatalysis for Oxygen Reduction Reaction, Nano Lett. 13 (2013) 2947–2951.

[204] Y.J. Sa, K. Kwon, J.Y. Cheon, F. Kleitz, S.H. Joo, Ordered mesoporous Co_3O_4 spinels as stable, bifunctional, noble metal-free oxygen electrocatalysts, J. Mater. Chem. A. 1 (2013) 9992.

[205] Y. Meng, W. Song, H. Huang, Z. Ren, S.Y. Chen, S.L. Suib, Structure-property relationship of bifunctional MnO_2 nanostructures: Highly efficient, ultra-stable electrochemical water oxidation and oxygen reduction reaction catalysts identified in alkaline media, J. Am. Chem. Soc. 136 (2014) 11452–11464.

[206] M. Fayette, a. Nelson, R.D. Robinson, Electrophoretic deposition improves

catalytic performance of Co$_3$O$_4$ nanoparticles for oxygen reduction/oxygen evolution reactions, J. Mater. Chem. A. 3 (2015) 4274–4283.

[207]   W. Tang, Y. Hou, F. Wang, L. Liu, Y. Wu, K. Zhu, LiMn$_2$O$_4$ Nanotube as Cathode Material of Second-Level Charge Capability for Aqueous Rechargeable Batteries, Nano Lett. 13 (2013) 2036–2040.

[208]   P. Li, Y. Yang, E. Shi, Q. Shen, Y. Shang, S. Wu, et al., Core-Double-Shell, Carbon Nanotube@Polypyrrole@MnO$_2$ Sponge as Freestanding, Compressible Supercapacitor Electrode, ACS Appl. Mater. Interfaces. 6 (2014) 5228–5234.

[209]   R.-R. Bi, X.-L. Wu, F.-F. Cao, L.-Y. Jiang, Y.-G. Guo, L.-J. Wan, Highly Dispersed RuO2 Nanoparticles on Carbon Nanotubes: Facile Synthesis and Enhanced Supercapacitance Performance, J. Phys. Chem. C. 114 (2010) 2448–2451.

[210]   Z. Chen, A. Yu, D. Higgins, H. Li, H. Wang, Z. Chen, Highly Active and Durable Core − Corona Structured Bifunctional Catalyst for Rechargeable Metal − Air Battery Application, Nano Lett. 12 (2012) 1946–1952.

[211]   S. Gupta, L. Qiao, S. Zhao, H. Xu, Y. Lin, S. V Devaguptapu, et al., Highly Active and Stable Graphene Tubes Decorated with FeCoNi Alloy Nanoparticles via a Template-Free Graphitization for Bifunctional Oxygen Reduction and Evolution, Adv. Energy Mater. (2016).

[212]   Y. Hou, Z. Wen, S. Cui, S. Ci, S. Mao, J. Chen, An advanced nitrogen-doped graphene/cobalt-embedded porous carbon polyhedron hybrid for efficient catalysis of oxygen reduction and water splitting, Adv. Funct. Mater. 25 (2015) 872–882.

[213]   G. Zhou, D.W. Wang, L.C. Yin, N. Li, F. Li, H.M. Cheng, Oxygen bridges between nio nanosheets and graphene for improvement of lithium storage, ACS Nano. 6 (2012) 3214–3223.

[214]   S. Mao, Z. Wen, T. Huang, Y. Hou, J. Chen, High-performance bi-functional electrocatalysts of 3D crumpled graphene-cobalt oxide nanohybrids for oxygen reduction and evolution reactions, Energy Environ. Sci. 7 (2014) 609–616.

[215]   S. Zhao, B. Rasimick, W. Mustain, H. Xu, Highly durable and active Co$_3$O$_4$ nanocrystals supported on carbon nanotubes as bifunctional electrocatalysts in alkaline media, Appl. Catal. B Environ. 203 (2017) 138–145.

[216] S. Kundu, Y. Wang, W. Xia, M. Muhler, Thermal stability and reducibility of oxygen-containing functional groups on multiwalled carbon nanotube surfaces: A quantitative high-resolution xps and TPD/TPR study, J. Phys. Chem. C. 112 (2008) 16869–16878.

[217] D. V Kosynkin, A.L. Higginbotham, A. Sinitskii, J.R. Lomeda, A. Dimiev, B.K. Price, et al., Longitudinal unzipping of carbon nanotubes to form graphene nanoribbons, Nature. 458 (2009) 872–876.

[218] L. Zhu, W. Wu, Y. Zhu, W. Tang, Y. Wu, Composite of CoOOH nanoplates with multiwalled carbon nanotubes as superior cathode material for supercapacitors, J. Phys. Chem. C. 119 (2015) 7069–7075.

[219] M. Xu, D.N. Futaba, M. Yumura, K. Hata, Tailoring Temperature Invariant Viscoelasticity of Carbon Nanotube Material, Nano Lett. 11 (2011) 3279–3284.

[220] W. Li, H. Hu, X. Zhang, S. Zhao, K. Fu, N.K. Dutta, High-speed ultrashort pulse fiber ring laser using charcoal nanoparticles, Appl. Opt. 55 (2016) 2149–2154.

[221] L. Shahriary, A. a. Athawale, Graphene Oxide Synthesized by using Modified Hummers Approach, Int. J. Renew. Energy Environ. Eng. 02 (2014) 58–63.

[222] and C.-T.C. Jianguo Song, Xinzhi Wang, Preparation and characterization of graphene oxide, J. Nanomater. 2014 (2014).

[223] B.H. Stuart, Spectral Analysis, in: Infrared Spectrosc. Fundam. Appl., John Wiley & Sons, Ltd, 2005: pp. 45–70.

[224] N. Ramaswamy, S. Mukerjee, Fundamental mechanistic understanding of electrocatalysis of oxygen reduction on Pt and non-Pt surfaces: acid versus alkaline media, Adv. Phys. Chem. 2012 (2012).

[225] S. Zhao, A.E. Wangstrom, Y. Liu, W.A. Rigdon, W.E. Mustain, Stability and Activity of Pt/ITO Electrocatalyst for Oxygen Reduction Reaction in Alkaline Media, Electrochim. Acta. 157 (2015) 175–182.

[226] M.S. Burke, M.G. Kast, L. Trotochaud, A.M. Smith, S.W. Boettcher, Cobalt–Iron (Oxy) hydroxide Oxygen Evolution Electrocatalysts: The Role of Structure and

Composition on Activity, Stability, and Mechanism, J. Am. Chem. Soc. 137 (2015) 3638–3648.

[227] G.-G. Lee, G.-H. Ha, Synthesis of Ultra Fine Titanium-Tungsten Carbide Powder from Titanium Dioxide and Ammonium Metatungstate, Mater. Trans. 50 (2009) 187–191.

[228] E.A. Gulbransen, G.H. Meier, Thermochemical stability diagrams for condensed phases and volatility diagrams for volatile species over condensed phases in twenty metal-sulfur-oxygen systems between 1150 and 1450/sup 0/K, Pittsburgh Univ., PA (USA). Dept. of Metallurgical and Materials Engineering, 1980.

[229] J. Bisquert, Physical electrochemistry of nanostructured devices, Phys. Chem. Chem. Phys. 10 (2008) 49–72.

[230] A.J. Nozik, R. Memming, Physical chemistry of semiconductor-liquid interfaces, J. Phys. Chem. 100 (1996) 13061–13078.

[231] W.J. Albery, G.J. O'Shea, A.L. Smith, Interpretation and use of Mott-Schottky plots at the semiconductor/electrolyte interface, J. Chem. Soc. Faraday Trans. 92 (1996) 4083.

[232] F. Fabregat-Santiago, G. Garcia-Belmonte, J. Bisquert, P. Bogdanoff, A. Zaban, Mott-Schottky Analysis of Nanoporous Semiconductor Electrodes in Dielectric State Deposited on SnO_2 (F) Conducting Substrates, J. Electrochem. Soc. 150 (2003) E293–E298.